CHAPTER 4: GEOLOGIC SETTING

4. GEOLOGIC SETTING

This chapter provides the detailed assessment of the geologic setting of the KNPS and Duynefontyn sites (hosting the KNPS and a new build site) and surrounding region. It begins with a review of the tectonic history of Africa and the Western Cape, which is summarized in Section 4.1. The regional geologic and seismotectonic setting is described in Section 4.2, including the alternative tectonic interpretations for the Western Cape and their implications for the SSM TI Team's evaluation and integration of seismic source data, models, and methods that is described in Chapter 8. Information about available geodetic measurements and crustal stress for the Western Cape are also discussed in Section 4.2. Section 4.3 summarises the historical seismicity analysis from Albini and Flint (2023) and provides the SSM TI Team's evaluation and assessment of their analysis. This evaluation and assessment informs the SSM TI Team's project earthquake catalogue that is described in Chapter 6. The geology of bedrock and surficial deposits at the KNPS and new build sites is described in Section 4.4. The details of the geotechnical and geophysical tests that were performed to develop the shear-wave velocity (V_S) profiles of the Duynefontyn site are described in Section 4.5. Information from sections 4.4 and 4.5 support the GMM TI Team's site response modeling that is described in Section 9.4.

4.1 TECTONIC HISTORY OF THE WESTERN CAPE

The tectonic history recorded in the geology of Africa spans nearly 4 billion years of Earth history (e.g., Tankard et al., 1982). The African continent comprises several Precambrian cratons that formed between about 3.6 and 2 billion years ago. The cratons are bounded by younger mobile belts that formed between 2 billion and 300 million years ago. These mobile belts are narrow zones of sedimentary and volcanic strata that were deposited between the cratons. They were subsequently deformed during the convergent plate tectonic processes that stitched the cratons together to make the African plate (Figure 4-1). The active tectonism recorded in the mobile belts range from Archean-age orogenesis (2 billion years ago) to Proterozoic orogenesis such as the Kibaran Orogeny (1.2 billion to 950 million years ago) which occurred in eastern and southern Africa (e.g., Tack et al., 2010, Thomas et al. 1994). All these orogenic events reflect an active period of tectonism in the Proterozic and earliest Palaeozoic involving the assembly and breakup of several supercontinents (including Rodinia and Pannotia) that culminated with the formation of Gondwana (e.g., Hartnady et al., 1985; Meert and Van der Voo, 1997; Meert and Lieberman, 2008; Gaucher et al., 2009). Gondwana later collided with Laurasia in the Carboniferous (359 to 299 Ma) to form a single supercontinent called Pangea.

Collectively, the series of major Neoproterozoic orogenic events which related to the formation of the supercontinents Gondwana is referred to as the Pan-African orogeny (e.g., van Hinsbergen et al., 2011). This orogeny is also known as the Pan-Gondwanan or Saldanian Orogeny (Rozendaal et al., 1999). The Saldania belt (Figure 4-1) is an arcuate fold belt along the southern tip of Africa that is part of the larger system of Pan-African orogenic belts (e.g., Hartnady et al., 1985; Gaucher et al., 2009). Poor exposures and uniformly low grades of metamorphism make correlating the Saldania belt with similar Pan-African belts to the north difficult, and there are several contrasting views about the tectonostratigraphic make-up and overall geodynamic setting of the Saldanian belt (Hartnady et al., 1974; Von Veh 1983; Rozendaal et al., 1999; Belcher and Kisters 2003; Gresse et al. 2006; Frimmel, 2009; Frimmel

et al., 2011, 2013; Buggisch et al., 2010; Rowe et al., 2010). Nearest the Duynefontyn site, the Saldania belt comprises a low-grade metamorphic and folded supracrustal strata collectively referred to as the Malmesbury Group. Areally extensive syn-, late- and post-tectonic granites of the 550–510 Ma Cape Granite Suite intrude the Malmesbury Group. Structural relationships indicate that the granites were emplaced during late-stage deformation, although some may be post-tectonic (e.g., Scheepers 1995; Scheepers et al., Schoch 2006). Synmagmatic deformation of the granite is evident in the Darling batholith that has intruded the central Colenso fault zone over a strike length of more than 40 km (Kisters and Belcher, 2018).

The last major compressional event to impact the Western Cape was the Permo-Triassic (~245 and ~278 Ma) Cape Orogeny (Söhnge and Hälbich, 1983; De Beer, 1990; Hansma et al., 2015). The Cape Orogeny formed the Cape Fold Belt by deforming the Early Palaeozoic Cape Supergroup strata (e.g., Thamm and Johnson, 2006). The orogeny is responsible for the dominant structural characteristics seen along the southern coast of Africa today (Hälbich, 1983). Karoo Supergroup sedimentation within the Karoo basin located north of the Cape Fold Belt, farther inland, continued from ~350 to ~180 Ma (Tankard et al., 2012).
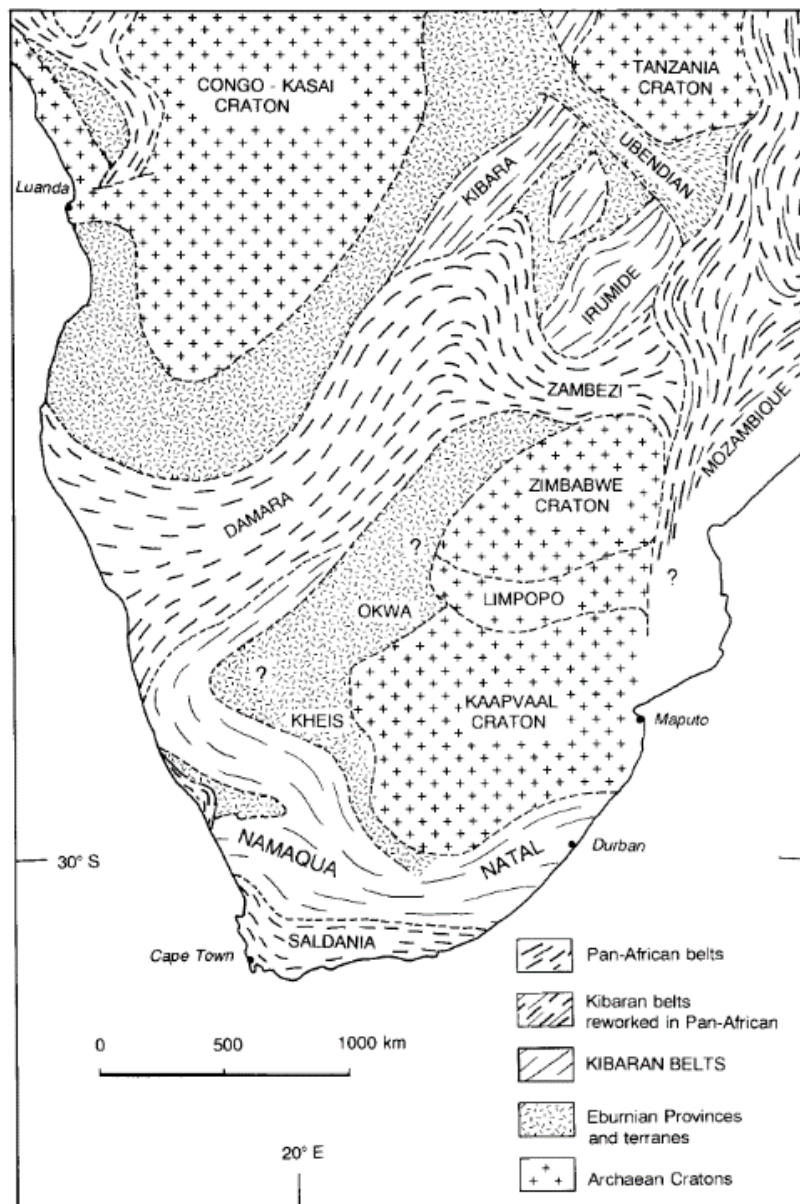
Figure 4-1. Sketch map of the tectonic framework of central and southern Africa, showing the distribution of Archaean cratons and Proterozoic mobile belt, copied from Figure 1 of Thomas et al, (1994).

Contraction was followed by extension in what can be described as the third major tectonic event in the region. In the Early Jurassic (~180 Ma), Gondwana began to breakup though a series of rifting events (Conrad and Gurnis, 2003; Watkeys, 2006; Broad et al., 2006). Rifting reactivated the Cape Fold Belt contractional fault system as extensional and transtensional faults, which was associated with the right-lateral rifting of the Agulhas-Falkland Fracture Zone, located offshore along the southeastern margin of South Africa (Broad et al., 2012). Unfortunately, the absence of Table Mountain Group strata across most of the site vicinity greatly hinders discernment of possible Mesozoic reactivation along the older basement faults in the Western Cape (De Beer et al., 2008). During Late Jurassic to Early Cretaceous extension, rifting initiated a series of grabens and half-grabens along the southern margin of Africa, including the Orange Basin (McMillan et al., 1997; Broad et al., 2006, 2012; Paton et al., 2006).

The last major events that shaped the region's geology were the Late Neogene to Recent sea-level fluctuations (Roberts et al., 2006). Along the coastline, bedrock is overlain by unconsolidated to semi-consolidated sequences of marine, estuarine, and aeolian deposits of the Sandveld Group that reach thicknesses of generally <20 m at Koeberg (Figure 4-2). Pedogenic silcretes and ferricretes, developed on weathered basement, are sporadically preserved inland beyond the reach of the Middle Miocene to Pliocene marine transgressions (De Beer et al., 2008). Section 4.4 provides a detailed description of the Sandveld Group sediments at the Duynefontyn site.
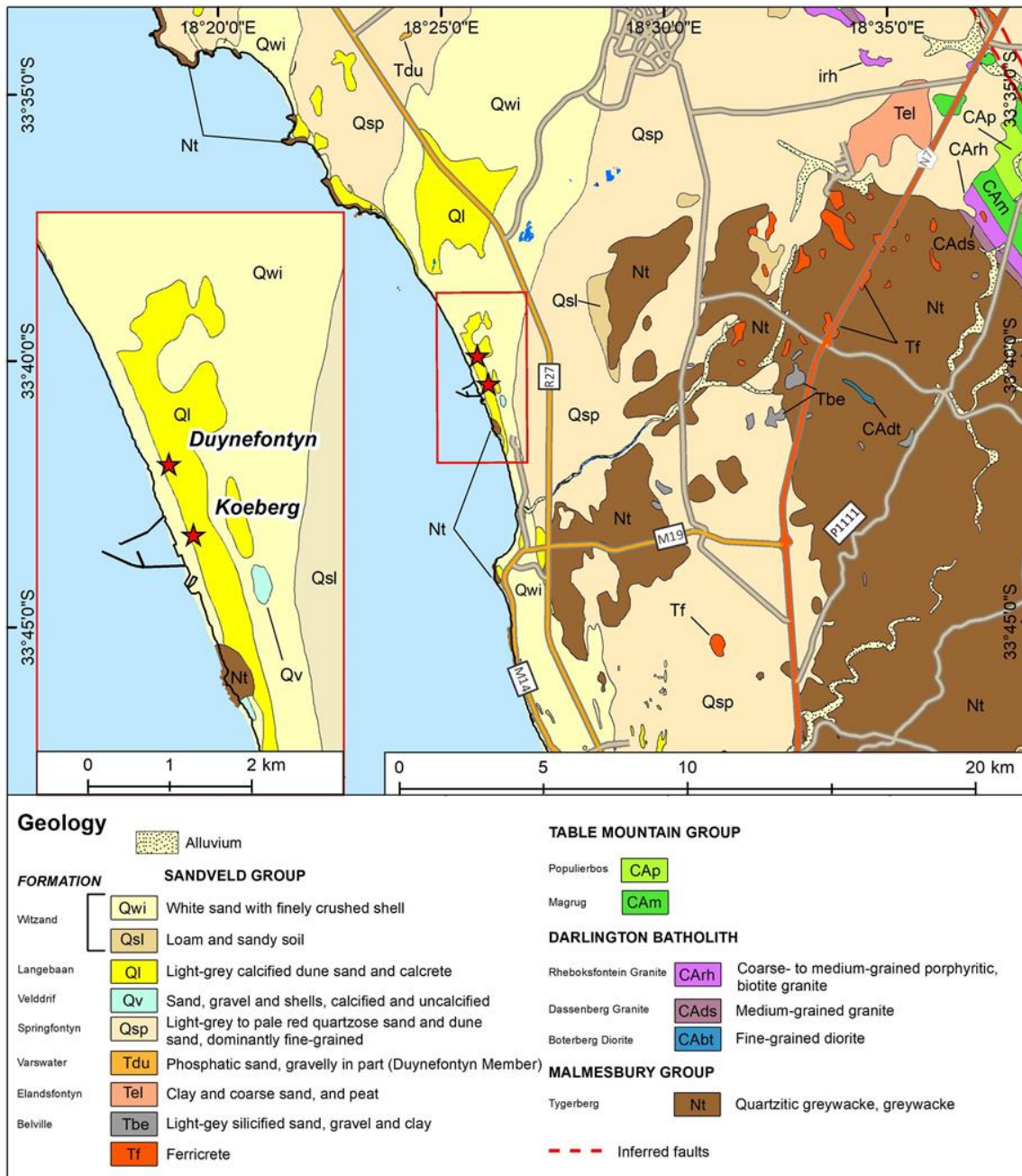

Figure 4-2. Lithostratigraphy in proximity of the KNPS. Duynefontyn and KNPS locations indicated by red stars on map and inset, reproduced from De Beer et al., 2008).

4.2 REGIONAL GEOLOGIC SETTING

The regional geology of the southwest coast of South Africa has been investigated by numerous authors (e.g., Van der Merwe, 1963; Visser and Schoch, 1973; Hartnady et al., 1974; Dames and Moore, 1975, 1976, 1977; Rogers, 1980; Von Veh, 1982; Theron, 1984, 1992; Day and Ridgway, 2000, 2006; Roberts, 2001; Kisters et al., 2002; Gresse et al., 2006; De Beer et al., 2008; Roberts et al., 2011, 2013; Roberts and Siegfried, 2014). This section provides a condensed summary of relevant findings from these and other studies with additional results derived from this PSHA (e.g., Claassen et al., 2024; Coppersmith et al., 2024) that highlight the lithostratigraphy and structural characteristics of the region surrounding the Duynefontyn site.

4.2.1 Lithostratigraphy

The geology of the region around Koeberg and Duynefontyn is mapped in detail at various published and unpublished scales ranging from 1:5000 to 1:250,000 (Beeson, 1973; Theron, 1975, 1984, 1990; Gresse, 1980; Roberts, 2001, 2002; Viljoen, 2008; Siegfried, 2008a,b; De Beer et al., 2008). Maps depict rocks ranging from the oldest Neoproterozoic basement of the Malmesbury Group to the youngest sediments of thick and extensive Late Holocene alluvium and soil cover (Figure 4-3). The low-grade metasediments and subordinate metavolcanic rocks of the Malmesbury Group (Tygerberg, Moorreesburg and Franschhoek Formations) include rhythmic alternations of greywacke, phyllitic shale, siltstone, immature quartzite, and a few thin impure limestone and conglomerate beds. These basement rocks are intruded by the Cambrian (550 and 510 Ma) Cape Granite Suite (e.g., Scheepers, 1995; Kisters et al., 2002; Scheepers et al., 2006), spatially subdivided into five batholiths, each with its own of assemblage of granites, granodiorite, diorite, and gabbro with a broad compositional range. The batholiths are cut by thin dykes of aplite, quartz porphyry, pegmatite, and microcrystalline aphanitic rocks of basaltic composition (Kisters et al., 2002; De Beer et al., 2008; Gresse et al., 2006). At ~515 to 520 Ma the coarse-clastic Klipheuwel Group, composed of an assemblage of immature shales, mudstones, sandstones, and conglomerate, was deposited in fault-bounded rift basins.

Late Proterozoic to early Palaeozoic extension formed an Atlantic-type passive margin along the southern edge of Gondwana, which allowed deposition of the Mid-Cambrian to Ordovician fluvial to shallow-marine and glacial sequences of the Cape Supergroup within the area. The Graafwater, Peninsula, and Pakhuis Formations of the Table Mountain Group comprise quartz arenite, siltstone, shale and diamictite (Theron et al., 1992; Thamm and Johnson, 2006). Within the 40 km radius around the Duynefontyn site, these rocks crop out southwest of Cape Town. Regionally extensive, predominantly NW-SE trending dykes assigned to the False Bay Dolerite Suite intruded rocks of the Malmesbury Group and Cape Granite Suite rocks along the SW Cape during the Early Cretaceous. A swarm of these dykes traverse the coastline between Milnerton and Bloubergstrand (e.g., Day, 1986; Reid et al., 1991; Theron et al.,1992).
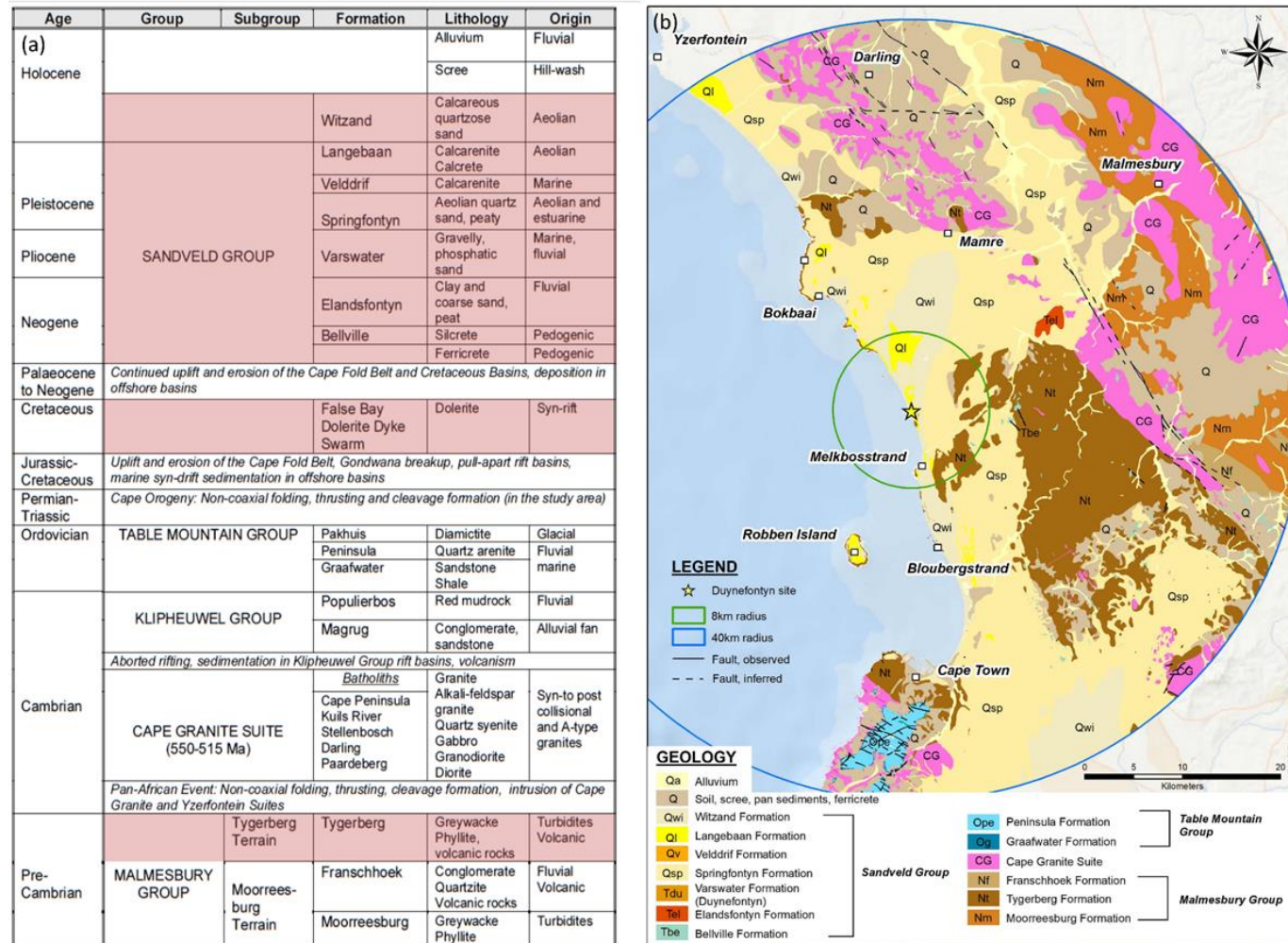
Figure 4-3. (a) Lithostratigraphy of the area within a 40 km radius of the Duynefontyn site (copied from De Beer et al., 2008). Lithological units highlighted in red are known to occur at both sites. (b) Geological map depicting the location of lithostratigraphic units within a 40 km radius around the Duynefontyn site (copied from De Beer et al., 2008).

The large majority of all these rocks are overlain by well-developed soil cover and Cenozoic sediments of the Neogene to Holocene Sandveld Group, composed of unconsolidated to semi-consolidated sequences of marine, estuarine, and aeolian deposits that attain thicknesses of more than 60 m in places (Rogers, 1980, 1982, 1983; Roberts, 2001; Roberts et al., 2006). Occurrences of silcretes (Belville Formation) and ferricretes are also developed on weathered basement and are sporadically preserved inland beyond the reach of the Middle Miocene to Pliocene marine transgressions (De Beer et al., 2008) (Figure 4-3)

4.2.2 Regional structural geology

Along the southwestern margin of South Africa and within the site vicinity, the structural geology is largely dominated by NW-SE striking, NE or SW steeply dipping (frequently >60°) Malmesbury Group rocks which are deformed in a succession of tight upright folds with axial planes trending NW to NNW. The SE-NW trending fold axes gently plunge NW with a weakly-developed axial plane cleavage (Dames and Moore, 1976; Theron et al., 1992; De Beer at al., 2008). NW-SE orientated, SW and NE steeply dipping strike-slip faults dominate (e.g., Colenso and Piketberg faults) (Figure 4-4). Generally shorter normal faults (e.g., the Mamre Fault) and localised reverse and thrust faults are also present. These fault and fold styles, as well as their orientation, change across this region towards the south coast across the Cape Fold Belt syntaxis where faults take on a mainly E-W and NE-SW orientation with a predominantly normal sense of fault displacement (e.g., Worcester Fault) and E-W trending folds. Detailed descriptions of the dominant structural geologic features are provided in Section 8.3 and 8.5. Figure 4-4b shows the regional and local stress data. The three main sources of stress data shown in the figure are structural geological mapping, borehole breakouts, and focal mechanism. The SSM TI Teams assessment of the regional stress is provided in Section 4.2.11 and Section 5.2.5.
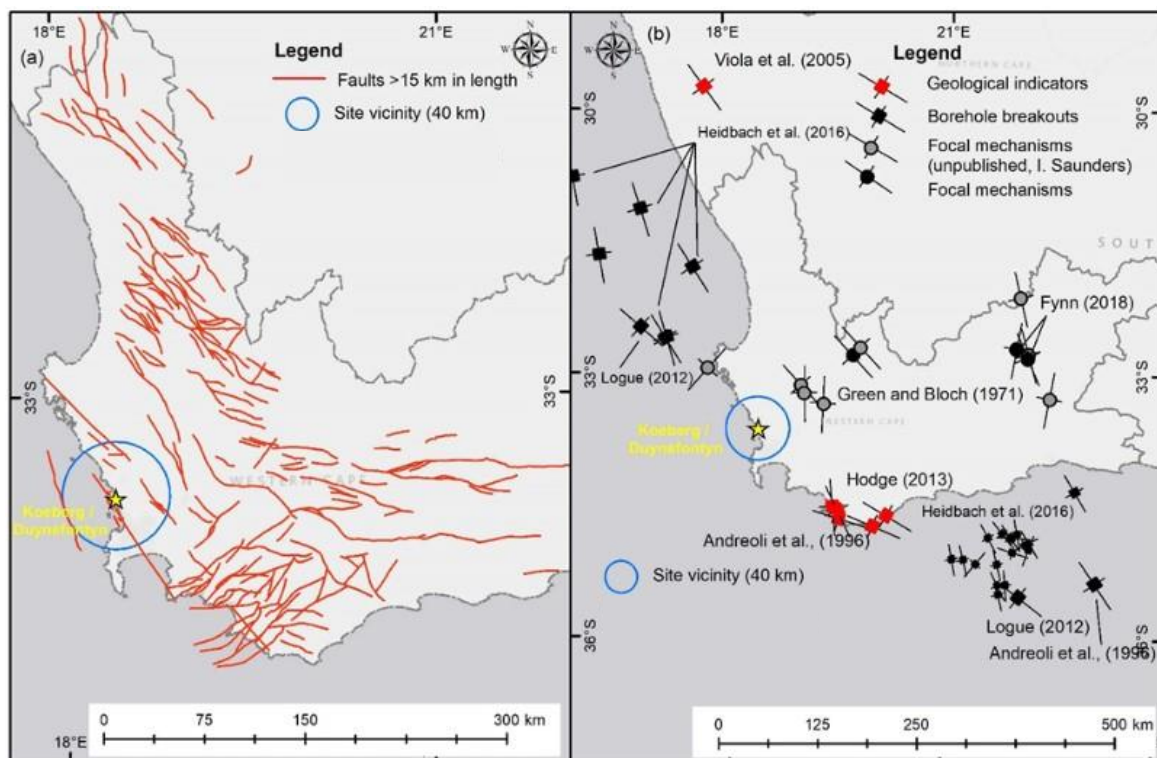

Figure 4-4. Map of (a) identified tectonic structures and (b) indicators of stress across the region.

4.2.3 Seismotectonic setting

In the Baseline PSHA report (Stamatakos et al., 2022), the SSM TI Team summarised the tectonic history based on the original three-terrane interpretation of Hartnady et al. (1974). This interpretation, which we have named the Proterozoic terrane model, was the accepted interpretation of Western Cape tectonic history for several decades (Kent, 1980) and was revisited by Gresse et al. (2006) in the most recent version of the Geology of South Africa book (Johnson et al., 2006). At Workshop 2, however, three alternative tectonic models were proposed by the proponent experts (Kisters, 2022; Tankard, 2022; Paton, 2022). The SSM TI Team has named these three models the 'accretionary prisms and fore-arc basin model', the 'Vredenburg Shear Zone Duplex model', and the 'lateral ramp on an inclined plate-margin detachment model', respectively. Table 4-1 summarises these three alternative tectonic models, in addition to the model relied on for the Baseline PSHA report. Table 4-1 also describes the tectonic models and identifies the key features of each interpretation, the technical bases, technical challenges, and the implications for the site hazard results.

However, it is important to recognise that the tectonic models are not used as direct inputs to the SSM. Rather, the tectonic models provide the SSM TI Team with base knowledge and a common understanding of the tectonic and geological framework of the Western Cape (and the uncertainties of that framework). This base knowledge and common understanding of the tectonic framework underlie and connect the more hazard-specific assessments needed to build and populate the SSM. For example, the SSM TI Team's assessment of seismogenic thickness or fault activity is based on earthquake data in the project catalogue or detailed geologic mapping of fault traces. However, the SSM TI Team's certainty (or uncertainty) in these specific assessments comes in part from how well (or how poorly) these assessments fit within the SSM TI Team's overall understanding of the tectonic and geological framework. Earthquake data or field observations that are compatible with the SSM TI Team's understanding of the tectonic framework may be judged by the SSM TI Team as reliable and credible. Data and field observations that conflict with the tectonic framework suggest that the given interpretation of the tectonic framework needs to be challenged by the SSM TI Team and may require additional study and verification.

The SSM TI Team's assessment of uncertainty in the SSM logic tree and HID inputs is also informed by an understanding of the range of possible tectonic interpretations. Because the four alternative tectonic models included in the current SSM TI Team's evaluation span a relatively broad range of tectonic interpretations, the SSM TI team will need to include sufficient uncertainty in many of the model inputs that are rooted in an understanding of the tectonic and geological framework. The alternative tectonic models used to form the base knowledge and common understanding of the tectonic and geologic framework of the Western Cape are summarised below and in Table 4-1. Discussions of the SSM implications and methods for model assessment are provided, followed by descriptions of geodetic and tectonic stress analyses that are considered within the tectonic and geological framework of the Western Cape.

4.2.4 Proterozoic terrane model

In this model, the Western Cape is underlain by the Saldania Belt, one of the Pan-African orogenic belts that mark the suture zones along which continental fragments were amalgamated during the Late Neoproterozoic to Early Palaeozoic construction of Gondwana

(Miller, 1983; Hartnady et al., 1985; Gresse and Scheepers, 1993; Frimmel et al., 1996; Frimmel and Frank, 1998; Rozendaal et al., 1999). The terranes include the Damara, Kaoko, Gariep and Saldania Belts, and record the main phase of collisional tectonism at ~550 to ~530 Ma (Frimmel and Frank, 1998; Fitzsimmons, 2000) (Figure 4-5).
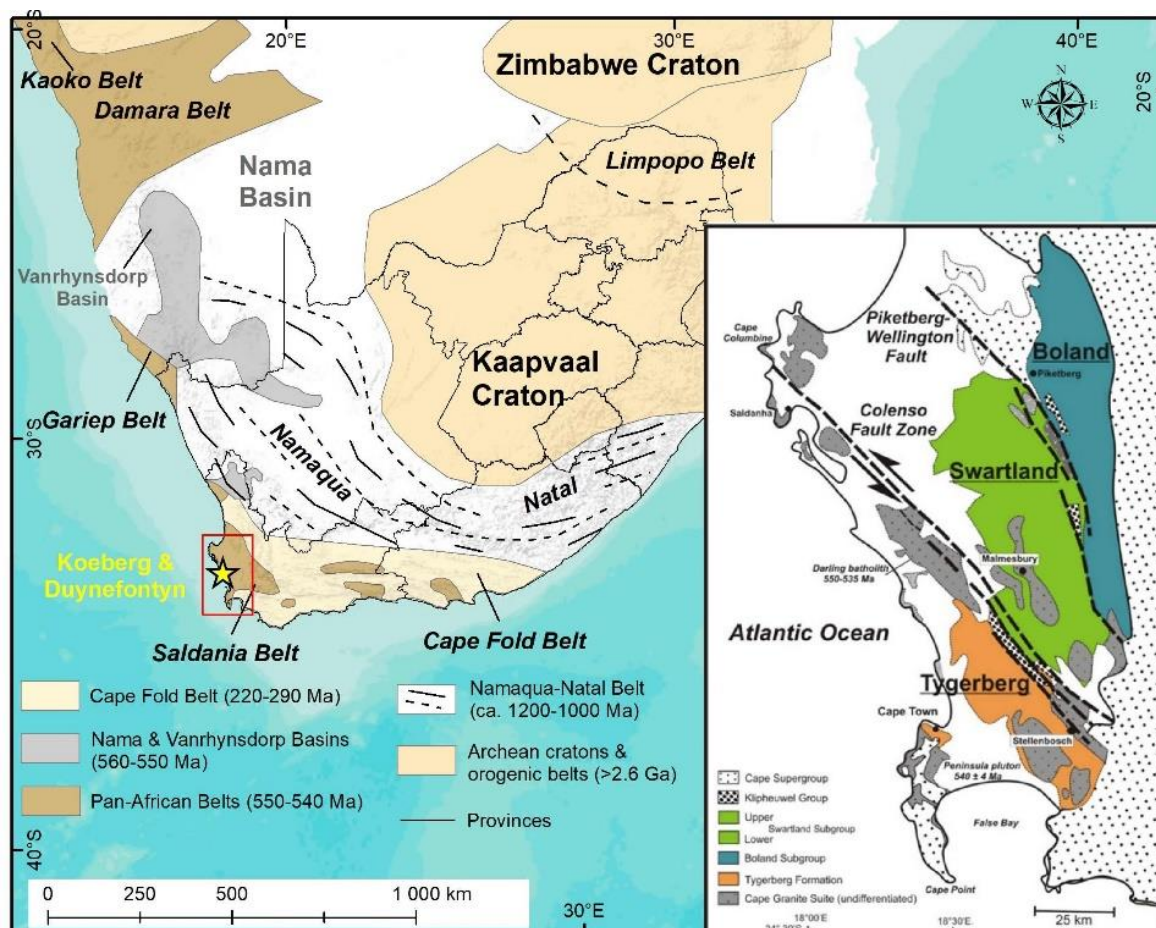

Figure 4-5. Map showing the large-scale seismotectonic features for the Proterozic terrane model, including cratons and orogenic belts in Southern Africa. Inset map shows the northern branch of the Saldania Belt and its simplified geology (after Scheepers, 1995; modified by Kisters et al., 2002).

The Proterozoic terrane model was first proposed by Hartnady et al. (1974), who suggested that the southwestern branch of the Saldania Belt comprises three allochthonous and para-allochthonous terranes (Tygerberg, Swartland, and Boland) that were amalgamated against the Kaapvaal Craton by a series of terrane-bounding transpressional strike-slip faults, including the Colenso and Piketberg–Wellington faults. These terranes are underlain by Meso- to Paleoproterozoic crystalline basement.

The terranes comprise low-grade metamorphic Neoproterozoic metasediments and subordinate metavolcanic rocks assigned to the Malmesbury Group that include rhythmic alternations of greywacke, phyllitic shale, siltstone, immature quartzite, and a few thin impure limestone and conglomerate beds. The Proterozoic terrane model separates the three sub-sections according to how they are dissected by the two regional fault systems, the distribution of deposits on geological maps, as well as some noted changes in the structural style among the three terranes.

4.2.5 Accretionary prisms and fore-arc basin

At Workshop 2, Professor Alex Kisters proposed a tectonic model in which the Western Cape originated as an accretionary prism akin to the present-day subduction tectonics along the Indonesian archipelago (Figure 4-6). The details of this interpretation are laid out in Kisters and Belcher (2018). In this tectonic model, the Neoproterozoic tectonic assemblages that were interpreted as allochthonous terranes by Hartnady et al. (1974) are reinterpreted as autochthonous relics of a Late Neoproterozoic convergent margin. Kisters and Belcher (2018) divided the Neoproterozoic stratigraphy into two structural units: a lower domain (Swartland Complex) comprising an imbricate stack of marine sediments and relic ocean crust, overlain by a less deformed domain (Malmesbury Group) comprising shales, phyllites, and metagreywackes, and thin limestones and conglomerates that were folded into tight west-trending upright to southwest-verging folds. Tectonic underplating during subduction in the deeper parts of the prism and deposition of fore-arc sediments at higher structural levels are contemporaneous between >560 Ma and at least 520 Ma.
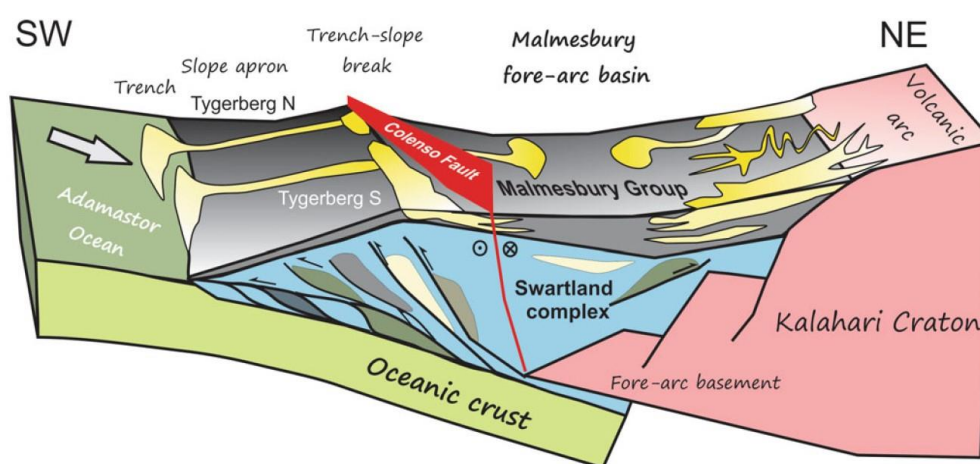

Figure 4-6. Schematic illustration showing the different lithological and structural elements of the Tygerberg prism and Malmesbury fore-arc with respect to the Kalahari Craton[1], from Kisters and Belcher (2018, Figure 14.9). The Swartland Complex corresponds to the Swartland Subgroup in the inset map legend of Figure 4-5.

The key evidence supporting this interpretation comes from a detrital zircon study by Frimmel et al. (2013), which demonstrates within the margin of error that rocks of the two domains are identical in age, and thus simply represent two different structural levels of the same fore-arc complex. The Swartland Complex exposes the upper parts of the accretionary prism while the overlying Malmesbury Group is the remnant (albeit deformed) fore-arc basin resting atop the accretionary prism. In this model, the Colenso Fault is recognised as a regional-scale fault or fault zone that originates within the accretionary prism, but it is not a terrane boundary. The Colenso Fault is the primary fault separating the continental crust (upper domain) from the accretionary prism (lower domain). Frimmel et al. (2013) suggest that the Piketberg Fault represents the major terrane boundary in the western Saldania Belt. Although not

---

[1] The Kalahari Craton consists of two cratons separated by the Limpopo Belt: the larger Kaapvaal Craton to the south and the smaller Zimbabwe Craton to the north. The Namaqua Belt is the southern margin of the Kaapvaal Craton.

characterised as such in Kisters and Belcher (2018), the Piketberg-Wellington Fault, in this model, could be interpreted as the tectonic backstop of the accretionary wedge against the craton.

4.2.6 Vredenburg shear zone duplex

The Vredenburg Shear Zone Duplex model, developed by Dr Anthony (Tony) Tankard, is not yet published but was presented at Workshop 2. This model proposes a deep pan-African crustal structure, dating back to the Neoproterozoic-Early Cambrian assembly of western Gondwana (Figure 4-7). Dr Tankard proposes that there is a deep primary controlling north–south structure, which he calls the Vredenburg Shear Zone (VSZ).
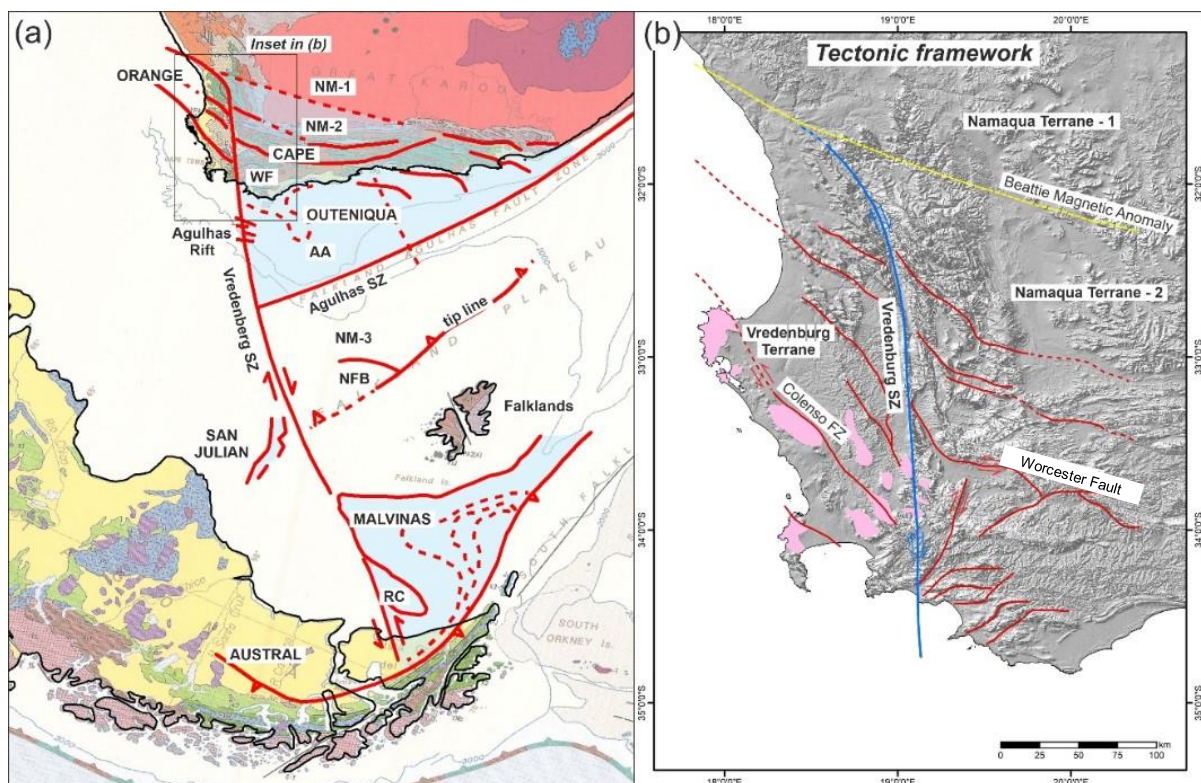

Figure 4-7. The Vredenburg Shear Zone model proposed by Dr Tony Tankard at Workshop #2. (a) The VSZ is a controlling primary tectonic structure (right lateral transform fault) that placed South America against Africa during the assembly of Gondwana. At the regional scale (b), there are no surface manifestations of the VSZ, but Riedel and conjugate Riedel shear structures of the model are manifest as the Colenso and Worcester faults, among other mapped faults.

The VSZ is interpreted as a basement shear zone above which a suite of linked and rotated faults occur in the cover sequence. The width of the shear zone may vary by up to several kilometres, which Dr Tankard attributes to the blank space or corridor on the 1:250,000 geological sheets of the Western Cape in the vicinity of the syntaxis that separates two disconnected sets of structures. There is no surface expression of the VSZ or principal displacement zone, but measurable offsets of associated structures are present, with surface displacement of generally less than one kilometre. The Colenso Fault Zone is one of several associated Riedel shear structures.

The VSZ and the Colenso Fault now occur at the trailing edge of this structural complex, and at the southern part of the onland portion of the structure (Figure 4-7b), and Tankard proposes

that these two structures are the principal focus of recent seismic activity in the southwestern Cape. In his model, Dr Tankard cites the interplay of synthetic shears (Riedel structures) and antithetic shears (conjugate Riedels) on mapped geological structures in the Western Cape.

Dr Tankard cites the following evidence for his model:

- Zircon xenocryst ages of 2.0 Ga in the Vredenburg and Darling granites (dated by Rozendaal et al., 1999) suggest the origin of the Vredenburg basement may have been derived as a fragment of the Rio de la Plata craton of northeast Argentina. Dr Tankard suggests that Rio de la Plata-type basement was accreted during Gondwana assembly and is believed to underlie the Malmesbury platform and western edge of the Cape Fold Belt up to the VSZ.

- There is an intermediate zone where the antithetics are inverted by a suite of reverse faults. This can be observed on the geological map, where the western end of the Worcester fault bends northwards.

- At Caledon, a structural complex that forms a 'pop-up structure' was compared with the sandbox modelling of McClay and Bonora (2001). Tankard's explanation of a pop-up is that the fault system comprises a jog or offset in the trace of the strike-slip fault. In this case, uplift occurred where the dextral fault system met a left-stepping jog.

- Although there is a scarcity of subsurface data, Dr Tankard interprets the vertical shape of the Colenso Fault as a listric, down-to-the-southwest fault, rather than a planar fault. He infers that reflection seismic profiles from comparable areas show that anything other than listric would have created 'space problems.'

- The Late Cambrian Klipheuwel Basin and its structural architecture provide an important template for basin evolution along the Colenso Fault Zone. At its southeastern end, the Colenso Fault Zone consists of a principal strike-slip fault as well as a secondary synthetic fault to accumulate the strain, thus accommodating the Klipheuwel Basin. It is a useful yardstick to compare with the Langebaanweg and Elandsfontein deposits. This synthetic fault is expressed as a magnetic lineament. The angular deviation of the synthetic fault to the principal fault zone is ~15°, typical of a synthetic shear. Dr Tankard attributes the magnetic lineament to magmatism, such as a basic dyke, along the synthetic fault plane which occurs because the role of the synthetic and antithetic faults is to conserve strain. Translation along the Colenso Fault Zone included a component of uplift. This is also observed in unroofing of the Darling granite along strike (Figure 4-5 inset).

Dr Tankard interpreted relatively recent geologic deformation in the area he mapped based on a series of Cenozoic deposits along the Colenso Fault Zone, including the Langebaanweg and Elandsfontein phosphate deposits and underlying wetland accumulations. The Elandsfontein phosphate deposits are found in the present at the Kropz phosphate mine. Clay-cake deformation models (Groshong, 1989) together with a display from Mandl (1988) were re-oriented to match the Langebaanweg geology. The inboard peak of the accumulation, isopached based on phosphorous pentoxide (P_2O_5) percent, presently occurs at an elevation of 52 m above present sea level (Tankard, 1974). This elevation has been structurally restored, showing that the pre-deformation height was 21 m asl (above sea level). As a secondary check, chronological equivalents at Sandheuwel (Saldanha Bay) and Koingnaas confirmed this pre-deformation elevation of 21 m. This implies that the Mid-Pliocene sea-level

was at 21 m asl, whereas the world average is 22 m asl. Uplift of the Langebaanweg and Elandsfontein Early Pliocene sediments across the Colenso Fault Zone is therefore believed to have occurred in the Late Pliocene to Early Pleistocene. More importantly, it involved ~30 m of structural uplift along the Colenso Fault in an inferred time span of about 1.5 Ma. There were no geochronological dates on these deposits to verify the proposed uplift rate. Furthermore, the intervening Miocene-Pliocene unconformity is mapped in the offshore Orange Basin, where it is dated at 5.5 Ma.

4.2.7 Lateral ramp on an inclined plate-margin detachment

Based on extensive analysis of mainly offshore seismic images and cross-section restoration across the southern coast of South Africa presented at Workshop 2, Dr Douglas Paton proposed a seaward-dipping regional detachment model that was formed in the Neoproterozoic during the assembly of Gondwana (Figure 4-8). This detachment has continued to play a role in subsequent phases of tectonism, including the break-up of Pangaea and Gondwana and the subsequent transition from rift to drift to passive margin tectonism throughout the Mesozoic and Cenozoic.
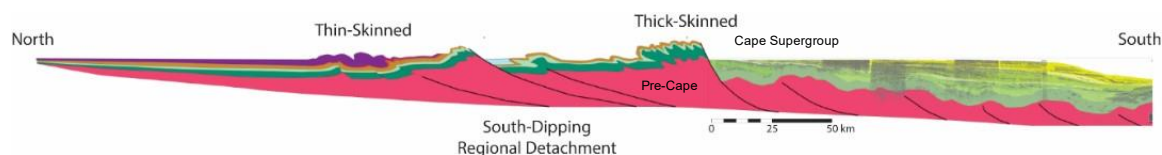

Figure 4-8. Composite cross-section from the southern Karoo Supergroup (left), through the Cape Fold Belt (centre), to the offshore Mesozoic extensional basins (right), redrafted from slide #50 of Dr Paton's Workshop #2 presentation (Paton, 2022).

In these restorations, Dr Paton documents a change in structural style from thin-skinned shortening inboard, where the crustal detachment is shallow, to thick-skinned shortening outboard, where the crustal detachment is deeper. The thin-skinned deformation is characterised by northward-verging thrust sheets on low angle faults, while the thick-skinned shortening is characterised by steep basement-cored faults and large box folds in the cover rocks. Dr Paton also showed similar structural and stratigraphic relationships that appear to be preserved in the Falkland Islands and Patagonia, which were juxtaposed against South Africa as part of Gondwana, and thus share a common tectonic evolution to South Africa. Extension during the breakup of Gondwana was accomplished by reactivation of the contractional faults as transpressive strike-slip faults, and reactivation of the normal faults as transtensional strike-slip faults.

Although a detailed analysis of similar data was not available for the west coast of the Western Cape, Dr Paton extended his interpretation of a seaward-dipping detachment based on his reconstruction of the various tectonic plates and micro-plates prior to the breakup of Gondwana. An important distinction in his model is that the Western Cape is highly oblique to both convergent and divergent plate motions, unlike the southern to south-eastern margin of South Africa. In addition, Dr Paton interprets the SW part of the coastal region of the Western Cape as resting atop a large southwest-dipping lateral ramp (Figure 4-9) within the detachment zone. The region is therefore dominated by margin-parallel strike-slip and oblique strike-slip deformation. In this model, the lateral ramp constitutes a deep-rooted tear fault.

Based on his model, Dr Paton explains the nearly orthogonal sets of mapped faults in the syntaxis as coeval conjugates or orthogonal fault sets that reflect the underlying geometry of a seaward-dipping detachment over its lateral ramp.
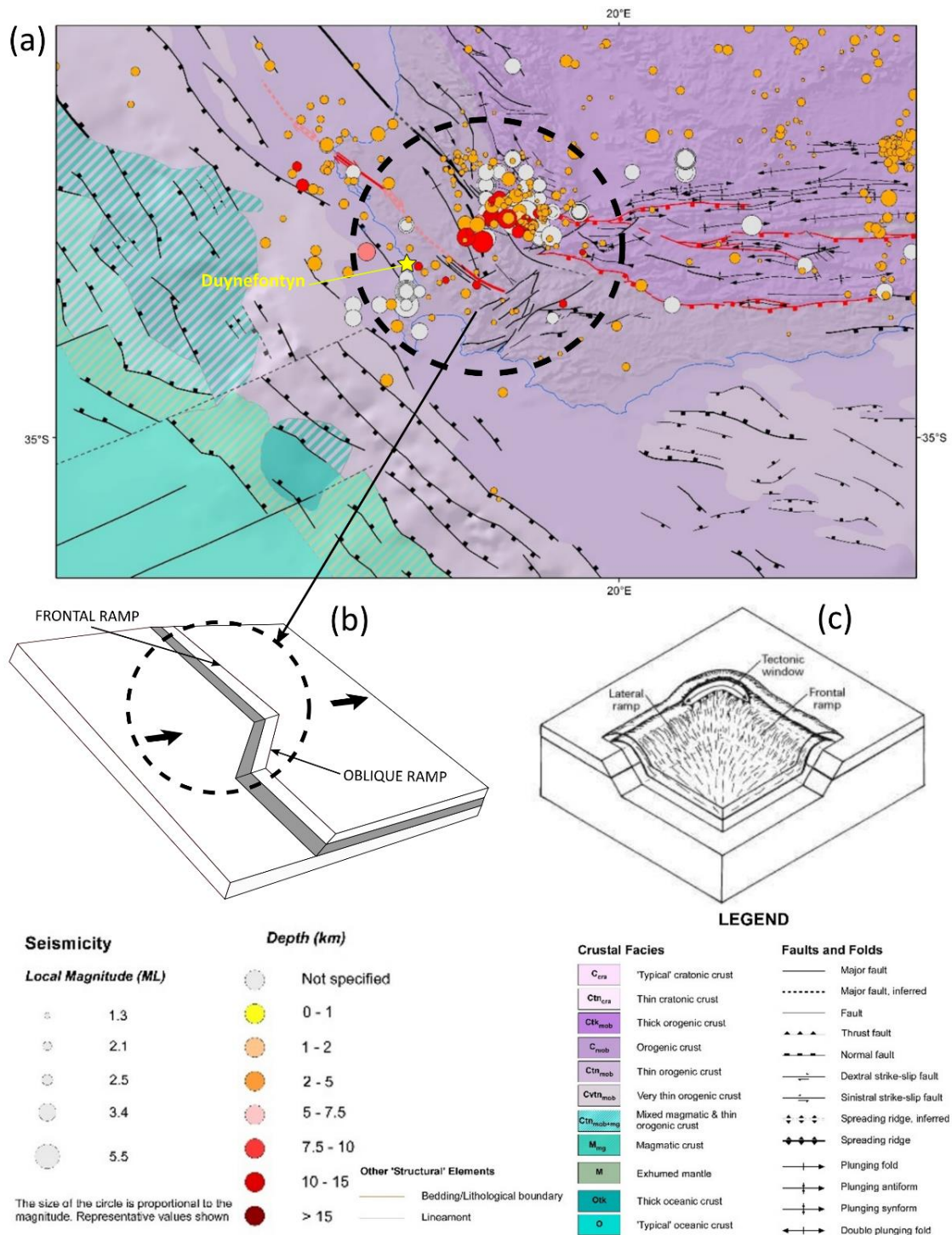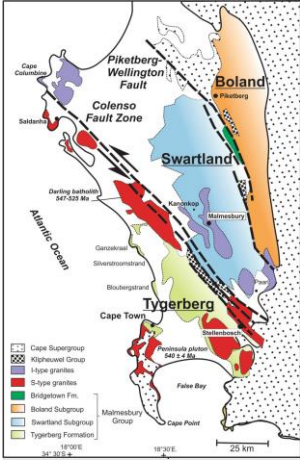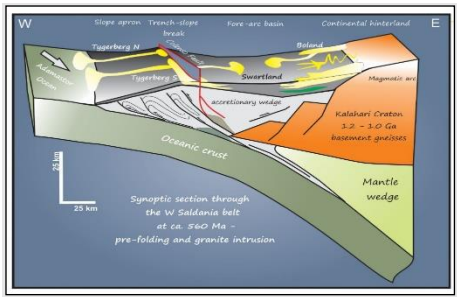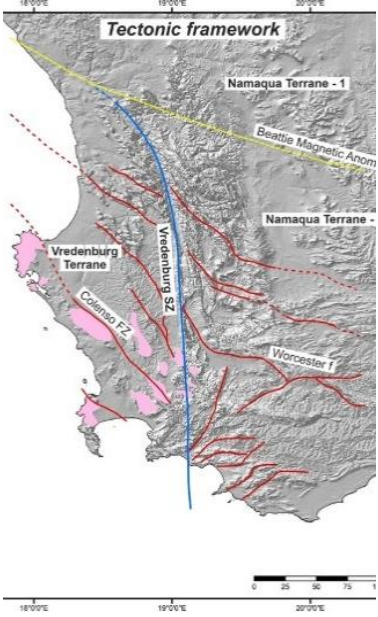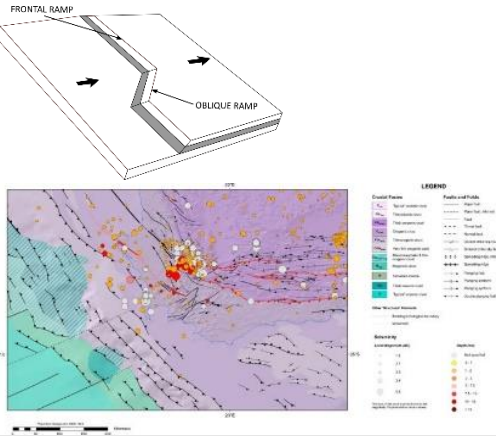

Figure 4-9. Lateral ramp tectonic model presented by Dr Paton at Workshop #2. (a) Geological map of the Western Cape showing the location of earthquakes in the syntaxis, from Markwick et al. (2021). (b) Diagram showing the three-dimensional (3D) footwall ramp structure, after Figure 10 of McClay (1992). (c) Diagram showing how orthogonal fault sets form above a lateral thrust ramp, from https://pubs.usgs.gov/bulletin/b2163/html/fig33.html.

An interesting alternative to the lateral ramp concept proposed by Dr Paton, is a hypothesis of the Syntaxis as an orocline that formed in response to dextral transpression along the continental margin (Johnston, 2000). This interpretation uses a similar tectonic reconstruction as that proposed by Dr Paton. In this interpretation, the east-west Cape Fold Belt, including the Falkland Islands, formed a 300 km left-step within the dextral shear zone (similar to a restraining bend along a strike-slip fault system but much larger). According to this model, dextral margin-parallel translation of the crustal blocks outboard of the orogen was accommodated by strike-slip deformation in South America and Antarctica, and inboard of the margin by convergence along the east-west portion of the Cape Fold Belt and the growth of its foreland-verging fold-thrust structures (Figure 4-8). In this interpretation, the Syntaxis (and its counterpart, the Port Elizabeth Antitaxis) are oroclinal bends in the Cape Fold Belt that developed in response to two large rotations of the Falkland Islands, a 90° clockwise rotation during plate convergence followed by a 60°-70° clockwise rotation from shear along the Agulhas-Falkland Fracture zone during the break-up of Gondwana. This interpretation is however at odds with the conventional interpretation in which the Falkland Island rotations are considered to post-date the Cape Fold Belt. This age constraint on the rotations is based on palaeomagnetic data, which show that these rotations took place sometime after 190 Ma (Mitchell et al. 1986; Taylor and Shaw, 1989).

Table 4-1. Summary of tectonic models following Workshop #2.

Model	Conceptual Image	Key Features	Technical Basis	Technical Challenges	Implications for Hazard
Proterozoic terrane [Hartnady] [Baseline PSHA report]		Three terranes amalgamated along transpressive northwest–southeast-trending shear zones. Post-amalgamation intrusion of large granite plutons.	Geological mapping revealed subvertical, northwest-southeast strike-slip (SS) faults with intensely mylonitised and brecciated rocks, that separate terranes. These SS faults have been interpreted as the terrane boundaries.	Gleaning direct evidence of recent (Quaternary) faulting and seismicity along any one of these shear zones from the geological record. Integration of the tectonic model with other data e.g., heat flow, gravity, magnetics.	Active faulting primarily occurs as reactivation on a subset of these early faults, those that are optimally oriented for slip in the current stress regime.
Accretionary prism and fore-arc basin [Kisters]		The Western Cape is a relict accretionary prism and fore-arc basin developed by sinistral Gondwana transpression. The Colenso Fault (which dips to the northeast in this model) is the primary fault separating the continental crust (upper domain) from the accretionary prism (lower domain).	Strong differentiation in metamorphic grade within the Malmesbury strata between the accretionary prism and fore-arc. Similar detrital zircon ages for strata across the belt indicating a common depositional setting.	How can this be differentiated from the terrane model? Integration of the tectonic model with other data, e.g., heat flow, gravity, magnetics.	Primarily SS earthquakes on reactivated Colenso Fault or parallel structures. The model divides the Western Cape crust along the Colenso Fault. Clear delineation between deep crust and shallow crust. Deep earthquakes east of the Colenso Fault.

Model	Conceptual Image	Key Features	Technical Basis	Technical Challenges	Implications for Hazard
Vredenburg Shear Zone Duplex [Tankard]		Western Cape faulting is controlled by a cryptic north–-south-oriented shear zone at depth with a detached (partially coupled?) cover of Riedel (R) and anti-Riedel (R') faults. Depth to detachment is about 6–8 km. In this model the Colenso Fault dips to the southwest.	Geometry of mapped faults and basins along the Vredenburg Shear Zone mimics features produced by clay-cake models. Zircon xenocryst ages of 2.0 Ga in the Vredenburg and Darling granites (dated by Rozendaal et al., 1999) suggest the origin of the Vredenburg basement may have been linked to the Rio de la Plata craton of northeast Argentina.	The shear zone is not visible/ evident in the cover sequence (difficult to verify). Buried shear zone models imagine a wide variety of surficial deformation that, in and of themselves, are non-unique to the shear zone itself. Integration of the tectonic model with other data, e.g., heat flow, gravity, magnetics.	Partitioned (and thus smaller M) seismicity between cover and shear zones. The shear-zone is a 5–10 km wide zone of anastomosing faults. R and R' structures are active normal and reverse faults in the cover, including the Colenso.

Model	Conceptual Image	Key Features	Technical Basis	Technical Challenges	Implications for Hazard
Lateral ramp on an inclined plate-margin detachment [Paton]		Western Cape is a lateral ramp along a reactivated convergent-divergent plate margin (see Figure 4-8). The lateral ramp leads to SS faulting parallel to the plate margin. Plate margin is inclined seaward. Syntaxis is an overlapping network of orthogonal faults reflecting the later ramp architecture.	Consistent plate-scale deformational history based on detailed cross-sections and linked to tectonic history (e.g., assembly and break-up of Gondwana/Pangaea). Explains the thin and thick-skin crust.	Identifying a similar tectonic history developed for the Southern Cape from offshore 2D seismic profiles. Integration of the tectonic model with other data, e.g., heat flow, gravity, magnetics.	Primarily SS earthquakes on margin-parallel faults. Seismogenic depth shallows to the west, consistent with tapered plate margin. Earthquakes occur on reactivated structures.

4.2.8   Implications for the SSM

Alternative tectonic models are not usually segregated in the SSM logic tree as distinct branches. Rather, the models are used to support the SSM TI Team's assessment of various aspects of the model that are captured as logic-tree inputs, such as seismogenic thickness or Mmax and their uncertainty. Specifically, for the Duynefontyn SSHAC EL-2, the SSM TI Team assessed the following aspects of the SSM based on the four tectonic models.

- <u>Source zone boundaries</u>: Source zone boundaries are often defined by important crustal features. Most important are considerations of differences in crustal properties, crustal thickness, changes in the structural grain or types of faulting, and whether the crust was involved in Mesozoic extension. Identification and characterisation of these kinds of features requires a firm understanding of the tectonic forces that produced these features. A detailed description of the SSM TI Team's approach and criteria for defining source zone boundaries is provided in Sections 8.1 and 8.3.

- <u>Orientation and geometry of ruptures in the virtual fault generator:</u> To generate site-to-event distances appropriate for use with most modern GMPEs, potential future earthquakes generated from zones within 100 km of the site were modelled on virtual faults. To model the virtual faults, the SSM TI Team needed a technical basis to define the location, size, geometry, orientation, and style (normal, reverse, strike-slip) of these virtual ruptures, as described in Section 8.2.5. The approach adopted by the SSM TI Team was to assume that these ruptures would most likely be reactivations of existing bedrock faults. Thus, the mapped surface pattern of existing faults that are optimally oriented in the current stress field (see Section 4.2.11) were used to develop the input distributions of virtual faults. However, the VSZ model, and to some extent the lateral ramp model, predict that a broader distribution of surface faults may be involved. Movement on the VSZ may result in reactivation on the western set of northwest–southeast faults. In this model, the VSZ and perhaps the Colenso Fault are the principal foci of recent seismic activity in the southwestern Cape. The proximal trailing-edge margin or Riedel shear closest to the VSZ may be more susceptible to reactivation, especially faults such as the Colenso and southern trace of the VSZ. Farther away from the trailing edge, towards the distal end of the Riedel or conjugate anti-Riedel shears, the yield strength of the crust and its tectonic fault structures caused by buttressing may dampen the risk of earthquakes. This aspect of the seismotectonic framework informed the SSM TI Team's broader range of fault orientations and styles of faulting used in the virtual fault generator.

- <u>Crustal type:</u> Many of the models relied on to generate inputs to the distributions for Mmax (Section 8.2.9) and the magnitude-frequency distribution for the source zone (Sections 8.2.10 and 8.4.6) depend, in part, on how the crust is classified. Specifically, the SSM TI Team classified the crust as stable continental and determined whether this crust can be considered highly extended by the Mesozoic breakup of Pangaea and Gondwana. The SSM TI Team assessed the crustal properties of the source zones considering the differences among the four tectonic models. The SSM TI Team concluded that the crust of the Western Cape shares properties with Stable Continental Regions (SCRs) around the world (see Section 8.2.2 for more details about SCRs). SCRs are defined as regions of continental crust that have not experienced major tectonism, magmatism, basement metamorphism,

or anorogenic intrusion since the early Cretaceous (~145 Ma), and no rifting or major extension or transtension since the Palaeogene (~60 Ma). In this assessment, the SSM TI Team noted that the Duynefontyn site is approximately 2,000 km from the nearest active plate margin and underlain by Precambrian metasedimentary and crystalline strata with no known major deformation in the Neogene and Quaternary periods (~23 Ma). The SSM TI Team believes that the largest historical earthquakes (i.e., 1809 and 1969) occurred on faults within the crust that didn't rupture the surface or otherwise did not leave evidence of their rupture. For source zones off the west coast of South Africa, and the Orange Basin in particular, the crust is considered by the SSM TI Team to be Mesozoic extended crust. In addition, the SSM TI Team evaluated the information about crustal type provided by Dr Brandt at Workshop 2, and related information, including recent tomographic studies of southern Africa (Fadel et al., 2018; White-Gaynor et al., 2020; White-Gaynor et al., 2021; Afonso et al., 2022), Pn arrivals in southern Africa (Kwadiba et al., 2003), aftershocks (Marimira et al., 2021; Shumba et al., 2020; Yang and Chen, 2008), and the **M** 6.5 Botswana earthquake of April 2017 (Chisenga et al., 2020; Gardonio et al., 2018; Kolawole et al., 2017; Midzi et al., 2018; Moorkamp et al., 2019; Mulabisana et al., 2021).

- <u>Seismogenic thickness:</u> Seismogenic thickness is typically determined from the depth distribution of recorded earthquakes in the project earthquake catalogue (Section 8.2.2). Specifically, the depth distribution of the recorded earthquakes is plotted as a cumulative distribution, and the depth corresponding to the 90% probability value (D90) is then taken as the seismogenic thickness (e.g., Pacific Northwest National Laboratory [PNNL], 2014). However, because the earthquake record in the Western Cape is relatively sparse, a reliable depth distribution cannot be determined. Thus, the SSC TI Team relied on analogue regions where there is sufficient data to develop a reliable estimate of the seismogenic thickness. The technical basis for selecting appropriate analogue settings comes from an understanding of the nature of the crust.

4.2.9   Assessment methods

The complex geological and geophysical character of the Western Cape makes identification of a single seismotectonic model difficult. Many of the geological features observed at the surface, or interpreted from offshore seismic images, could equally be attributed to the tectonic driving forces from several of these tectonic models. For example, normal faults observed in the syntaxis could arise from the complex shear generated at the top of a lateral ramp, or from the flower structures generated above the buried VSZ. Thus, the SSM TI Team needed to maintain a broad perspective of alternative conceptual models to ensure that the full range of uncertainty was included in the hazard calculations to capture the CBR of TDI. Each diagnostic feature of the alternative conceptual models was carefully evaluated against the full range of existing geological, geophysical, and seismological information.

The assessments began with a summary of the existing tectonic model information presented at Working Meeting 2 for the SSM TI Team to discuss and assess. In this presentation and discussion, the SSM TI Team integrated the tectonic models with other data (e.g., geodesy, heat flow, gravity, and magnetics) and identified areas of agreement and incompatibility. Based on this assessment, the SSM TI Team produced a range of fault scenarios at Working

Meeting 3, consistent with each of the tectonic models, and evaluated those against geological, geophysical, and seismological data.

A critical component of the assessment was to evaluate results generated by the PSHA support studies (DDCs). This assessment included:

- Marine multibeam bathymetry data in Table Bay and False Bay;
- Recent field investigations of the Colenso Fault, where Tony Tankard indicated he found evidence for geologically recent deformation when the phosphate mine at Langebaanweg was active (1980s);
- Evaluation of microseismic data recorded by a temporary network, composed of seven stations, installed along the Colenso Fault;
- Results from the marine terrace data;
- Reprocessed seismic images from offshore data obtained from the Petroleum Agency of South Africa (PASA);
- 3DStress™ analysis supported by a database of stress indicators (Green and Bloch, 1971; Stacey and Wesseloo, 1998; Hodge, 2013; Fynn, 2018; Heidbach et al., 2018); and
- Remote sensing mapping with field verification for fault scarps.

Regarding the marine terrace studies, two points that garnered specific attention from the SSM TI Team were: (1) constraints on landscape uplift and (2) a comprehensive review of past sea-level fluctuations in the southwestern Cape, such as the recent work of Hearty et al. (2020). The marine terrace investigation (Claassen et al., 2024) addressed these two points. This study provided a basis for evaluating the stability of coastal geomorphic features and processes.

Regarding the offshore seismic images, the SSM TI Team acquired 48 seismic profiles from Cape Columbine to Cape Agulhas, and from the inner- to mid-continental shelf to the base of the continental slope from PASA. With these data, the SSM TI Team was able to construct regional onshore-offshore geological cross-sections spanning the northern extent of the Cape Fold Belt through the offshore Mesozoic Orange Basin (see Section 5.2.6) to evaluate the potential for recent offshore fault activity and to compare to cross-sections from the Cape South Coast through the Outeniqua Basin by Paton et al. (2006).

Regarding heat flow, the SSM TI Team evaluated the study from Dhansay et al. (2017) where they utilised subsurface temperature and heat flow measurements to determine potentially anomalous geothermal gradients, as described in Section 8.2.2.

4.2.10 Geodetic data

Geodetic measurements, especially Global Positioning System (GPS) data, can also be an important constraint in evaluating the seismotectonic framework in SSHAC PSHA studies (e.g., BC Hydro, 2012). GPS data for South Africa can be obtained from TrigNet, which is a network consisting of approximately 65 (mostly) continuously observing stations across the country with an average distance of 200 km between stations, and locally more dense station configurations of approximately 70 km around Cape Town, Johannesburg, and Durban (Figure 4-10). GPS data is also available from the International Global Navigation Satellite System (GNSS) Service (IGS).

GPS data for South Africa is reported in Malservisi et al. (2013), which shows that the South African region is rigid within the measurement uncertainties, with present strain rates on the order of 1 nanostrain yr^{-1}. The Cape Town region exhibits a slightly higher strain rate, with a north westerly direction relative to the stable Karoo region. However, Malservisi et al. (2013) determined that a significant part of the observed "higher" strain rate may actually be related to human activity such as agriculture and mining or increased noise due to atmospheric water vapour. Based on this analysis, Malservisi et al. (2013) concluded that unless these noise effects can be isolated, they could not definititively estimate small deformations from the GPS data that arise from tectonic processes within the Western Cape.
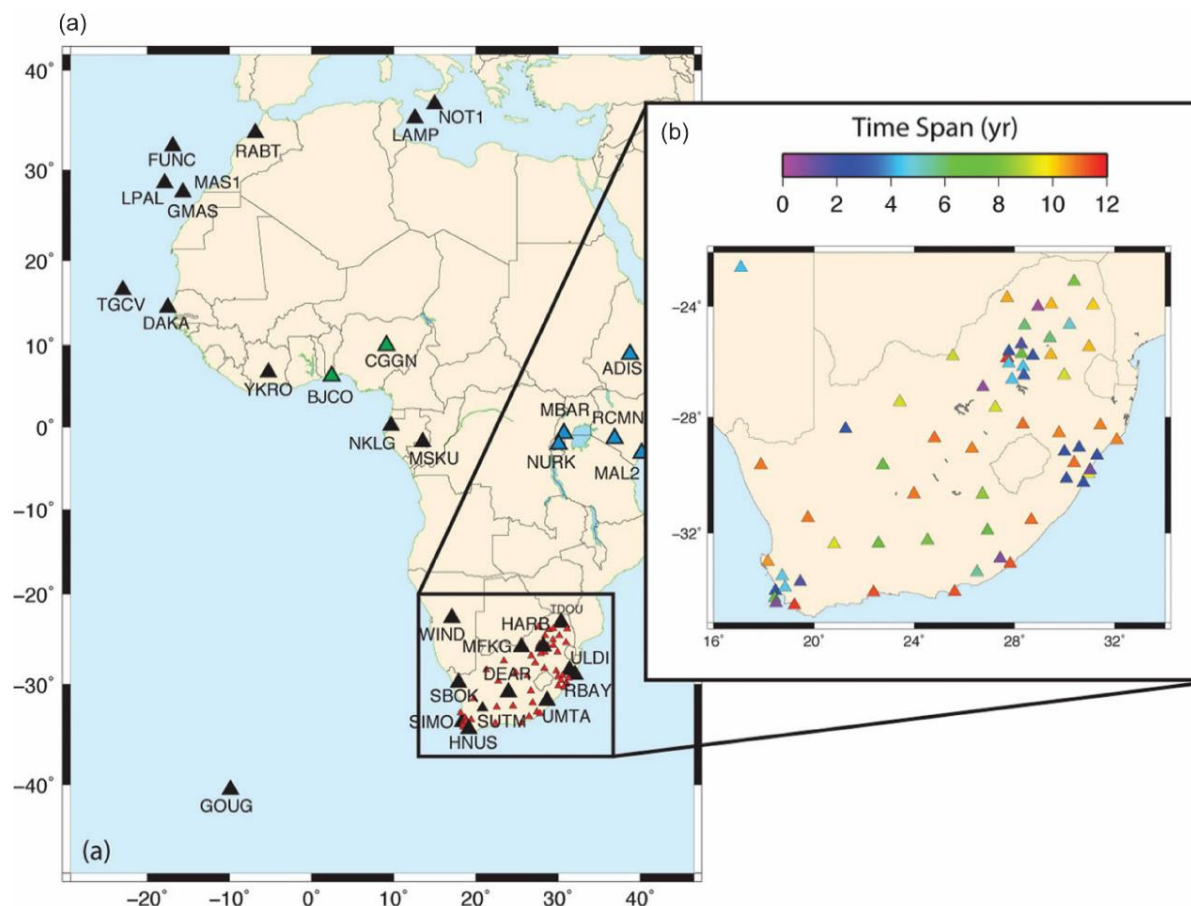

Figure 4-10. IGS and TrigNet stations used in the analysis provided in Malservisi et al. (2013), reprinted from Figure 2 of Malservisi et al. (2013). (a) The black triangles show IGS Nubia Plate sites, green triangles show sites with short time series, blue triangles show Somalia Plate or plate boundary sites, and red triangles show TrigNet sites. (b) Trignet sites colour coded by the time span of the data processed.

In September 2022, researchers from Cape Town and Universität München published a preliminary report (Abolghasem et al., 2022) using data from the GNSS study that intends to update the work from Malservisi et al. (2013). Their preliminary observations are: "*predominantly strike-slip strain rates at the 1-2 ns/yr level, typical of a stable continental region and consistent with the predominantly strike-slip earthquake focal mechanisms observed.*" They show relative velocities of the Western Cape in the 0.1-0.5 mm/yr range (see Figure 6 of their report). However, like Malservisi et al. (2013), these authors caution that a longer time series is needed to characterise the strain rates for the region and reduce noise. Given these conclusions and cautions, the SSM TI Team considered these data in their

development of the SSM, but only to the extent that they confirmed SSM TI Team's assessments of very low slip rates for the Groenhof Fault (Section 8.5.6) and the lack of observed slip and deformation on the regional-scale faults, including the Colenso Fault (Section 8.5.2).

4.2.11 Tectonic stress analysis

The SSM TI Team assessed the potential for fault slip based on an evaluation of tectonic stress data that was conducted within the DDC6 and 7 study on faults (Section 5.2.5) and a separate, independent specialty contractor study conducted by a research team at Southwest Research Institute (SwRI) in San Antonio Texas, in the USA. The goal of both studies was to define the tectonic stress tensor for the Western Cape based on earthquake hypocentre data and borehole breakouts and use that information to identify the most likely style of deformation (horizontal shear, extension, or compression) and the associated faulting regimes (strike-slip, normal, reverse). This leads to the most favourable orientations of fault surfaces that will fail under this tectonic stress.

The SSM TI Team considered several sources of information regarding the stress state of the Western Cape. These included the presentation at WS2 from Dr Andreoli and the references therein as well as published papers suggested to the SSM TI Team by the PPRP. These included Viola et al. (2005, 2012), Bird et al. (2006), White et al. (2009), Logue (2012), Hodge (2013), Paton (2022), Andreoli et al. (1996), and Andreoli (2012). In discussions with our specialty contractors at SwRI, the SSM TI Team decided that the earthquake focal mechanisms from the earthquake catalogue were the most reliable indicators of the stress state because they are the most direct representations of stress and the boreholes that were used by the specialty contractor were all in the Western Cape. The stress analysis performed by SwRI was based on these focal mechanisms. All other information regarding the stress state was considered by the SSM TI Team to be supporting information of the primary stress analysis. In a similar way, the borehole-breakout-based SHmax orientations from the World Stress Map database were not used directly by Smart et al. (2023) in their stress state determination. Rather, the borehole-breakout-based SHmax orientations were qualitatively compared to the 3DStress™-inversion-based maximum principal stress orientation (NW-SE trend) and shown to be generally compatible.

An intricate array of bedrock faults is mapped across the Western Cape. These faults were produced by the long and complex tectonic deformation of South Africa. This is especially evident in the syntaxis, which is characterised by two or three sets of fault orientations (Figure 4-11). However, not all these faults may be favourably oriented for future fault rupture given the present stress conditions. To assess which of the existing faults are most likely to reactivate, the SwRI team conducted a 3DStress analysis (McFarland et al., 2012; Morris et al., 2013) for the Western Cape region. The 3DStress code includes a patented stress inversion technique that can be used to estimate the stress states based on fault orientations and seismic moments, and then assess which faults are most likely to rupture (reactivate) in this stress state using the slip tendency analysis of Morris et al. (1996).

Fault displacement can be defined in terms of net slip measured paralleled to the fault plane, the horizontal component (heave), or as the vertical component of slip (throw). As an alternative, the fault area or earthquake magnitude can be scaled to slip using magnitude area or magnitude-displacements scaling relationship (Morris et al., 2016). The stress state

solutions are derived from inversion of earthquake events (strike, dip, seismic moment) that are within ~200 km of the Duynefontyn site. Slip tendency (T_S) is the ratio of shear stress (τ) to normal stress (σ_n) on a fault surface, as defined in equation 4-1 (Morris et al., 1996).

4-1

$$T_S = \tau / \sigma_n$$

For the 3DStress-based stress inversion analysis, SwRI staff used six earthquake focal mechanism solutions within approximately 200 km of the Duynefontyn site, including the selected nodal plane orientation and magnitude of each earthquake. To provide qualitative verification of the stress inversion results, SwRI staff considered maximum horizontal stress azimuth data from the World Stress Map database release in 2016 (Heidbach et al., 2016, 2018) that included both onshore earthquake-based orientations and offshore borehole-breakout-based orientations. This slip tendency analysis was used by the SSM TI Team to inform their assessment of seismogenic probability (p[S]) of active faults and to assign the range of fault orientations that were replicated in the virtual fault generator used to model faulting in the source zones nearest to the site, as described in Section 8.2.6.
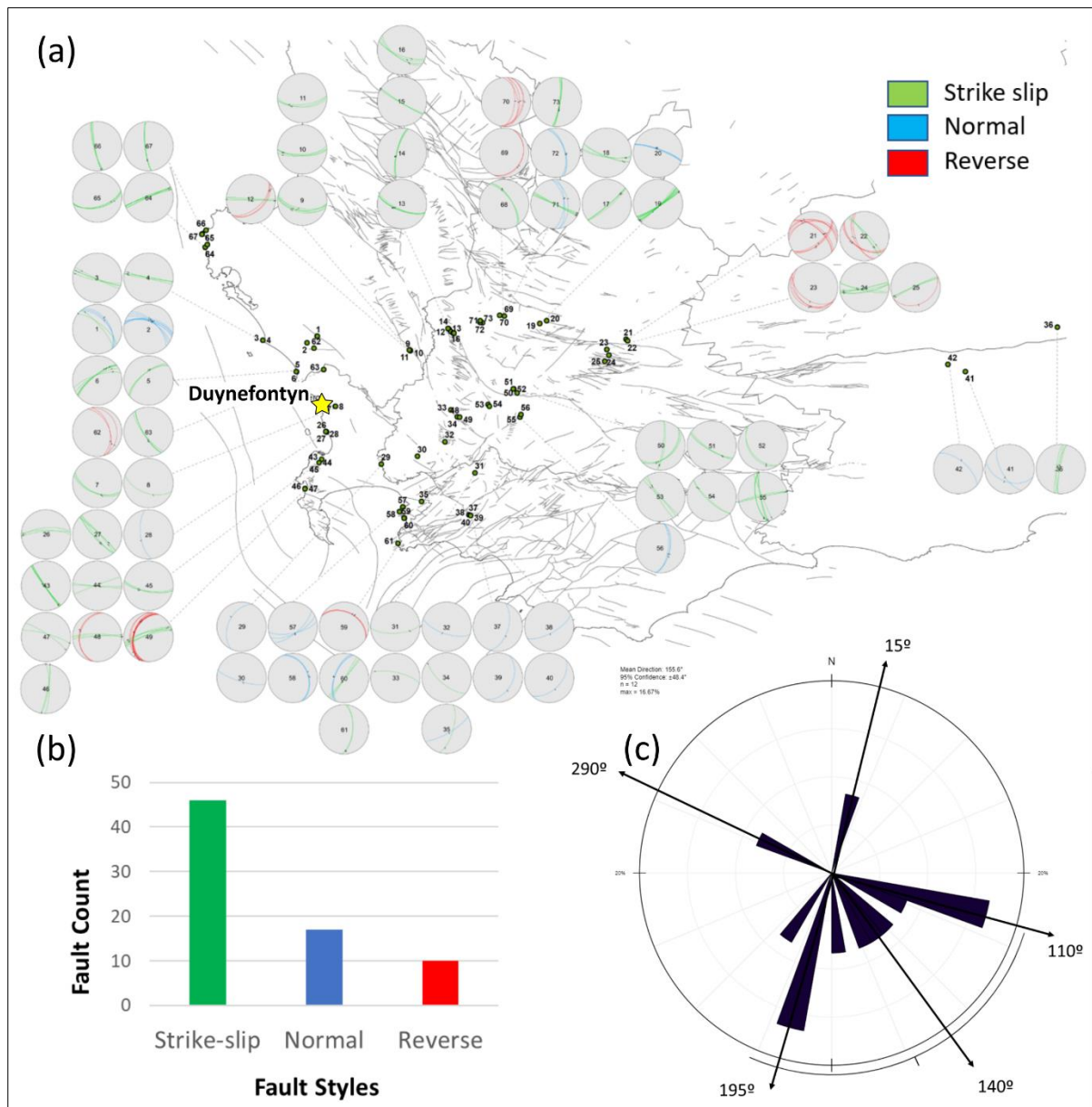
Figure 4-11. Mapped bedrock faults in the Western Cape compiled by CGS geologists and presented to the SSM TI Team at Workshop 1. In (a), stereonet plots show the style and orientation of each measure bedrock fault. The colour coding indicated the style of faulting, strike-slip (green), normal (blue), and reverse (red). (b) A histogram plot shows the number of each style of fault in (a). (c) A rose diagram showing the distribution of fault orientations in (a).

4.3   HISTORICAL SEISMICITY

The DDC4 report by Albini and Flint (2023) examined historical seismicity in the Western Cape region. It included characterisation of identified historical earthquakes and observations of the effects of these earthquakes that were obtained from various historical documents including newspapers and logs. They also went on to determine intensity data points (IDPs) using the compiled observations. There are 74 earthquakes evaluated in the report (Table 4-2), with an emphasis on the three largest earthquakes that occurred on 4 December 1809, 14 August 1857, and 29 September 1969.

Table 4-2. List of 74 reported events analysed and reported on by Albini and Flint (2023).

Year	Month	Day	Time local (SAST)	Area or Place Most Affected	Type	No. IDPs	Imax (MMI-56)	Newly Retr.
1620	Apr	7		Table Bay/ Robben Island	False		---	
1643	Apr	12		Cape Town, False Bay	False		---	
1690				Cape Town	Solitary	1	2–3	1 2
1693	Jun	3 to 5		Rockfall, Table Mountain	Confirmed		---	
1695	July			Rockfall, Table Mountain	False		---	
1695	Sep	4	18:00 to 19:00	Cape Town and neighbourhood	Solitary	1	4	
1696	Jan	11	14:00	Cape Town	Solitary	1	2–3	
1699	Oct	16		Rockfall, Table Mountain	Confirmed		---	
1739	Sep	5	2:00	Cape Town	Solitary	1	2–3	
1749	Aug	27	dawn	Cape Town	Solitary	1	2–3	
1760	May	27		Rockfall, Table Valley	Unverified		---	
1766	Jul	14	2:00	Cape Town	Solitary	1	3	
1801	Dec	8	10:00	Rockfall, Table Mountain	Confirmed		---	
1806	Jan	25	evening	Griquatown/ Griekwastad or Klaarwater	Solitary	1	3	
1809	Dec	4	22:10	"Cape Colony"	Multiple	13	7	
1810	Jan	23	3:45	Cape Town	Multiple	3	3	NR
1810	Jan	29	7:45	Cape Town	Multiple	3	3	
1810	Feb	5	1:00	Cape Town	Solitary	1	2–3	NR
1810	Apr	11	3:00	Cape Town	Solitary	1	3	
1810	Dec	12		Genadendal	False	---	---	
1810	Dec	26		Genadendal	Unverified	---	---	
1811	Jan	2		Cape Town	False	---	---	
1811	Jan	7	6:00	Cape Town	Solitary	1	3	
1811	Jun	2		Cape Town	False	---	---	

Year	Month	Day	Time local (SAST)	Area or Place Most Affected	Type	No. IDPs	Imax (MMI-56)	Newly Retr.
1811	Jun	10		Cape Town	False	---	---	
1811	Jun	7	12:00	Rietvlei	Multiple	4	6	
1811	Jun	19	10:00	Rietvlei	Multiple	4	6	
1813	Sep	12	2:00 to 3:00	Genadendal	Solitary	1	3	NR
1814	July	18	22:00	Mamre	Solitary	1	3	NR
1819	April	14	5:00	Leliefontein	False	---	---	
1819	Jun	24		Piketberg	Unverified	---	---	
1819	Jun/Jul	30	5:00	Leliefontein	Solitary	1	3-4	
1826				Saldanha Bay	Unverified	---	---	
1826	Apr	14	7:00	Cape Town	Solitary	1	3	
1830				Rockfall, Table Mountain	Confirmed	---	---	
1835	Nov	11	3:48	Cape Town	Multiple	4	3	
1842	Mar	22	16:00	Cape Town	Solitary	1	3	NR
1844	Jan	23	14:00 to 15:00	Cape Town	Solitary	1	3	NR
1852	Nov	12	9:00 to 10:00	Western Cape	Multiple	8	3	NR
1857	Aug	14	23:30	Western Cape	Multiple	38	5–6	
1862	Jun	23	2:00	Cape Town	Multiple	3	4	
1864	Feb	24	1:20	Knysna	Multiple	4	4	
1868	Oct	8	4:20	George	Multiple	3	4–5	(NR)
1869	Oct	31		Cape Town	False	--	--	
1869	Nov	23	19:50	Riethuis, NC	Multiple	3	4	
1874	Feb	26	2:30	Namaqualand, NC	Solitary	--	--	NR
1875	Oct	30	23:00 to 24:00	Rondebosch	Solitary	1	3	NR
1880	Jul	16	12:30	Darling	Multiple	6	4–5	NR
1882	Apr	28	1:15	Springbok, NC	Multiple	4	4	
1885	May	10	23:41	South-western Cape	Multiple	10	4	
1887	Mar	4	morning	Cape Town	Solitary	1	3	NR
1894	Dec	13	11:00	Darling	Multiple	2	3–4	NR
1899	Aug	9		The Towers, near Darling	Solitary	1	3	NR
1899	Sep	15	12:23	Cape Town	Multiple	19	5	
1901	Mar	24	16:42	Bishop's Court	Solitary	1	3	NR

Year	Month	Day	Time local (SAST)	Area or Place Most Affected	Type	No. IDPs	Imax (MMI-56)	Newly Retr.
1901	Apr	24		The Towers, Darling	Solitary	1	3	NR
1902	May	28		Cape Town	False	--	--	
1903	Jan	27	3:30	Tokai	Solitary	1	3	NR
1903	Jul	9		Cape Town	Multiple	7	3	
1903	Jul	10	3:00	Green Point	Solitary	1	3	NR
1909	Dec	9	16:22	Blaauwberg	Solitary	1		NR
1909	Dec	9	19:20	Worcester	Multiple	7	4	NR
1910	Feb	19	7:30	Montagu	Solitary	1	3	NR
1921	Oct	9	15:20	Tulbagh	Solitary	1	4	
1922	Jan	4	1:10	Tulbagh	Solitary	1	3	NR
1932	Nov	28	night	Moorreesburg	Solitary	1	3–4	NR
1940	Oct	11	23:40	Langebaan	Solitary	1	3–4	NR
1941	Oct	24	20:30	Van Rhynsdorp	Solitary	1	3–4	
1952	Feb	26	21:45	Swellendam	Solitary	1	3–4	NR
1960	Aug	29	7:35	Western Cape	Multiple	10	4	
1963	Aug	27	2:45 to 2:50	Western Cape	Multiple	39	4–5	
1963	Sep	17	1:40 to 6:00	Karoopoort	Solitary	1	3	
1969	Sep	11	23:45	Heidelberg	Multiple	19	5	
1969	Sep	29	22:05	Western Cape	Multiple	57	8–9	

Notes: IDP – Intensity Data Point; MMI-56 – Modified Mercalli Intensity scale; Newly Retr. (NR) – Indicates record was retrieved as part of DDC4.

The spatial distribution and quality of IDPs in any region is dependent on the spatial and temporal and spatial evolution of towns, cities, settlements, farms and population (especially for historical IDPs). It must be noted that earthquakes are usually limited in the geographical area over which shaking was experienced. This is clearly seen in the number and distribution of IDPs of events in the SW Cape Province as reported by Albini and Flint (2023). The growth of settlements in the province from Cape Town going inland with time is reflected by earthquakes felt mostly in the Cape Town in the Seventeenth Century with the number of earthquakes felt inland as immigrants moved further inland with time. A more detailed review of the temporal evolution of IDPs in the SW Cape Province was reported by Albini and Flint (2023).

Of the 74 events, Albini and Flint (2023) identified 14 to be false or unverified events. They were identified as fake events because they lacked any verifiable intensity observations. It appears original assessments had misinterpreted the observations as signs of an earthquake. Detailed information explaining how these events came to be reclassified as false events was given by Albini and Flint (2023). They also identified 25 newly recognized events that were not included in any previous catalogue. Thirty-three events had a single observation each resulting

in a single IDP for each event. Twenty-three events were each characterised by at least 2 IDPs. The 29 September 1969 earthquake at Ceres had 57 IDPs, the largest number of IDPs in the list. Albini and Flint (2023) did not extend their analysis to determine the location of the epicentre or estimate the moment magnitude of the events. However, in this study, an effort was made to determine the source parameters for those events with an adequate number of IDPs that also had a good spatial distribution.

The SSM TI Team made use of methods that are based on interpreting the spatial distribution and value of observed intensities to determine the epicentres and magnitudes of the events in Table 4-3. Usually, three levels of methods where macroseismic information is used to estimate earthquake source parameters are used. These methods differ according to the complexity and reliability of their application. They are classified under 1st, 2nd and 3rd generation techniques. Of these, the 3rd generation technique is used where a good spatial distribution and number of IDPs is available (Manzunzu et al., 2023). In this study the historical earthquakes assessment by the SSM TI Team was carried out using the 3rd generation methods that are included in the MEEP2 software (Musson, 2009). In the process, they utilize IDPs that are evenly distributed for location and magnitude determination (Musson, 2009). There are four methods that are implemented in the MEEP2 software (Musson, 2009; Musson and Jiménez, 2008). These methods include the Macroseismic Estimation of Earthquake Parameters (MEEP) by Musson (2009), the Bakun and Wentworth (1997) approach as initially described by Peruzza (1992), the Centroid method (BOXER) of Gasperini et al. (1999) and the Pairwise comparison of IDPs method presented by Vladimir Shumila at the ESC General Assembly in Athens, 1994, but was never published, According to Musson (2009) he was personnally informed by Shumila, that all the files linked to his method were lost. As a result, Musson (2009) reconstructed a simplified version of the method (Musson and Jiménez, 2008, Musson 2009).

The four methods use the individual IDPs to compute the epicentral location of the earthquake without computing the isoseismal lines. This is achieved through either the Centroid method (Gasperini et al., 1999) or the use of an empirical attenuation equation which assumes a function of distance that the IDPs follow and then applies a grid search to an area where each IDP must follow the attenuation equation (Kövesligethy, 1906; Bakun and Wentworth, 1997; Musson and Jiménez, 2008). Moment magnitude is determined according to a procedure prepared by Frankel (1994) and reported by Musson (2009) used for comparison purposes relative to the other historical events. For the project catalogues, the SSM TI team derived independent estimates of magnitude for all catalogue entries. The methodology of those independent estimates is described in Section 6.6.

The major advantage of the four techniques implemented in the MEEP2 software is that they use individual IDPs directly to compute the source parameters instead of converting them into isoseismals first. This has the advantage of removing outliers and wrong IDPs to constrain the final solution. These methods are computationally different, and they generally yield comparable results (e.g., Strasser et al., 2015; Albini et al., 2014) especially with well distributed IDPs. The SSM TI Team analysed the historical earthquakes with sufficient spatial coverage and number of IDPs using the MEEP2 software. Most of the analysis involved carefully summarising the observed IDPs and then using them to determine the earthquake source parameters (e.g., epicentre and magnitude). This was mainly done for those events without instrument solutions.

For each event, the epicentres and magnitudes obtained from each of the different methods were combined by the SSM TI Team to obtain the best estimate values using assigned event specific weights for each method. The weighing scheme that is provided in each of the TI Team's analysis for each earthquake was based on individual epicentre and magnitude error values for each method. The method that produced a solution with the lowest error was given the highest weight by the SSM TI Team. It should be noted that this process results in the weights assigned to each method fluctuating considerably from one earthquake to another.

Linking the assignment of weights to the errors of the locations reduces the subjectivity that is normally associated with such an exercise. The combined solution obtained using this method is selected as the preferred solution for each event except where instrumental solutions are available. Also included in Table 4-5 to Table 4-14 the published solution for each event as reflected in the CGS database (i.e. written as CGS Solution in tables). A bootstrap resampling routine was employed by the SSM TI Team to compute an uncertainty on all parameters. This involved repeating the calculations for source parameters 1,000 times using random resamples. From the 1,000 estimates of each parameter, a standard deviation is calculated from which root-mean-square (RMS) values are determined and are referred to here as the error. The error values vary for each earthquake depending on the number and distribution of the IDPs. The actual values of the weights assigned are different for each event but are consistent in that high values are assigned for solutions with low errors.

Table 4-3. Historical earthquakes assessed by the SSM TI Team using the MEEP2 software.

No.	Earthquake	Number of IDPs
1	04 December 1809	13
2	14 August 1857	38
3	10 May 1885	10
4	15 September 1899	19
5	9 July 1903	7
6	9 December 1909	8
7	29 August 1960	10
8	27 August 1963	39
9	11 September 1969	19
10	29 September 1969	57

Solutions determined using these methods by the SSM TI Team depend on the spatial distribution of IDPs. Generally, IDPs with the highest intensity values are modelled first and the rest are added in descending order. In this regard, the reliability of the final solution depends on the distribution of intensities of different values. For example, an earthquake with 10 IDPs where three have intensity of VI, five intensity values of V, and two with intensity values of IV, will yield reliable estimates of source parameters compared to another event with 10 IDPs all with intensity values of IV. This is because the basic assumption is that the

epicentral location is close to the IDP with the highest intensity (Musson, 2009). Different intensity values will generally show attenuation from high intensities closer to the epicentral areas to low intensities farther away.

4.3.1   The 4 December 1809 earthquake

In their study of this earthquake, Albini and Flint (2023) focused on retrieving as many contemporary and independent first-hand sources as possible to determine the maximum number of IDPs for the event. Thirty-three observations were obtained and used to determine the 12 IDPs shown in Figure 4-12. Albini and Flint (2023) also obtained observations of liquefaction (Table 4-4) that were linked to the earthquake.

There were reliable reports of many aftershocks of this event in the region. However, the SSM TI Team was not able to find any reliable locations of the main event and its aftershocks apart from the general region of the Cape Colony. Albini and Flint (2023) also did not give an estimate for the location of the event.

However, an existing location was given by Brandt et al. (2005). It was relocated to near Cape Town based on reports by Von Buchonroder (1830) of fissures at Jan Biesjes Kraal and sand boils near Blaauwberg's Valley (near present day Milnerton) Using the program MEEP2 (Musson, 2009; Musson and Jimenez, 2008), the SSM TI Team estimated an alternative location using the spatial distribution of the IDP that were estimated for this event. The solutions obtained are shown in Table 4-5 and Figure 4-13. The Bakun and Wentworth solution had a large location error value and thus it was not used in the calculation of the combined solution as shown by the assigned weight of zero (Table 4-5).
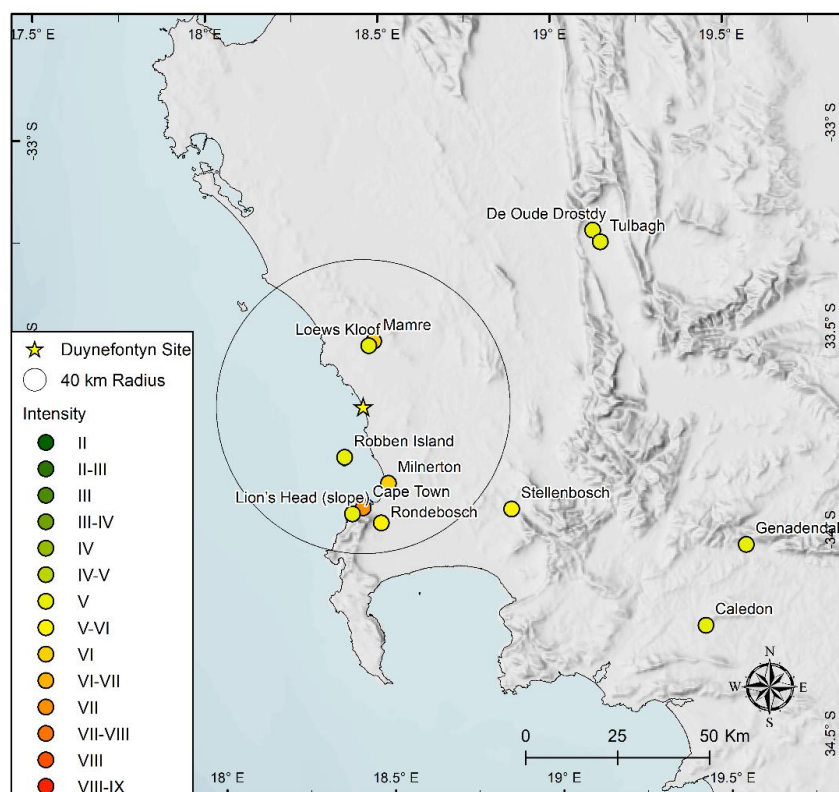

Figure 4-12. Distribution of Intensity Data Points in the Modified Mercalli Intensity (MMI-56) scale (Richter, 1958) for the 4 December 1809 earthquake.

Table 4-4. Liquefaction effects observed during and after the 4 December 1809 earthquake.

Observed at	Kuester, 1809 Dec 5 Kuester and Kuehnel, 1809 Dec 5	von Buchenroder, 1809 Dec 9
On the road between Mamre (Gruenekloof) and Cape Town Blauweberg's Valley Blaauwberg	On the 5th [Dec], we left Gruenekloof [Mamre] for Cape Town. On the road we saw many singular appearances, occasioned by the earthquake. In some places there were chasms in the ground, into which we could put our hands. In others, fountains had burst forth, where formerly no water had been found and they also threw up quantities of white sand.	At Blauweberg's Valley, I found the sandy surface studded with innumerable holes, resembling in shape, but in nothing else, craters in miniature. These holes were from six inches to a foot and a half, and some even three feet in diameter, and from four inches to a foot and a half deep; of a circular form, and the sides sloping to the centre. They were lined with a crust of bluish clay, of about a quarter of an inch in thickness, which had been baked by the sun, and according to its nature had cracked and curled up in fragments, which however adhered still to the sloping sides of the holes. I reckoned seven of these holes, of different dimensions, in an area, contained within a circle, which I drew around me with a walking stick, and which might have been somewhat more than ten feet in diameter. The people at Blauweberg's Valley, stated, that "they saw jets of coloured water spout from these holes to the height of six feet, in the night of the 4th of December, at the time that the shocks were felt"
Jan Biesjes (Beesjes) Kraal Milnerton	On the following day [5 Dec], towards evening, we set off in company with Brother Schmitt and his wife, for Cape Town. On the road we beheld with surprize [*sic*] the effects of the earthquake at a farm, where no less than twelve fountains had burst forth, and brought up water, and a quantity of white sand from a great depth. The nearer we approached to the Cape, the more accounts we heard of the mischief done.	Near the Kraal I found rents and fissures in the ground, one of which I followed for about the extent of a mile. In some places they were more than an inch wide, and in others much less. In many places I was able to push into them, in a perpendicular direction, a switch to its full length, of three or four feet. By the people residing in the vicinity, I was informed, that they had observed these fissures on the morning of 5th December, in some instances three and four inches wide, and that one person had been able to push the whole length of an iron rod used to fix curtains upon into them, and that others had been able to do the same with whip-handles of even ten feet in length.

Table 4-5. The 1809 earthquake locations using the MEEP2 software.

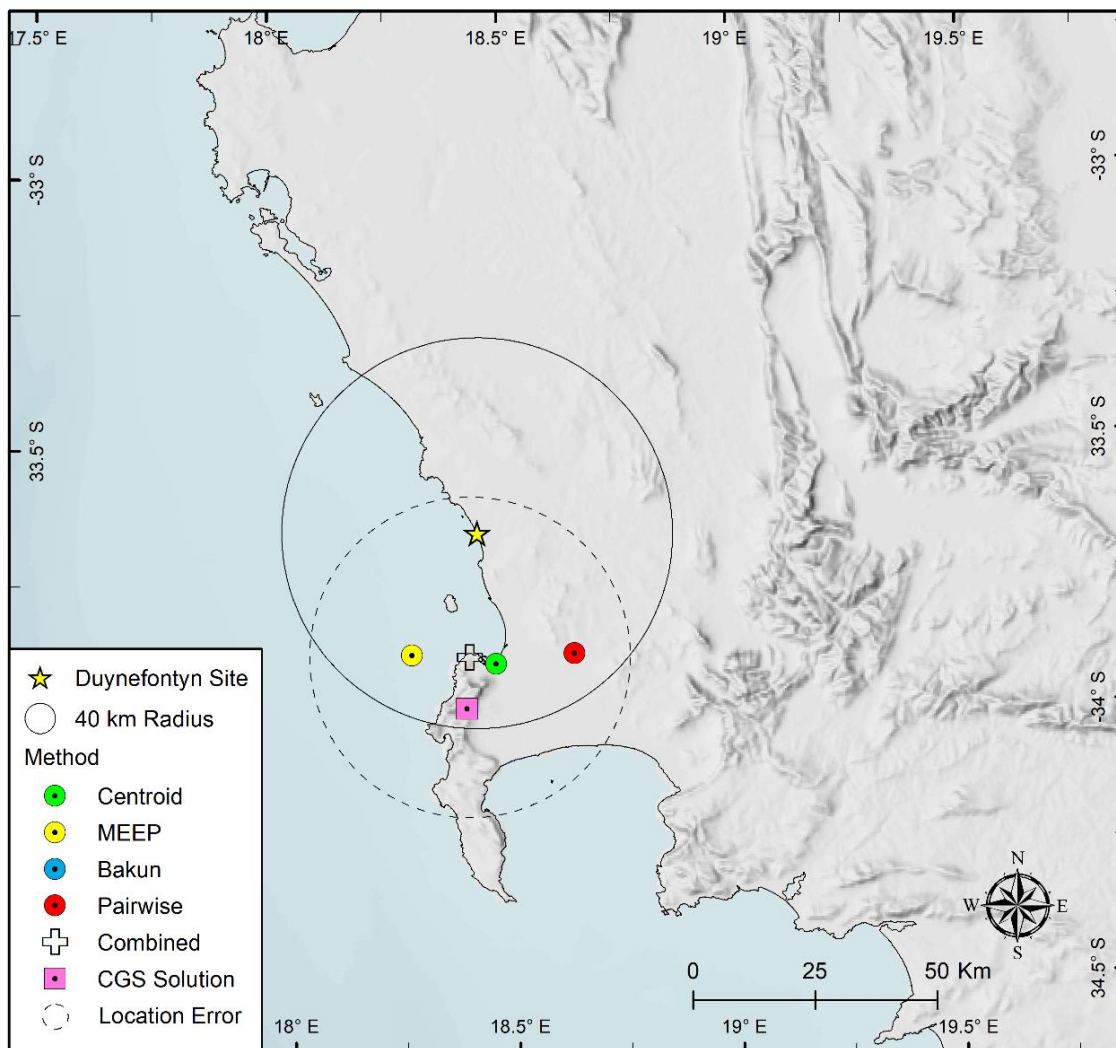| Method	Latitude	Longitude	Location error (± km)	Magnitude, M	Magnitude error, (±)	Depth (km)	Weight of solutions
Centroid	-33.918	18.467	30.9	5.2	0.3	20	0.3
MEEP	-33.899	18.281	26.5	5.5	0.4	20	0.5
Bakun and Wentworth	-35.020	17.586	195.7	6.8	1.1	-	0.0
Pairwise	-33.902	18.641	51.6	5.2	0.3	-	0.2
Combined	**-33.906**	**18.409**	**32.84**	5.3	**0.33**	**20**	**1**
CGS Solution	**-34.0**	**18.400**		6.3			

Figure 4-13. Location of epicentral solutions obtained for the 1809 earthquake using intensity data (Figure 4-12) and the MEEP2 software.

4.3.2 The 14 August 1857 earthquake

This event was well recorded with 72 observations used to determine or prepare 38 IDPs (Figure 4-14). However, Albini and Flint (2023) did not give an estimate of the event location and magnitude. The current location of the event is based on intensity data as reported by Brandt et al. (2005) and shown in Table 4-6. Using the program MEEP2 (Musson, 2009; Musson and Jimenez, 2008), the SSM TI Team estimated an alternative location using the spatial distribution of the IDPs that were newly estimated for this event. The obtained solutions are shown in Table 4-6 and Figure 4-15.
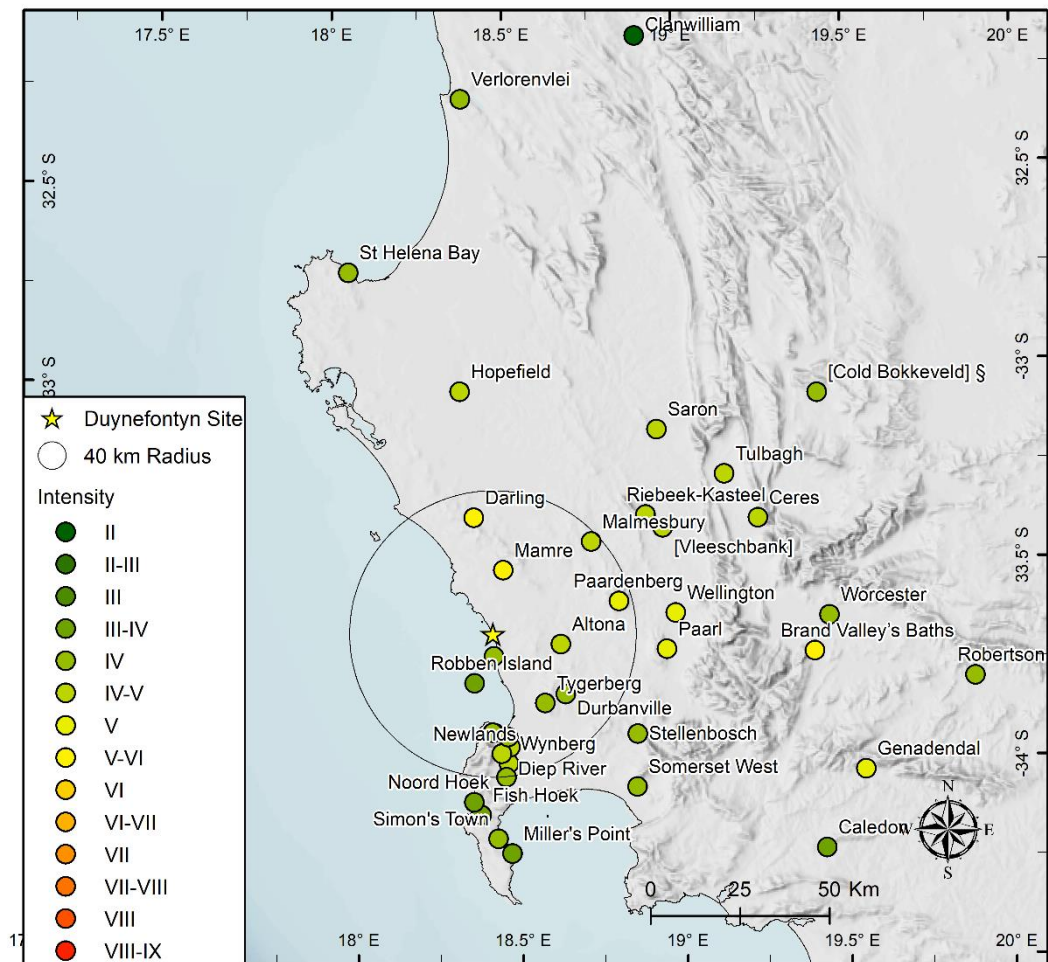
Figure 4-14. Distribution of Intensity Data Points in MMI-56 scale for the earthquake of 14 August 1857.

Table 4-6. The epicentre solutions for the 14 August 1857 earthquake using the MEEP2 software.

| Method	Latitude	Longitude	Location error (± km)	Magnitude, M	Magnitude error, (±)	Depth (km)	Weight of solutions
Centroid	-33.643	18.923	22.4	4.1	0.0	20.0	0.4
MEEP	-33.532	18.691	29.5	4.1	0.0	20.0	0.3
Bakun and Wentworth	-33.281	18.534	83.3	4.8	0.3		0.1
Pairwise	-33.316	18.732	55.1	4.1	0.2		0.2
Combined	**-33.508**	**18.776**	**37.2**	4.17	0.1	**20.0**	**1.0**
CGS Solution	-33.500	19.000		5.0			
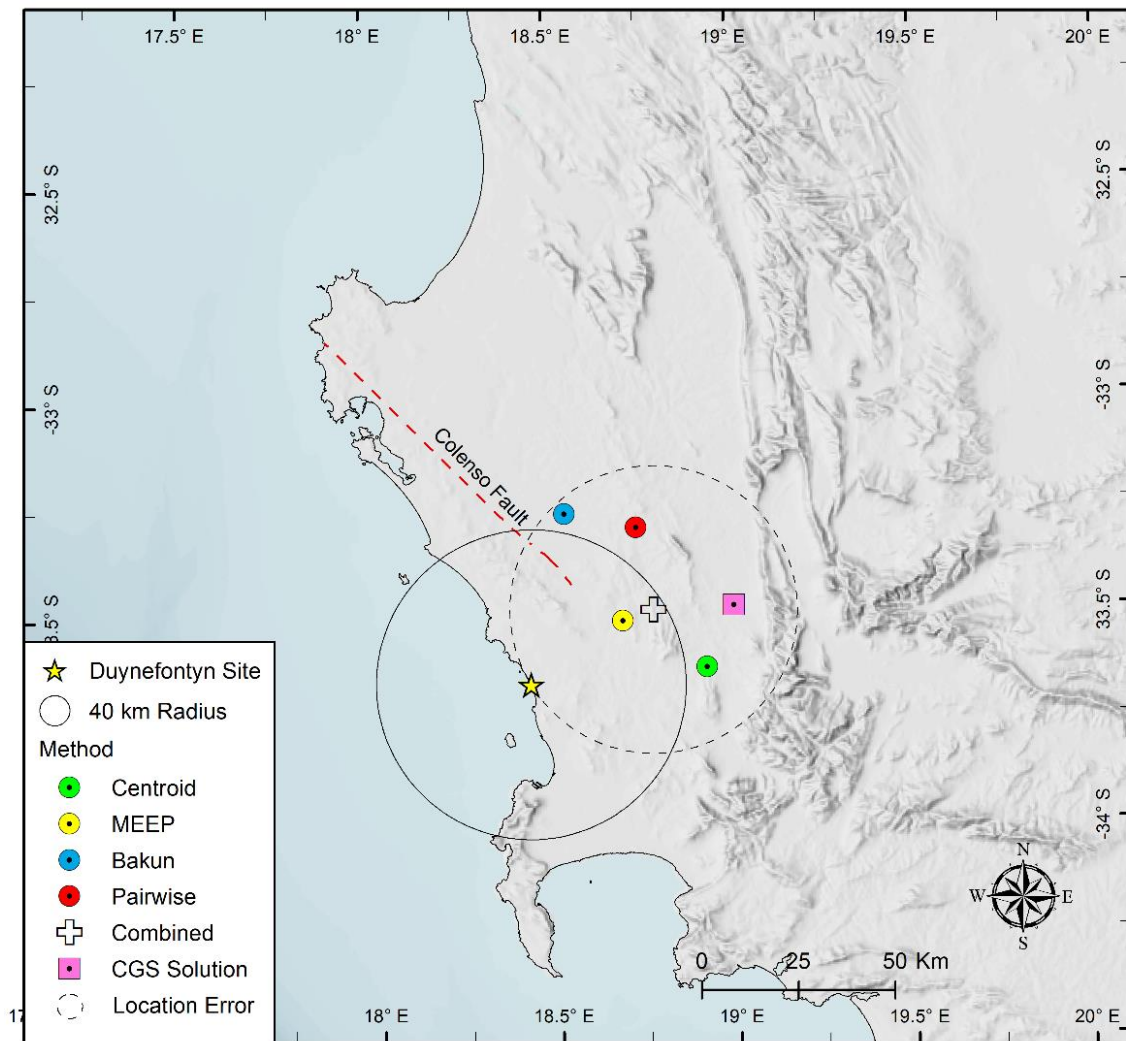
Figure 4-15. Location of epicentral solutions obtained for the 14 August 1857 earthquake using intensity data (Figure 4-14) and the MEEP2 software.

4.3.3   The 10 May 1885 earthquake

Using 14 observations, Albini and Flint (2023) created ten IDPs which showed that the event was mostly felt in the Western Cape Province close to Cape Town (Figure 4-16). The source solutions obtained for this event using the four methods in the MEEP2 software package are all generally in good agreement. To obtain the best and preferred location of the event, the four solutions were combined by the SSM TI Team according to the weight values shown in Table 4-7. The epicentral error of the obtained solution had a radius of 19 km, while the magnitude error was 0.2. The obtained solutions are shown in Table 4-7 and Figure 4-17.
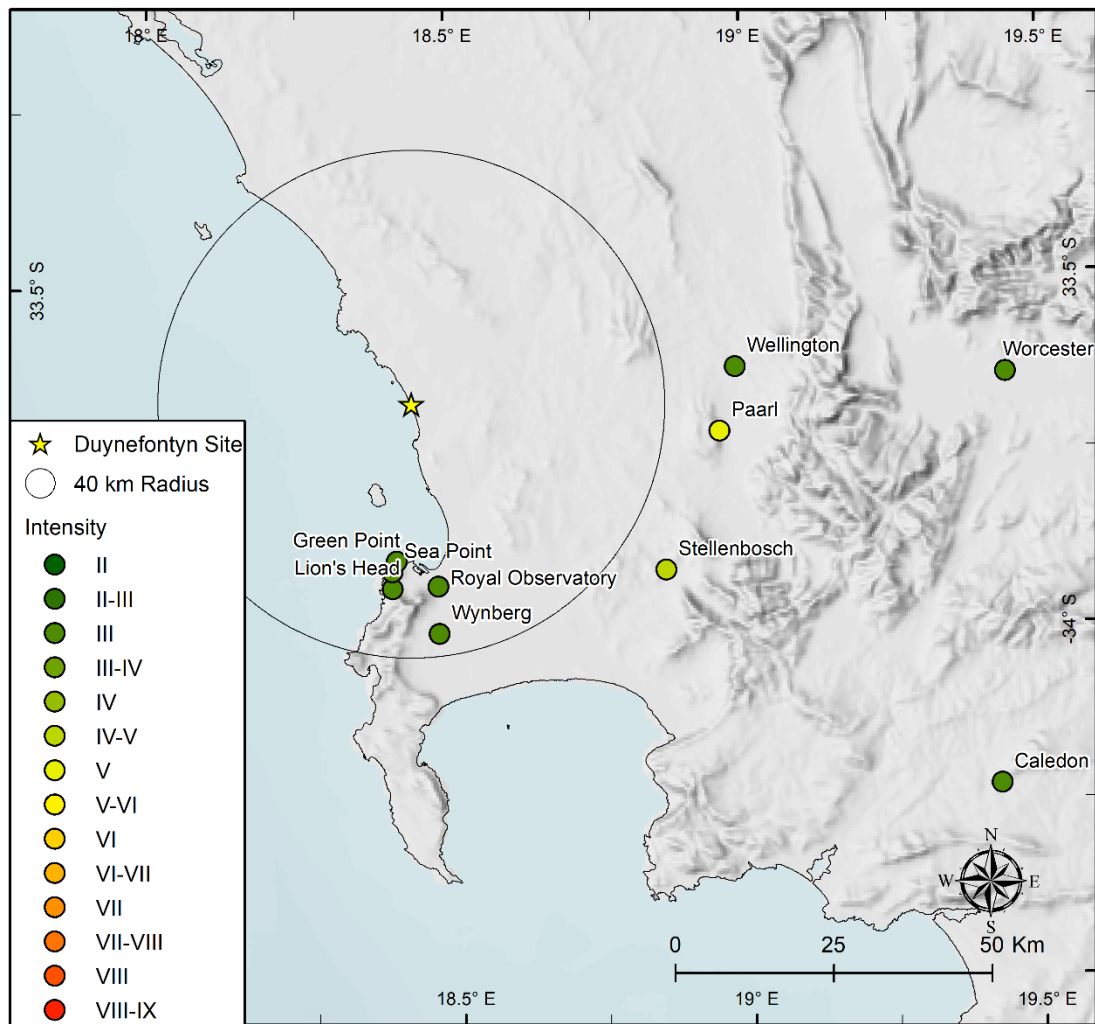
Figure 4-16. Distribution of Intensity Data Points in MMI-56 scale for the 10 May 1885 earthquake.

Table 4-7. The epicentre solutions for the 10 May 1885 earthquake using the MEEP2 software.

| Method	Latitude	Long-itude	Location Error (± km)	Magnitude M	Magnitude Error	Depth (km)	Depth Error (± km)	Weight of Solutions
Centroid	-33.872	18.615	14.6	3.7	0.2	20.0	7.0	0.3
MEEP	-33.785	18.941	9.3	3.4	0.1	10.0	4.0	0.3
Bakun and Wentworth	-33.854	18.983	21.8	3.4	0.2			0.2
Pairwise	-33.932	18.74	40.7	3.6	0.2			0.2
Combined	**-33.8543**	**18.811**	**19.7**	**3.5**	0.2	14.0	**5.2**	**1.0**
CGS Solution	-33.900	18.400		3.3				
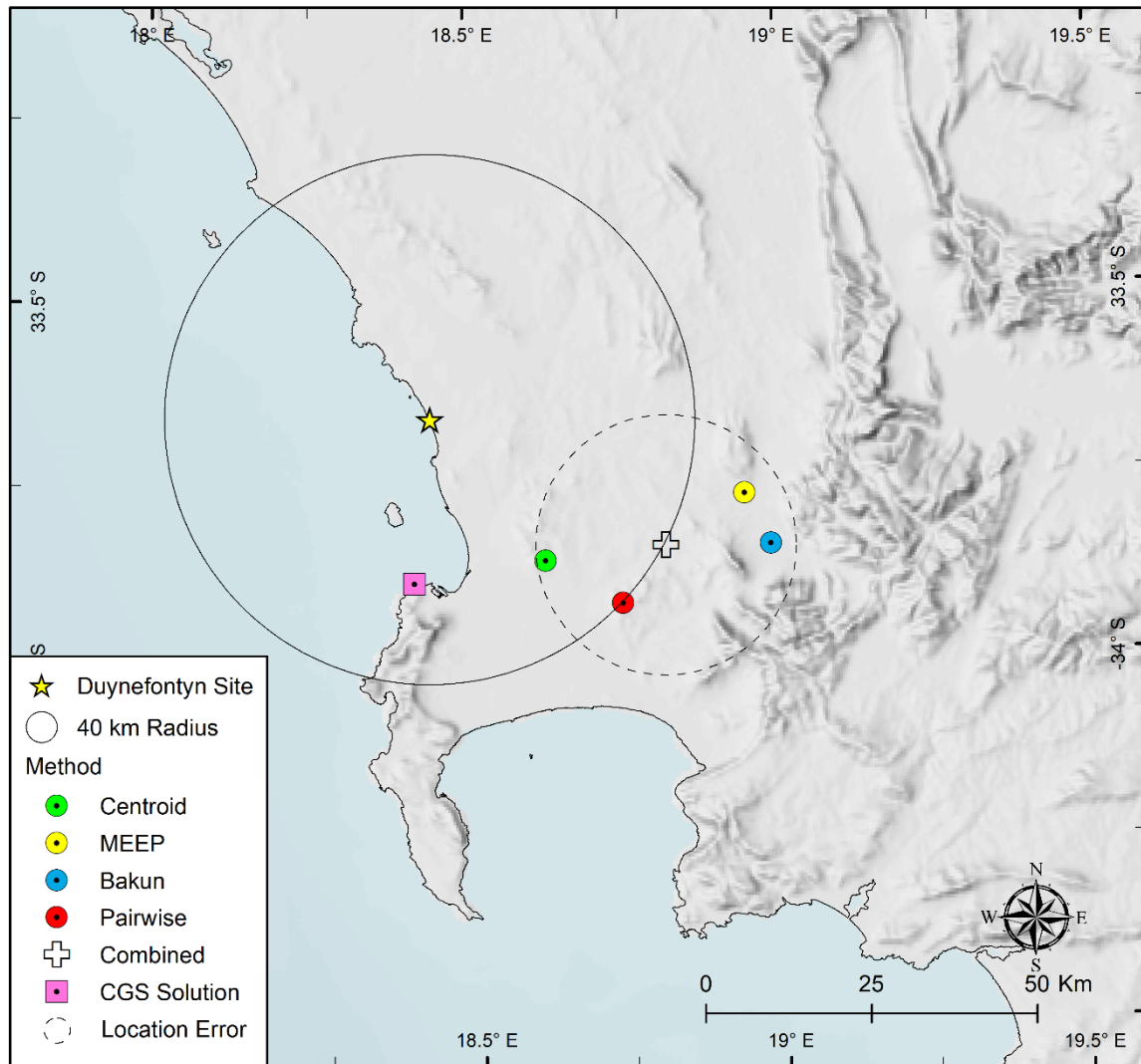
Figure 4-17. Location of epicentral solutions obtained for the 10 May 1885 earthquake using intensity data (Figure 4-16) and the MEEP2 software.

4.3.4 The 15 September 1899 earthquake

Using observation data from newspapers and brief reports from the Meteorological Commission, 19 IDPs were created for this event (Figure 4-18). Using the obtained IDPs and the software MEEP2, the SSM TI Team obtained source parameters for the event (Figure 4-19).
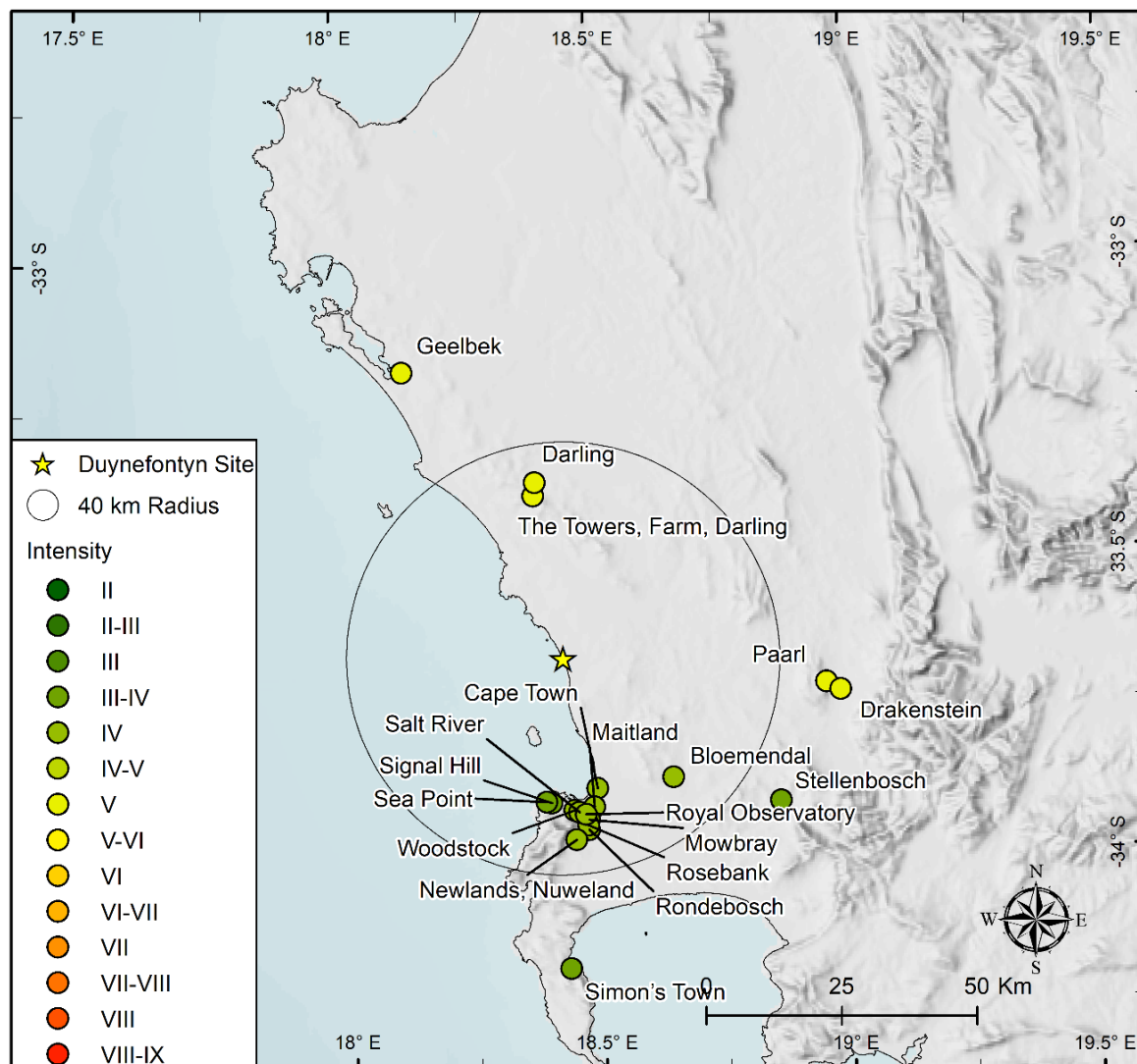
Figure 4-18. Distribution of Intensity Data Points in MMI-56 scale for the 15 September 1899 earthquake.

Though the locations obtained are not too far from each other, the epicentral error for the Bakun and Wentworth solution is quite large at 195 km, especially when compared to values obtained for the other solutions (Table 4-8). Therefore, only the three solutions obtained using the Centroid, MEEP and Pairwise techniques were combined to obtain the combined solution, which was taken as the preferred solution for this event. The SSM TI Team determined a magnitude of **M** = 5.3 with an error of 0.3. The obtained solutions are shown in Table 4-8 and Figure 4-19.

Table 4-8. The epicentre solutions for the 15 September 1899 earthquake using the MEEP2 software.

| Method	Latitude	Longitude	Location error (± km)	Magnitude, M	Magnitude error, (±)	Depth (km)	Weight of solutions
Centroid	-33.918	18.467	30.90	5.2	0.3	20.0	0.30
MEEP	-33.899	18.281	26.50	5.5	0.4	20.0	0.50
Bakun and Wentworth	-35.020	17.586	195.70	6.8	1.1		0.00
Pairwise	-33.902	18.641	51.60	5.2	0.3		0.20
Combined	**-33.905**	**18.409**	**32.84**	5.29	0.33	**20.0**	**1**
CGS Solution	-34.000	18.400		6.3			
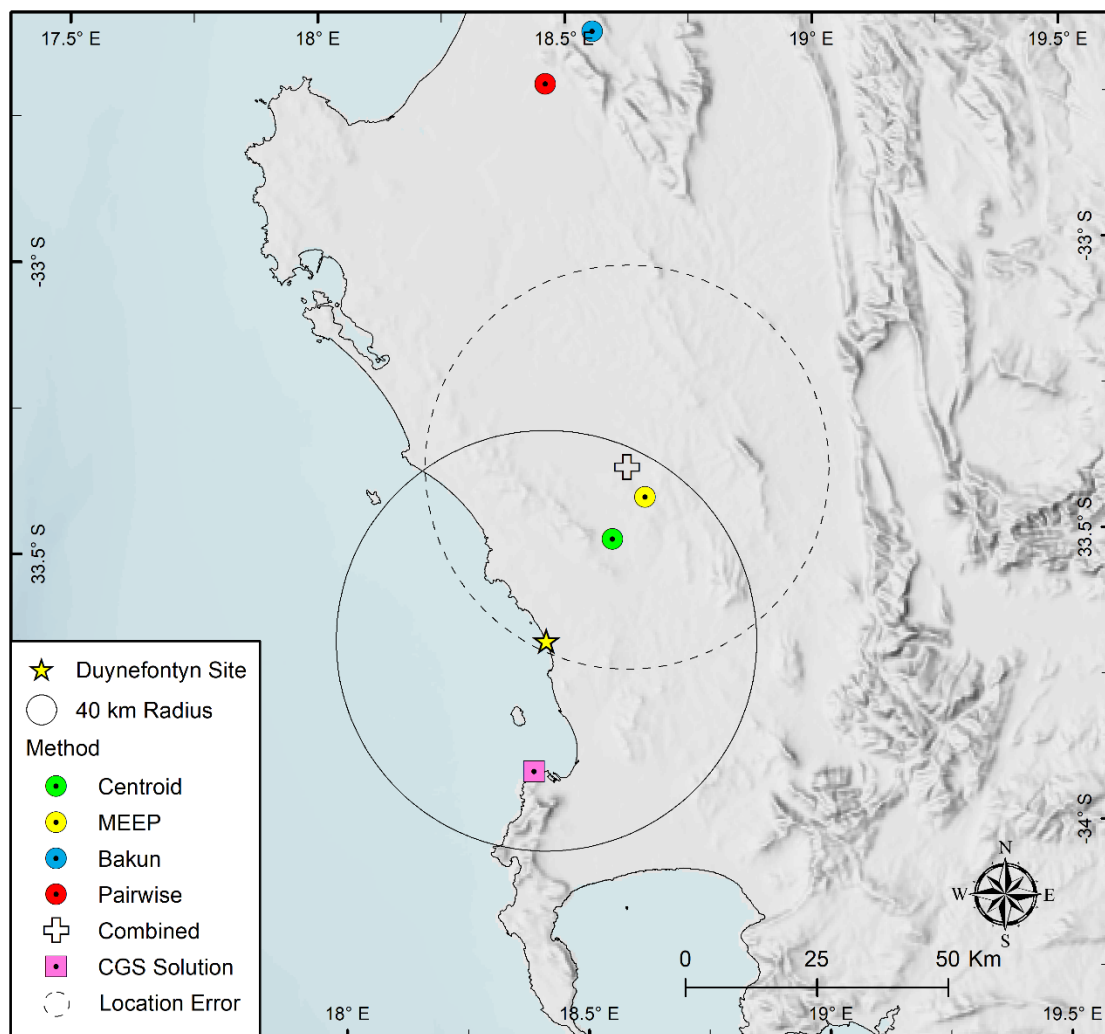
Figure 4-19. Location of epicentral solutions obtained for the 15 September 1899 earthquake using intensity data (Figure 4-18) and the MEEP2 software.

4.3.5   The 9 July 1903 earthquake

Using multiple observations, Albini and Flint (2023) created seven IDPs for the 9 July 1903 earthquake (Figure 4-20). However, all the created IDPs had the same intensity value of III. Normally such a distribution will not yield a reliable estimate of the source parameters (Manzunzu et al., 2023). However, an effort was still made to determine the source parameters (Figure 4-21, Table 4-9) for this event with the compiled IDPs. The preferred solution was obtained by combining the solutions obtained using the Centroid, MEEP and Pairwise methods. The solution obtained using the Bakun method had a large error of 279 km, which was much larger than the other three methods and the Bakun epicentre was located more than 150 km to the east (Figure 4-21). Thus, the SSM TI Team decided not to use the Bakun solution in determining the final solution.
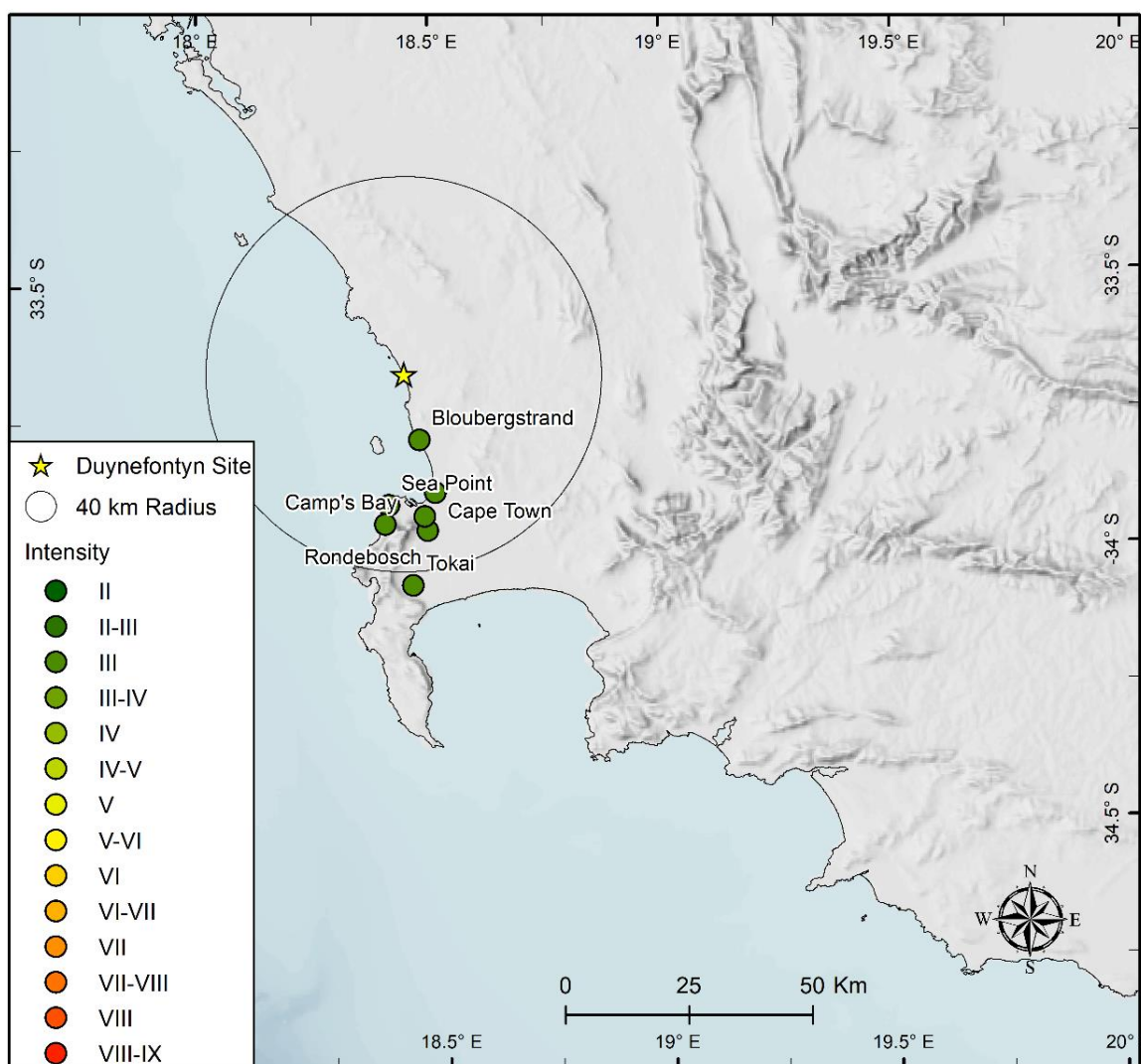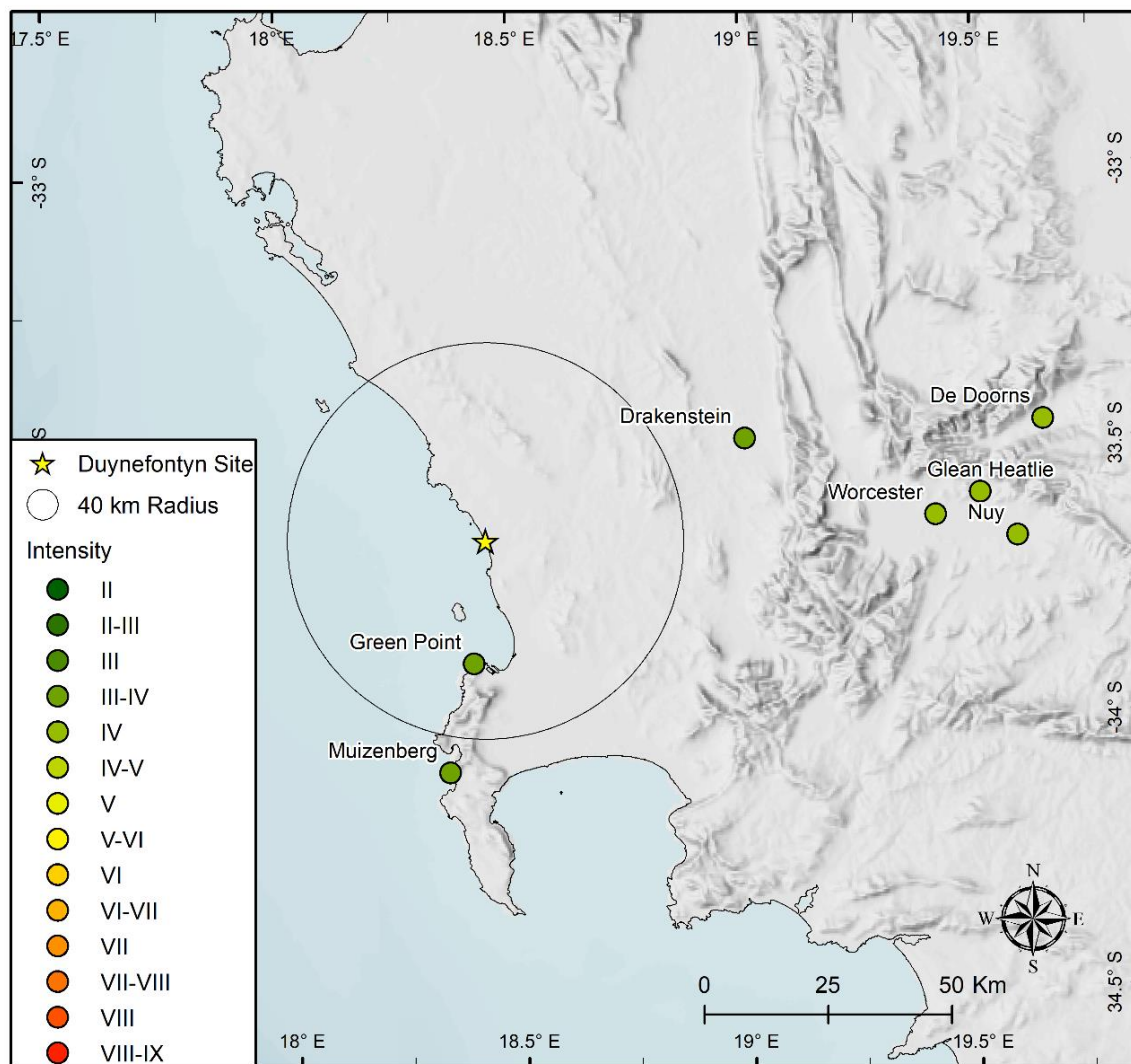

Figure 4-20. Distribution of IDPs in MMI-56 scale for the 9 July 1903 earthquake.

Table 4-9. The epicentre solutions for the 9 July 1903 earthquake using the MEEP2 software.

| Method	Latitude	Longitude	Location error (± km)	Magnitude, M	Magnitude error, (±)	Depth (km)	Weight of solutions
Centroid	-33.932	18.443	3.7	3.0	0.0	10.0	0.4
MEEP	-33.923	18.674	26.9	3.0	0.0	10.0	0.2
Bakun and Wentworth	-34.003	19.954	279.4	4.6	0.1		0
Pairwise	-33.932	18.443	3.7	3.0	0.0		0.4
Combined	**-33.9302**	**18.489**	**8.34**	3.2	0.01	**10.0**	**1**
CGS Solution	-33.900	18.400		3.7			
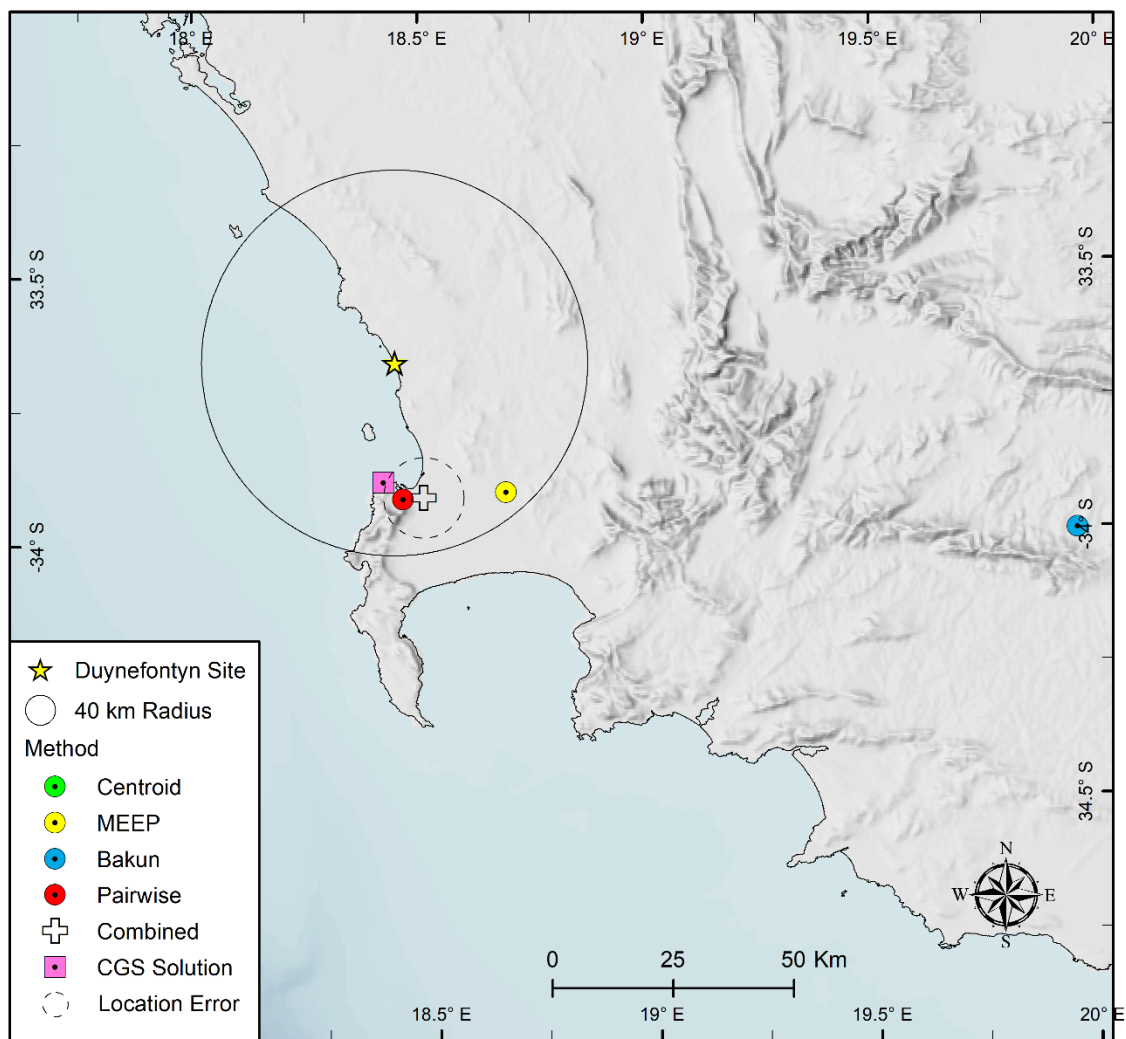
Figure 4-21. Location of epicentral solutions obtained for the 9 July 1903 earthquake using intensity data (Figure 4-20) and the MEEP2 software.

4.3.6 The 9 December 1909 earthquake

Seven IDPs were created by Albini and Flint (2023) using the observations obtained from newspapers and an Agricultural Journal (1909). The IDPs were located in the Western Cape close to Cape Town (Figure 4-22). The epicentre for this event (Figure 4-23) was estimated by the SSM TI Team using the obtained IDPs and the MEEP2 software. As observed with solutions obtained for other events, the Bakun solution had a large epicentral error of about 120 km (Table 4-10) and thus, it was not used by the SSM TI Team in determining the final preferred (combined) solution for this event.

Figure 4-22. Distribution of IDPs in MMI-56 scale for the 9 December 1909 earthquake.

Table 4-10. The epicentre solutions for the 9 December 1909 earthquake using the MEEP2 software.

| Method	Latitude	Longitude	Location error (± km)	Magnitude, M	Magnitude error, (±)	Depth (km)	Weight of solutions
Centroid	-33.644	19.551	15.2	3.9	0.2	20.0	0.4
MEEP	-33.713	19.234	16.6	3.8	0.1	20.0	0.4
Bakun and Wentworth	-34.534	20.042	120.5	5.2	0.2		0
Pairwise	-33.593	19.977	38.7	4.2	0.2		0.2
Combined	**-33.6614**	**19.5094**	**20.46**	3.9	0.17	**20.0**	**1**
CGS Solution	-33.900	18.400		3.7			
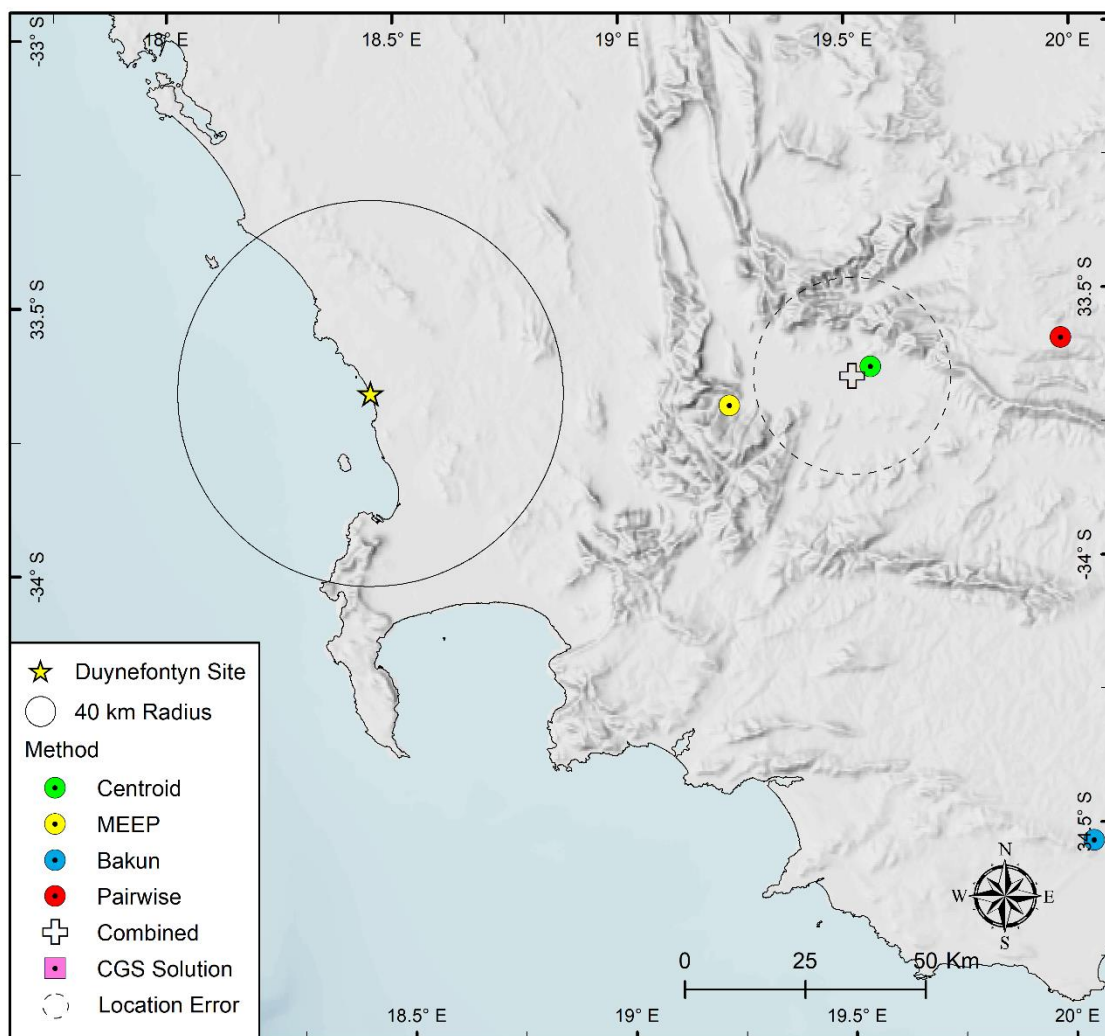
Figure 4-23. Location of epicentral solutions obtained for the 9 December 1909 earthquake using intensity data (Figure 4-22) and the MEEP2 software.

4.3.7 The 29 August 1960 earthquake

The records related to the 29 August 1960 earthquake were obtained by Albini and Flint (2023) from three newspapers that were published in Cape Town at the time. Using these records, Albini and Flint (2023) created ten IDPs located along the south-western coast of the Western Cape Province (Figure 4-24). Using the compiled IDPs and the MEEP2 software, source parameters were obtained by the SSM TI Team for this event using the four techniques that are part of the software. However, only two of the solutions (Centroid and MEEP solutions) were combined to produce the preferred solution (white star in Figure 4-25) because the Bakun and Pairwise solutions had large epicentral error values (Table 4-11) and had suspect locations that were far from the other two (MEEP and Centroid). Thus, these two solutions were not used by the SSM TI Team to determine the combined preferred solution.
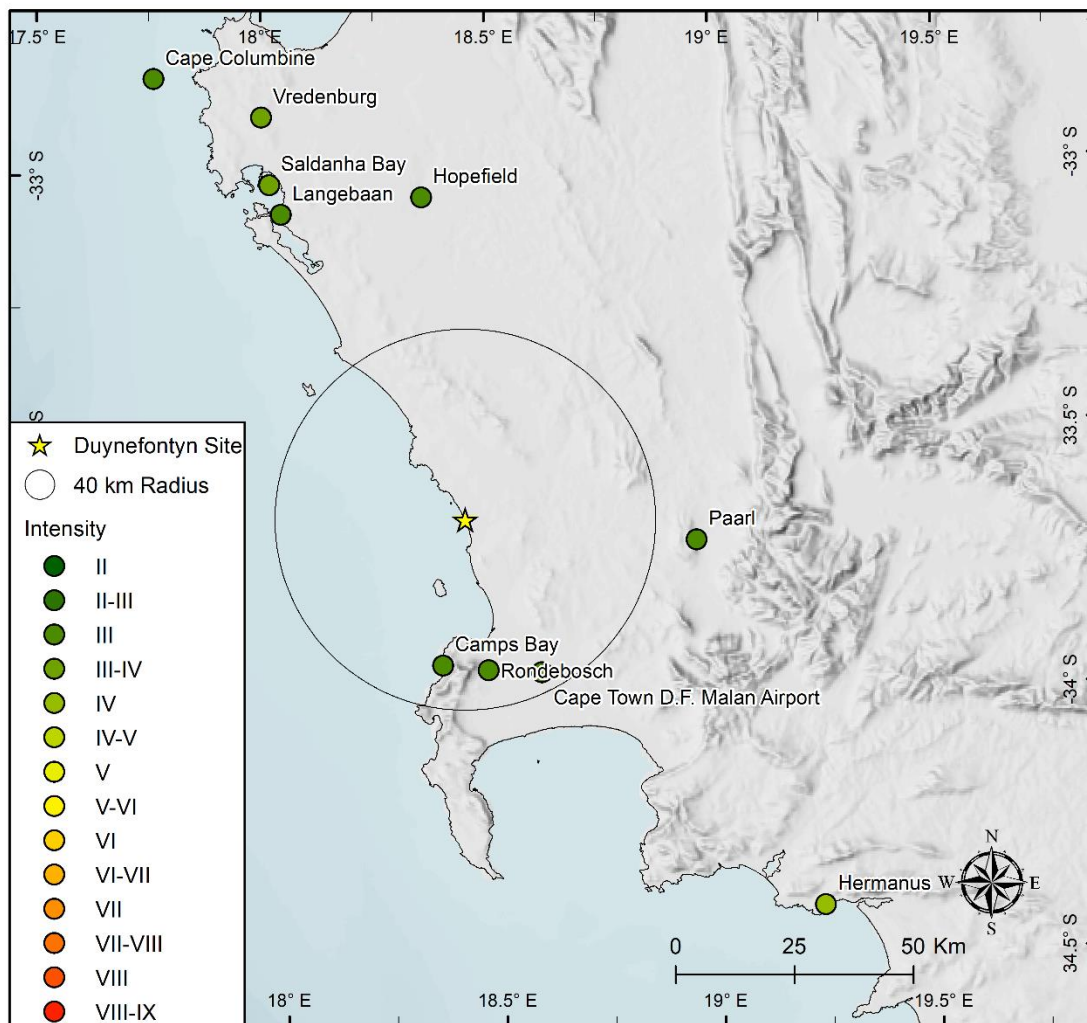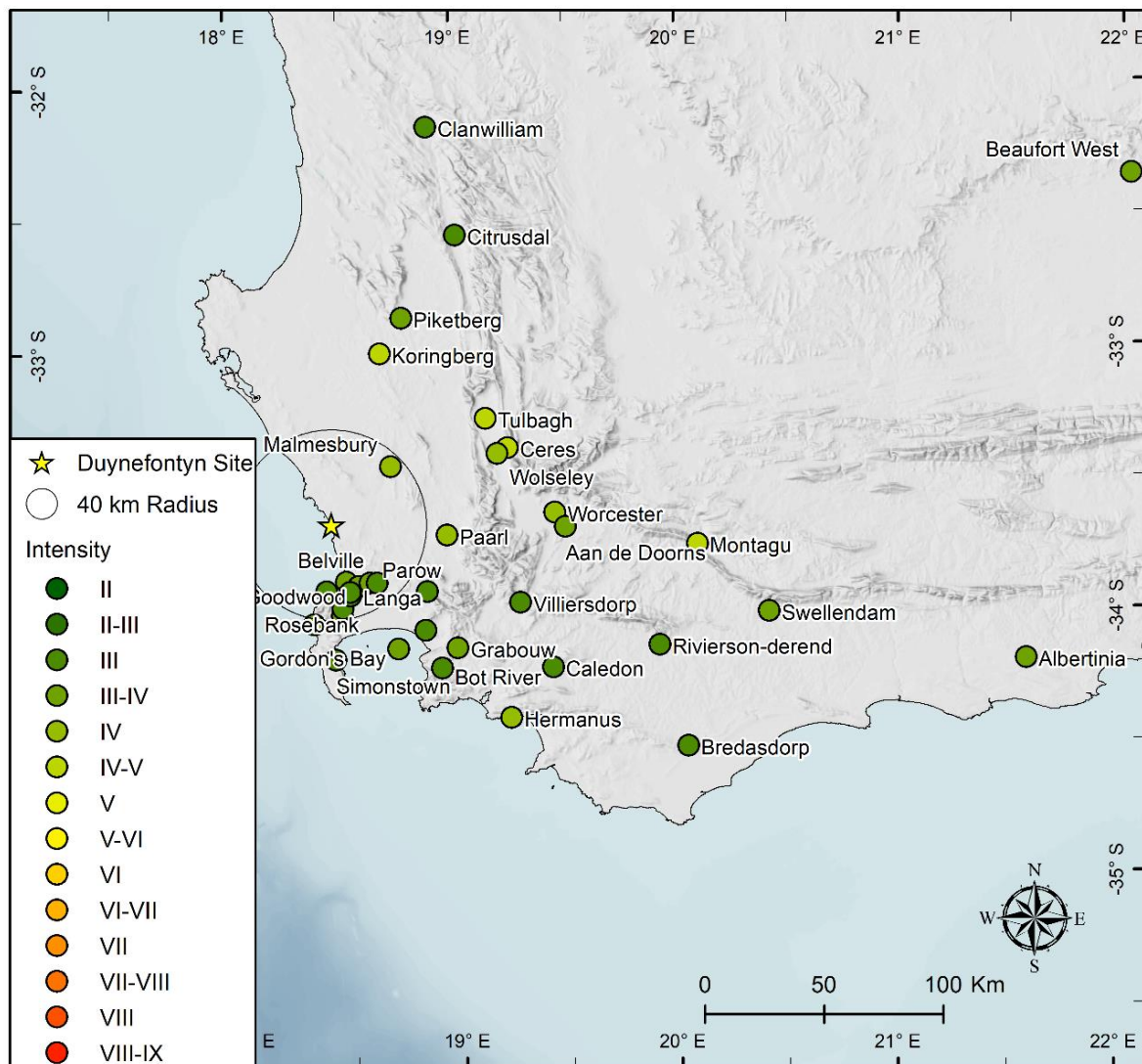

Figure 4-24. Distribution of IDPs in MMI-56 scale for the 29 August 1960 earthquake.

Table 4-11. The epicentre solutions for the 29 August 1960 earthquake using the MEEP2 software.

| Method	Latitude	Longitude	Location error (± km)	Magnitude, M	Magnitude error, (±)	Depth (km)	Weight of solutions
Centroid	-33.464	18.346	44.2	4.4	0.4	20.0	0.6
MEEP	-33.424	18.414	76	4.4	0.3	20.0	0.4
Bakun and Wentworth	-33.543	18.018	110.6	4.1	0.6		0
Pairwise	-32.892	18.079	178.6	4.8	0.6		0
Combined	**-33.448**	**18.373**	**56.92**	4.4	0.45	**20.0**	**1**
CGS Solution	-33.400	19.300		4.0			
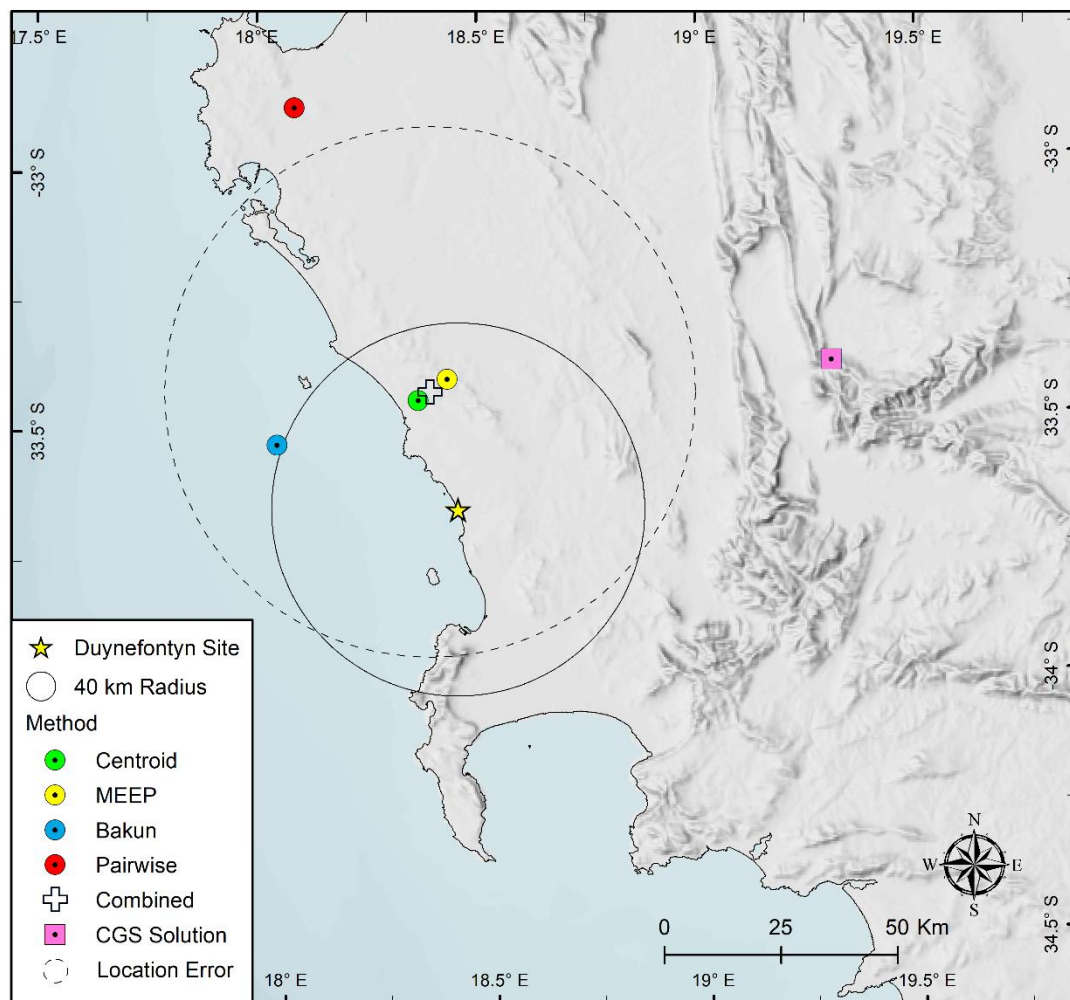
Figure 4-25. Location of epicentral solutions obtained for the 29 August 1960 earthquake using intensity data (Figure 4-24) and the MEEP2 software.

4.3.8 The 27 August 1963 earthquake

The 27 August 1963 earthquake was well recorded with the descriptions of the earthquake effects reported in six issues of four different Cape Town newspapers. Using the observations obtained from the reports, Albini and Flint (2023) created 38 IDPs (Figure 4-26). The distribution of the IDPs imply that the epicentre of the event is located northeast of Cape Town towards the Ceres area. This was confirmed by the source parameters estimated by the SSM TI Team using the intensity data and techniques in the MEEP2 software (Figure 4-27, Table 4-12). Though the Bakun solution had an error value less than 100 km, it was not used by the SSM TI Team in determining the combined solution because its location is far to the northeast compared to the other group of three solutions (i.e., Centroid, MEEP and Pairwise in Table 4-12).

Figure 4-26. Distribution of IDPs in MMI-56 scale for the 27 August 1963 earthquake.

Table 4-12. The epicentre solutions for the 27 August 1963 earthquake using the MEEP2 software.

Method	Latitude	Longitude	Location error (± km)	Magnitude, M	Magnitude error, (±)	Depth (km)	Weight of solutions
Centroid	-33.341	19.186	56.7	4.3	0.2	20.0	0.3
MEEP	-33.557	19.167	50.5	4.2	0.2	20.0	0.4
Bakun and Wentworth	-32.995	20.39	74.8	5.2	0.2		0.0
Pairwise	-33.383	19.356	61.7	4.2	0.3		0.3
Combined	**-33.440**	**19.229**	**55.7**	4.4	0.23	**20.0**	**1**
CGS Solution	-33.100	19.000		4.7			
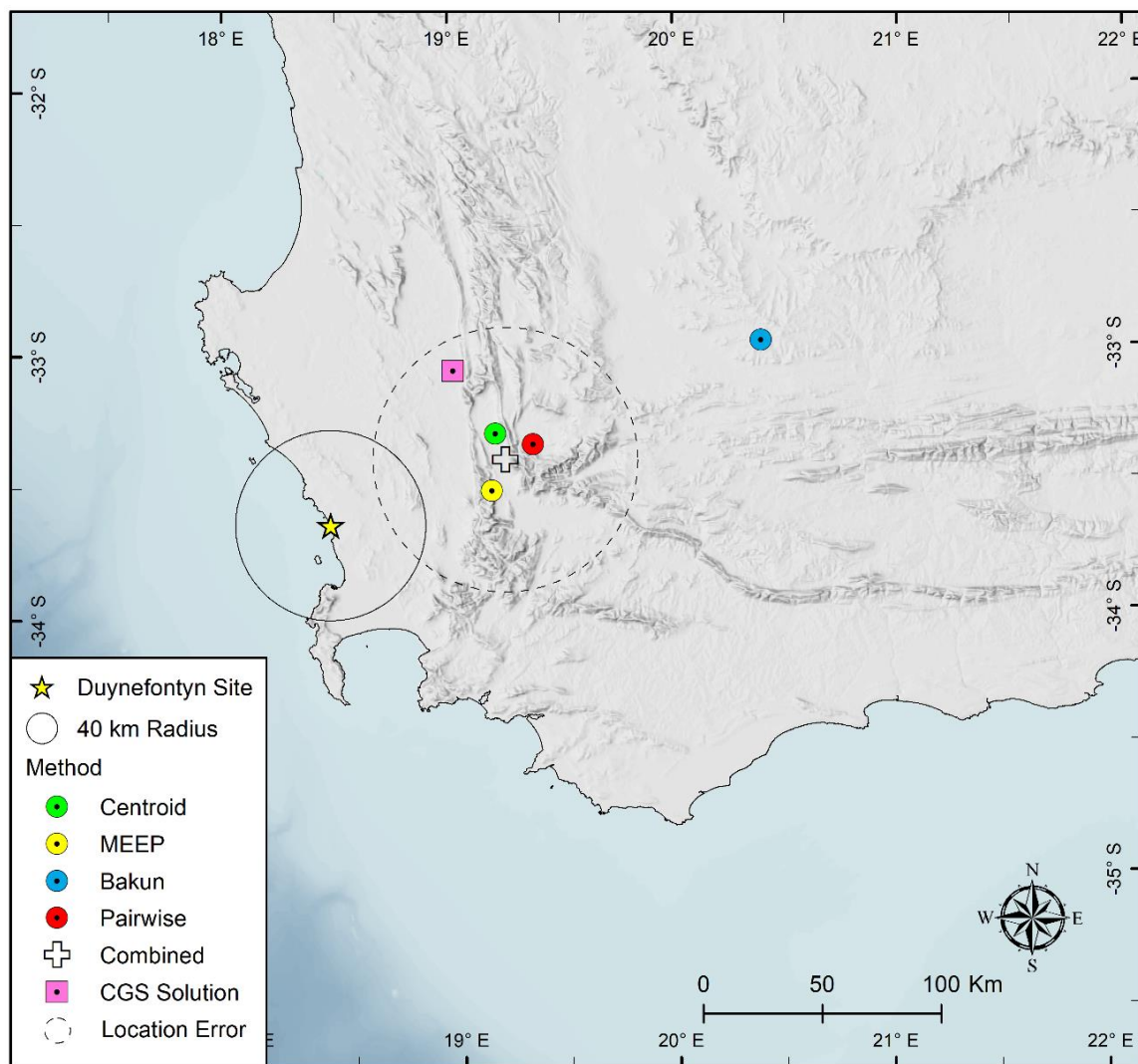
Figure 4-27. Location of epicentral solutions obtained for the 27 August 1963 earthquake using intensity data (Figure 4-26) and the MEEP2 software.

4.3.9 The 11 September 1969 earthquake

According to newspaper reports the 11 September 1969 earthquake was widely felt along the southern coast and immediate interior of the Western Cape Province (Figure 4-28). However, the distribution of the intensity values of the obtained IDPs is suspect given the higher values observed both to the east and the west, with the highest value of intensity V located in the centre of the distribution. Such a distribution made it difficult for the SSM TI Team to identify the epicentral location of the event. It is likely that site effects played a part in the higher intensity values observed both to the east and west. Thus, the epicentral solutions obtained by the SSM TI Team using these data and the software MEEP2, all had quite large errors (Table 4-13). Given the similar and large epicentral error values, the same weight value of 0.25 was applied to each of the solutions to develop the combined solution (Table 4-13, Figure 4-29). The significant location uncertainty was handled in the SSM by consideration of two possible locations for the event: 1) the CGS solution located far east of the site, and 2) the combined location northeast of Cape Town. The SSM TI Team evaluated the impact of these two locations on the catalogue declustering (Section 6.9) and spatial smoothing (Section 8.2.4). Sensitivity of the hazard results to the event location and the final SSM TI Team disposition for dealing with the 11 September 1969 event location are discussed in Section 6.9 and are shown in Figure 6-26. It should be noted that the magnitude value used in sensitivity analysis was the CGS value for both alternative locations.
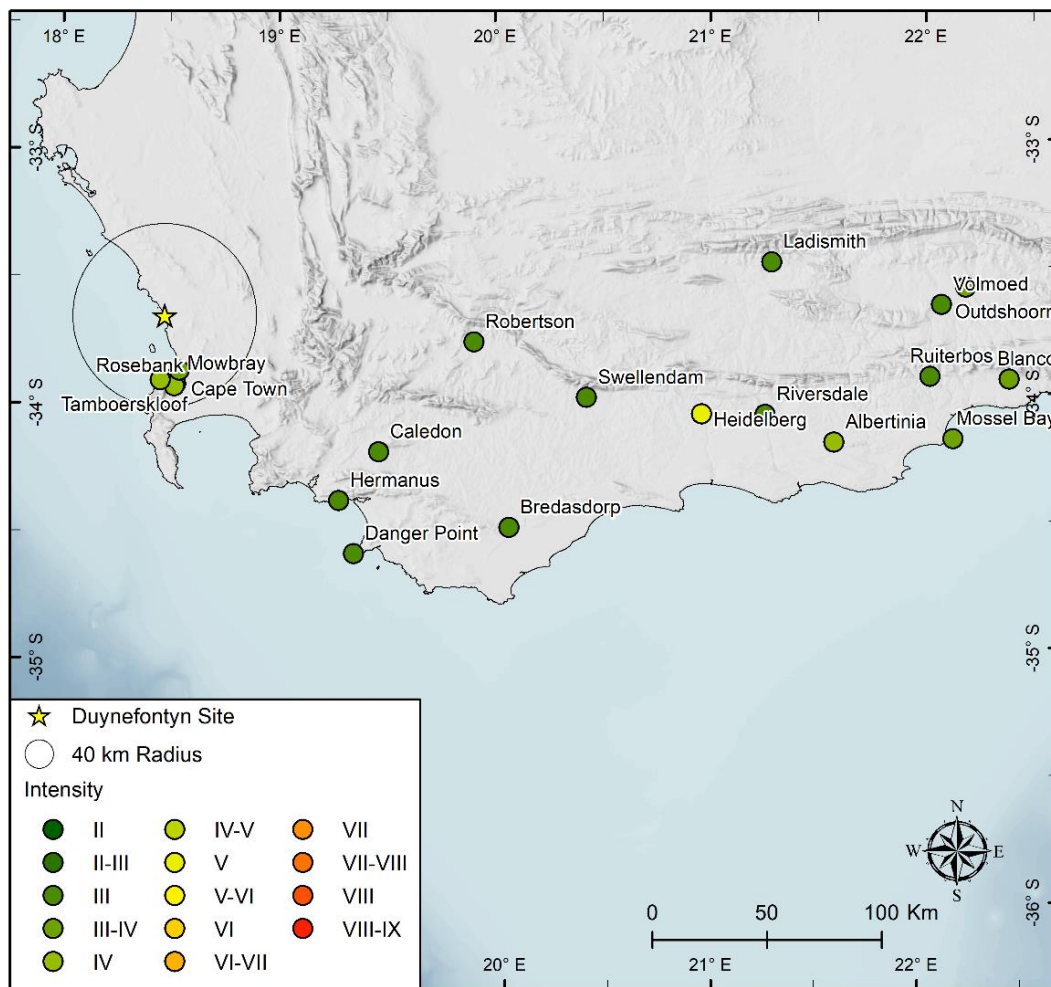

Figure 4-28. Distribution of IDPs in MMI-56 scale for the 11 September 1969 earthquake.

Table 4-13. The epicentre solutions for the 11 September 1969 earthquake using the MEEP2 software.

| Method	Latitude	Longitude	Location error (± km)	Magnitude, M	Magnitude error, (±)	Depth (km)	Weight of solutions
Centroid	-33.943	18.45	195.3	5.4	0.5	20.0	0.25
MEEP	-34.044	19.184	148.3	5.0	0.3	20.0	0.25
Bakun and Wentworth	-32.588	19.225	292.0	5.5	0.4		0.25
Pairwise	-34.652	17.996	280.2	5.6	0.5		0.25
Combined	**-33.807**	**18.714**	**229.0**	5.37	0.41	**20.0**	**1**
CGS Solution	-34.000	21.000		4.8			
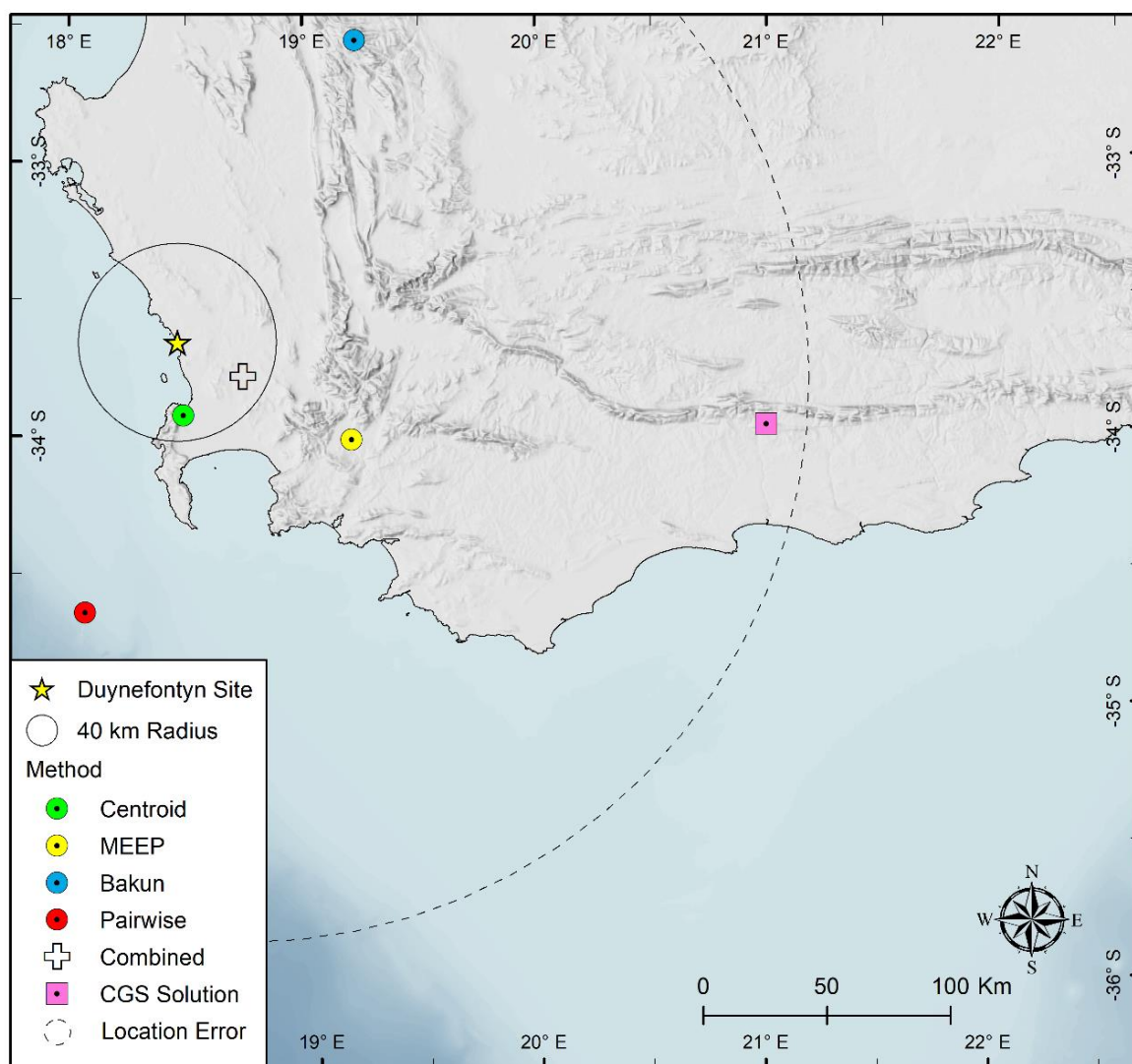
Figure 4-29. Location of epicentral solutions obtained for the 11 September 1969 earthquake using intensity data (Figure 4-28) and the MEEP2 software. Pink square (CGS solution) and cross (Combined solution) show the two alternative locations considered by the SSM TI Team.

4.3.10 The 29 September 1969 earthquake

This earthquake was widely felt throughout the country. The most affected area was near Tulbagh, where there was severe damage to property and 12 fatalities. From newspaper reports, Albini and Flint (2023) created 57 IDPs (Figure 4-30). However, this event has a reliable instrumental location. As a result, the SSM TI Team decided to determine its source parameters (Table 4-14 and Figure 4-31) using the collected IDPs for comparison and estimation of the reliability of the 3rd Generation methods used.
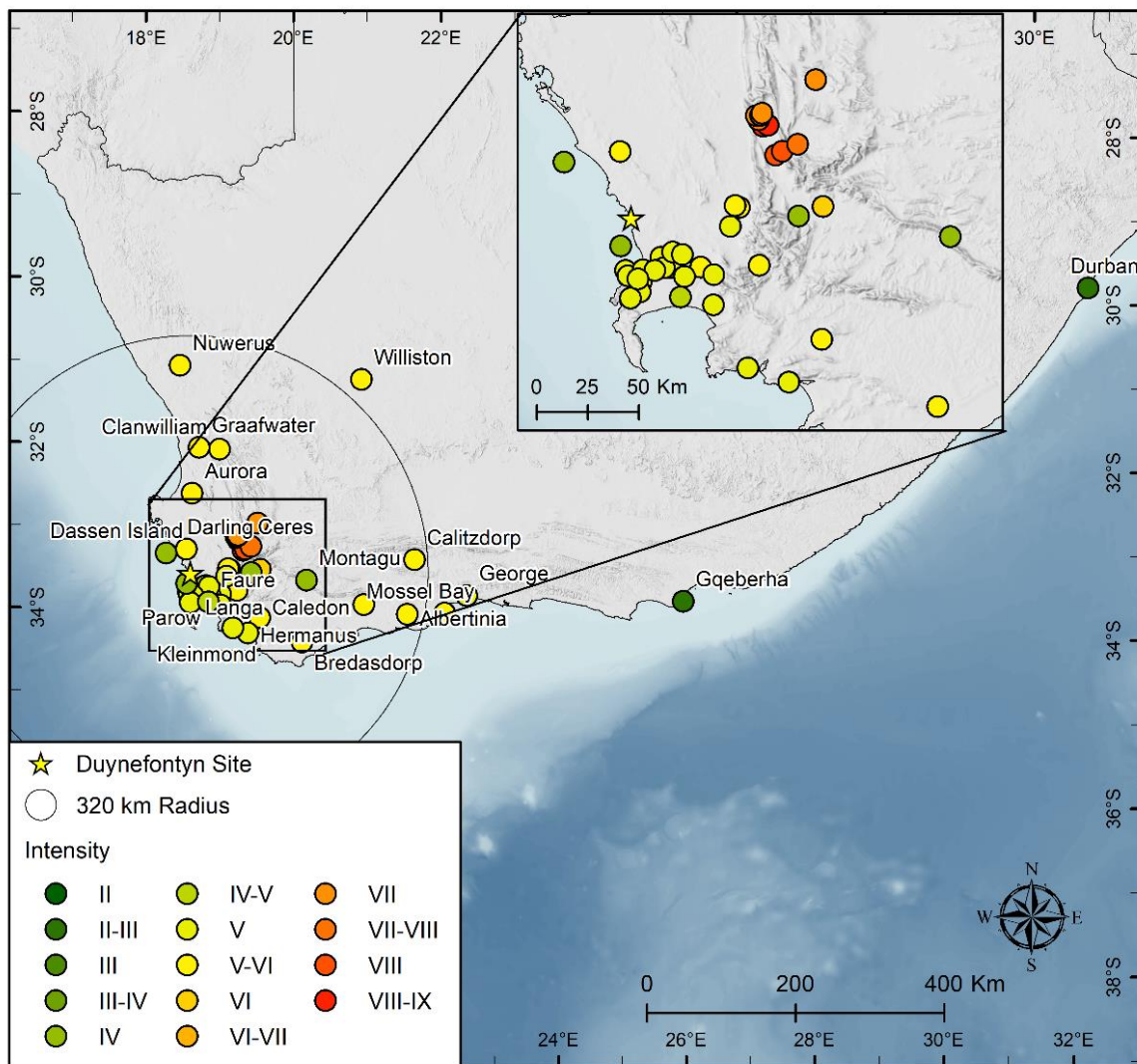
Figure 4-30. Distribution of IDPs obtained for the 29 September 1969 earthquake by Albini and Flint (2023).

Table 4-14. The epicentre solutions as obtained for the 29 September 1969 earthquake using the MEEP2 software.

Method	Latitude	Longitude	Location error (± km)	Magnitude, M	Magnitude error, (±)	Depth (km)	Weight of solutions
Centroid	-33.344	19.184	12.1	6.6	0.6	12.0	0.5
MEEP	-33.225	19.303	14.7	6.6	0.6	14.0	0.5
Bakun and Wentworth	-32.234	20.029	137.1	6.9	0.8		0
Pairwise	-32.772	20.363	116.6	6.6	0.6		0
Combined	**-33.2845**	**19.2435**	**13.4**	6.6	0.62	13.0	**1**
CGS Solution	-33.280	19.240		6.2			
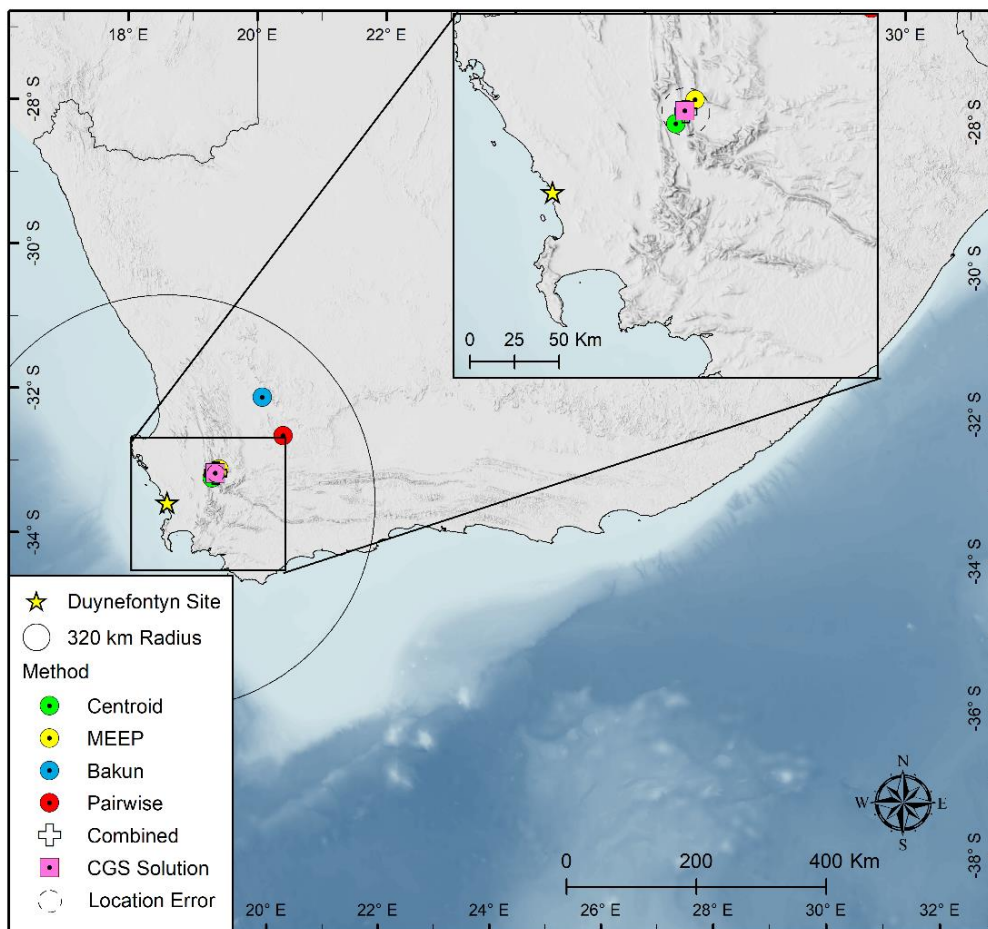
Figure 4-31. Location of epicentral solutions obtained for the 29 September 1969 earthquake using intensity data (Figure 4-30) and the MEEP2 software.

Of the four source parameter solutions obtained, two (Bakun and Pairwise) had epicentral errors greater than 100 km (Table 4-14). Thus, only two solutions (Centroid and MEEP) were used to determine the combined and preferred solution for this event. On comparing, the solution obtained in this study is at the same location as the published CGS instrumental solution (Figure 4-31), giving us confidence in the 3rd Generation techniques used as well as the assumptions made in the process followed in determining the combined solution. In addition, many earthquake-related phenomena were observed and recorded. A summary of the earthquake related phenomena observed during the earthquake are provided on pages 251-253 of Albini and Flint (2023). However, the magnitude value obtained in the MEEP2 analysis is an overestimation of the of the instrumentally determined moment magnitude of 6.2. However, the MEEP 2 analysis does not always overestimate magnitude as half of the MEEP2 estimates were larger than the CGS Solution and half were smaller. The SSM TI Team is uncertain about the reason for this variation in the magnitude values, but it might be caused by the spatial distribution and values of the IDPs. According to Bandt et al. (2005), the CGS local magnitude values for the events analysed in this study were derived from the maximum intensity (I_{max}), using the Richter formula $M_L = 0.66I_{max} + 1.0$ (Gutenberg and Richter, 1954). As described in Section 6.6, the 29 September 1969 instrumental magnitude was used for this study.

Using intensity data and 3rd generation techniques, epicentres are usually estimated according to two basic procedures. The first involves use of an estimate of the centroid of the higher intensities. The second assumes a distance function that the IDPs should follow, and then apply a grid search in which residuals are to be minimised. The second method is applied mainly in the Bakun and Wentworth method, making it susceptible to poor solutions. This happens in cases where the function or attenuation method used is not compatible with local geology. The poor solutions obtained using the Bakun and Wentworth method are illustrated by the large errors (greater than 100km) obtained in the solutions (e.g., Table 4-14 solutions for the 29 September 1969 earthquake).

4.4 DUYNEFONTYN SITE GEOLOGY

The Duynefontyn site sits atop relatively complex geology characteristics that consist of steeply-dipping to nearly vertical bedding of the Malmesbury Group strata uncomfortably overlain by Miocene to Holocene marine, estuarine, and aeolian strata atop a large wave-cut platform. Differential erosion of the Malmesbury Group layers on the wave-cut platform produced a corrugated bedrock surface (Figure 4-32a and b).

The SSM and GMM TI Teams determined that this bedding geometry and erosional fabric could potentially challenge one-dimensional site response analyses, which is traditionally based on an assumption of infinite horizontal layers that are then used to derive one-dimensional vertical V_S profiles. Thus, to characterise the Duynefontyn site, the SSM TI Team evaluated and assessed the site geology in detail. As described below, this evaluation and assessment included borehole data, geologic maps, photographic records, and a first-hand account of the construction of the KNPS (Barker, 2023). During construction of the KNPS, the Cenozoic cover was cleared off to expose the wave-cut platform and the corrugated steeply dipping beds of the underlying Malmsbury strata (Figure 4-32a). The SSM TI Teams assessment was provided to the GMM TI Team who used this information to investigate possible two-dimensional site response effects, as described in Section 9.4.6. The two-dimensional analysis was also the subject of a GMM TI Team supporting study conducted by de la Torre and Bradley (2023). While the GMM TI Team ultimately did not deviate from one-dimensional site response, this evaluation of the geological conditions at the Duynefontyn site may provide a template for studies at other geologically complex sites.

4.4.1 Bedrock geology (Malmesbury Group)

Within 40 km of the Duynefontyn site, comprehensive data collection activities and investigations (e.g., Dames and Moore, 1976; Rogers, 1979; 1980; Visser, 1988; De Beer et al., 2008 Engelsman, 2022; Claassen et al., 2024) reveal that both the Duynefontyn and Koeberg sites are exclusively underlain by bedrock of the Tygerberg Formation that comprises low-grade, immature, deep water, turbiditic metasediments of predominantly fine- to medium-grained, thinly bedded alternating greywackes/metagreywackes, shales, siltstones, and mudstones with occurrences of phyllites that exhibit a fining sequence from east to west (Figure 4-32). Borehole data at Koeberg and Duynefontyn (Dames and Moore, 1976; Day, and Ridgway, 2000; 2006; SRK, 2008b) indicate roughly equal proportions of arenaceous and argillaceous lithological units for the Tygerberg Formation. Lithological units are generally laterally persistent in thickness along strike. The formation consists of gradational sequences with beds grading mainly from coarse to fine in upward-fining successions.
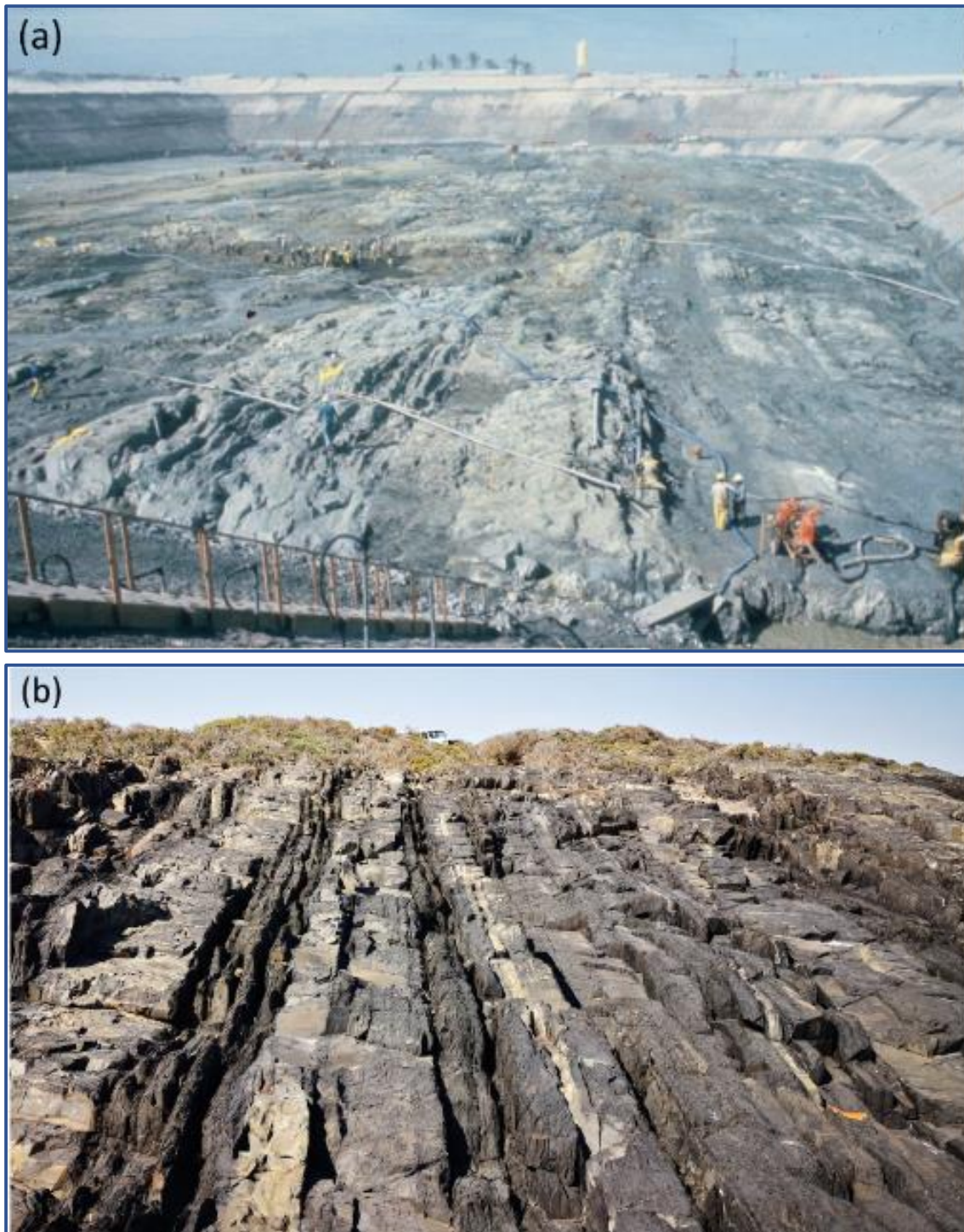
Figure 4-32. (a) Tygerberg Formation exposed in excavations during the construction of the KNPS. (b) Coastal exposures of the alternating metasediments of predominantly fine- to medium-grained, thinly bedded alternating greywackes/metagreywackes, shales, siltstones, and mudstones of the Tygerberg Formation just south of Grotto Bay (S 33°31'35.8"; E 18°19'01.2").

Dames and Moore (1977) identified four different rock sequences at Koeberg that can be extended along strike to the Duynefontyn site (Figure 4-33).

1. Greywacke: Massive, light to dark grey or greenish grey, medium to fine grained poorly graded greywacke with occasional dark grey shale partings and very thin mudstone beds. These units range in thickness from <2-10 m.
2. Predominant greywacke: Greywacke with numerous thin beds and laminae of greenish orange siltstone and grey mudstone. Interbedded mudstone units of up to 40 cm were mapped. Units range in thickness between <2-12 m.
3. Predominant mudstone: Dark grey to dark greenish grey mudstone with abundant siltstone and thin beds of greywacke. Units range in thickness from <2-9 m.
4. Mudstone: Dark grey to dark greenish grey mudstone with minor grey siltstone laminae and occasional thin beds of fine-grained greywacke. Thickness for these units range from <2-5 m.

Quartz dominated (70%) greywackes are fine-to-medium grained and are generally massive or laminated, occasionally containing subrounded to angular clasts. Small-scale cross-stratification, cross-lamination and bedding-parallel lamination are noted in finer-grained greywackes. Siltstone and mudstone are massive or frequently horizontally laminated. Lensoidal bodies exhibit whitish weathering laminae, possibly due to diagenetic silicification. Soft-sediment deformation structures are abundant and include load casts, ball-and-pillow structures, and convolute bedding (Theron, 1984; Roberts, 2001). Similar lithologies to those observed at the KNPS were identified in boreholes at Duynefontyn (Figure 4-34) but given the metre-scale alternating sequence of lithologies, and spacing of boreholes, the construction of a lithostratigraphic section for the site was not possible.

Most boreholes at Koeberg and Duynefontyn do not exceed 30 m depths, with the maximum depth drilled being 120 m in borehole ST1 (Claassen et al., 2023). Although granitic intrusions associated with the Cape Granite Suite were not encountered in any boreholes, given the shallow borehole depths their presence at depth in the area cannot be excluded.

In addition, no boreholes at Duynefontyn intercepted a Mesozoic dyke. However, given their narrow extent (frequently less than 10 m) and wide borehole spacing, their possible presence cannot be excluded, especially considering their occurrence along coastal exposures between Milnerton and Bloubergstrand. A ~7 m thick mafic dyke was encountered near the south-eastern boundary of the KNPS site in inclined borehole 603, some 300 m from the coastline (Dames and Moore, 1976).
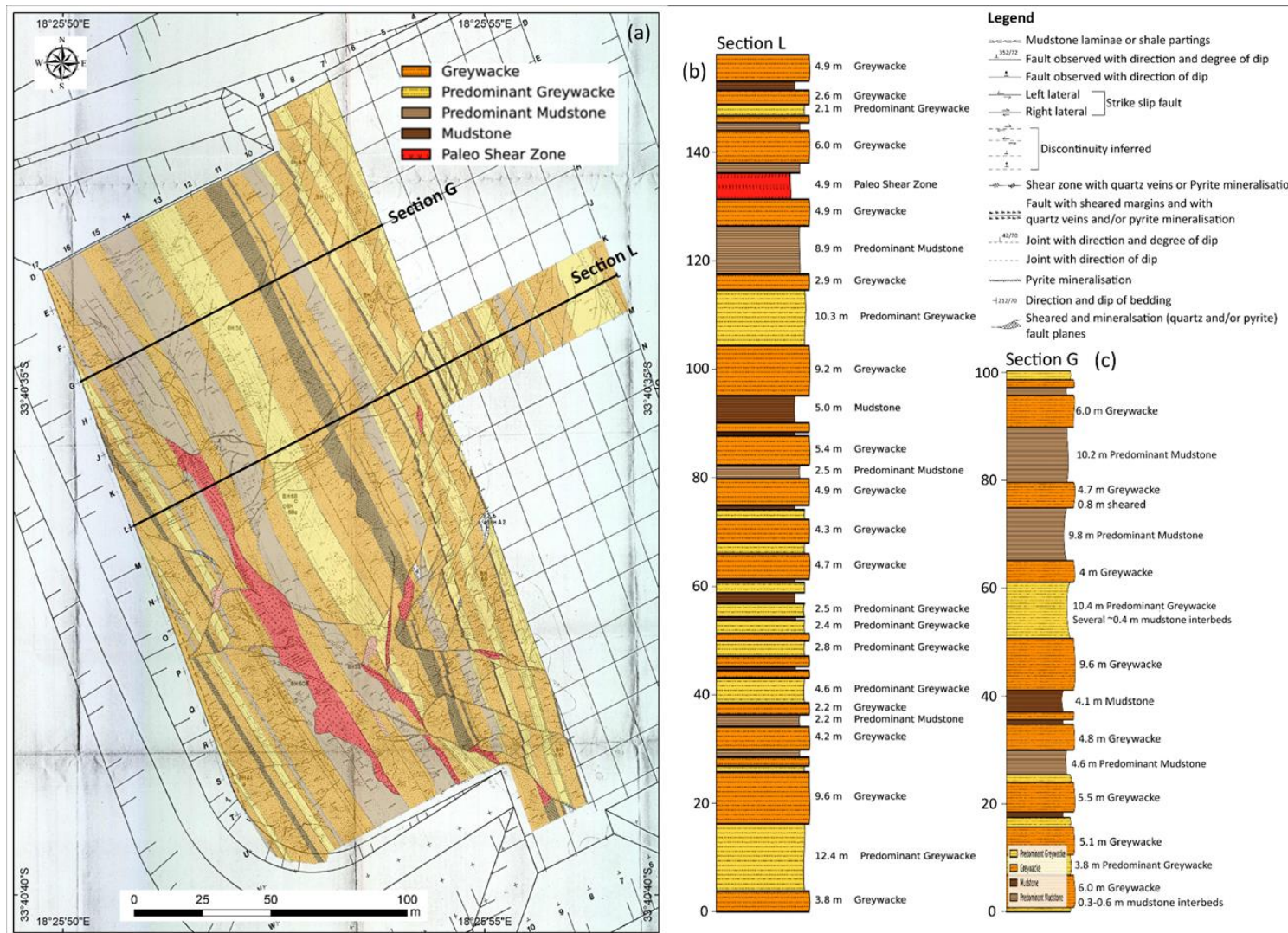
Figure 4-33. (a) Surface lithology and structure of the Tygerberg Formation mapped at excavations during the construction of the KNPS (after Dames and Moore, 1976). (b and c) Lithostratigraphic sections G and L orientated perpendicular to bedding strike. The thicknesses of lithological units were calculated perpendicular to strike (150°) using an average dip of 75°.
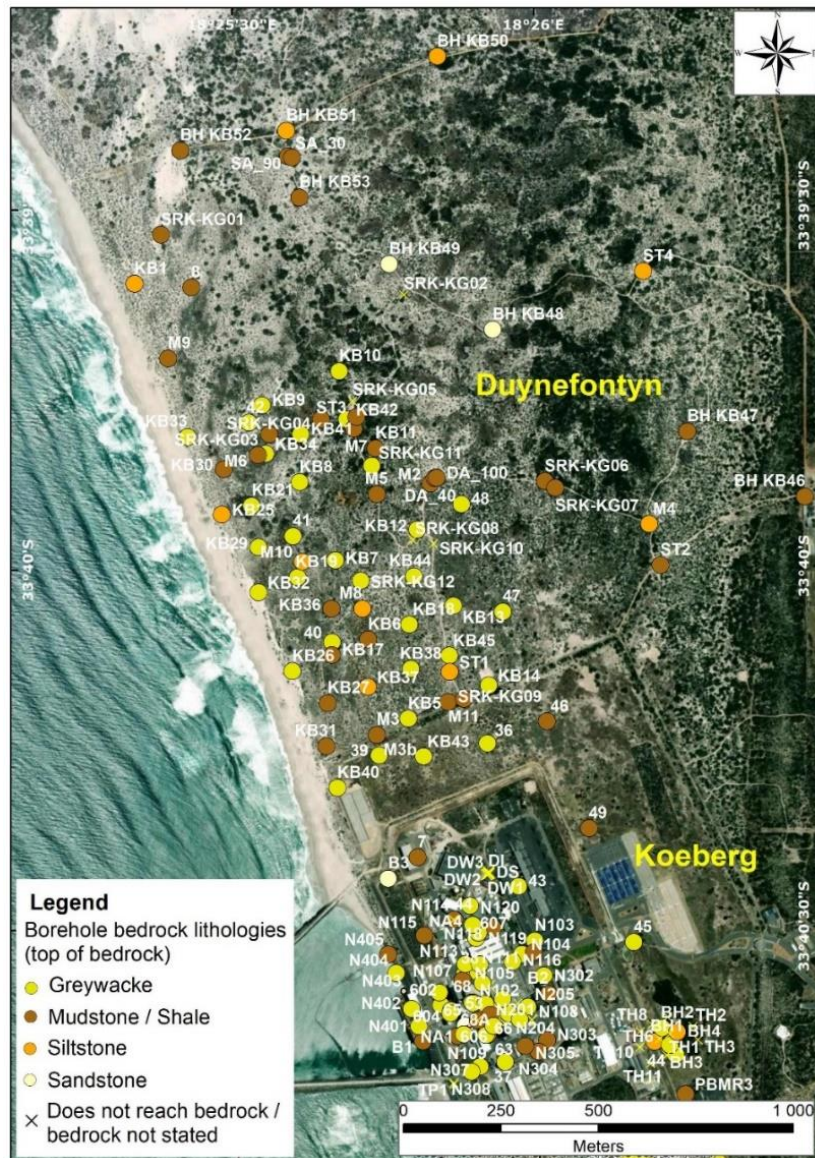
Figure 4-34. Top of bedrock lithology types intercepted in borehole data at Koeberg and Duynefontyn.

Excavations undertaken during the construction of the KNPS revealed that the overburden sediments were deposited on a weathered, uneven, gently seaward sloping bevelled and bioturbated wave-cut bedrock surface with steeply SW or NE dipping (70° – 90°), NNW-SSE striking beds. The broad planation surface at Koeberg is situated at an average elevation of 11 m bmsl. The bedrock surface exhibited thousands of shallow tubular *Pholad* burrows (Piddock bivalve molluscs) that penetrated bedding planes, joints, and faults, especially in more argillaceous lithologies (Figure 4-35a and b). No offset of these trace fossils was observed across mapped fractured/faulted zones (Rogers 1979, 1980; Barker, 2023), suggesting that the mapped bedrock faults must predate the age of the trace fossils. Unfortunately, the age on the terrace is unknown but is assumed to be older than a unit containing shark teeth roughly 2 m above bedrock that forms part of the Duynefontyn Member of the Varswater Formation which has an age range of Early Miocene to Pliocene. The lowermost gravel unit (Silwerstroom Member) of the Varswater Formation above bedrock was most likely laid down as a regressive deposit during the pre-terminal Miocene, before the early Pliocene regression.
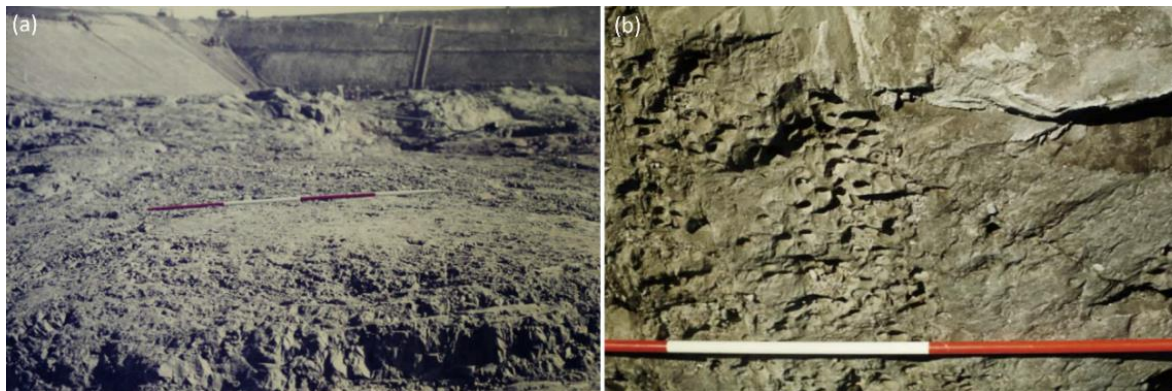
Figure 4-35. (a) Bedrock surface at Koeberg exbibit numerous shallow tubular *Pholad* burrows (Piddock bivalve molluscs). (b) A close-up image of the burrows that penetrated bedding planes, joints, and faults, especially in more argillaceous lithologies.

The Duynefontyn site contains a high density of boreholes (Murray and Saayman, 2000; Day and Ridway, 2006; SRK, 2008 a, b; Flanagan and Rosewarne, 2008; SRK, 2021; Claassen et al., 2024) that enabled the creation of an interpolated 1 m contour interval palaeotopography map of the bedrock surface (Figure 4-36a). Results show all bedrock within the contoured map area occurs below present-day sea level with elevations ranging between 26.6 m bmsl (BH607, just NW of the KNPS) and 1.0 m bmsl (SRK-KG04, at Duynefontyn, -390 m from the coastline) below overburden cover. Both these maximum and minimum elevations are extreme and isolated values, with average values across both sites calculated at 10.1 m bmsl. Topographically, bedrock elevation increases in a NE direction inland away from the coastal margin. At the Duynefontyn site itself, the lowest bedrock elevation of 16.34 m bmsl was encountered in borehole KB31. Towards the northwest extent of the Duynefontyn site, a NE-SW trending topographic low extends inland for at least 1 km. Claassen et al. (2024) identified two coast parallel, NNW-SSE trending wave-cut platforms at Duynefontyn based on the interpolated palaeobedrock topography and presence of overlying marine gravels. The first, lower, near-coastal marine terrace occurs at elevations between 10 to 12 m bmsl. A second, slightly higher probable terrace is located at elevations between 5 to 7 m bmsl (Figure 4-36b to e).
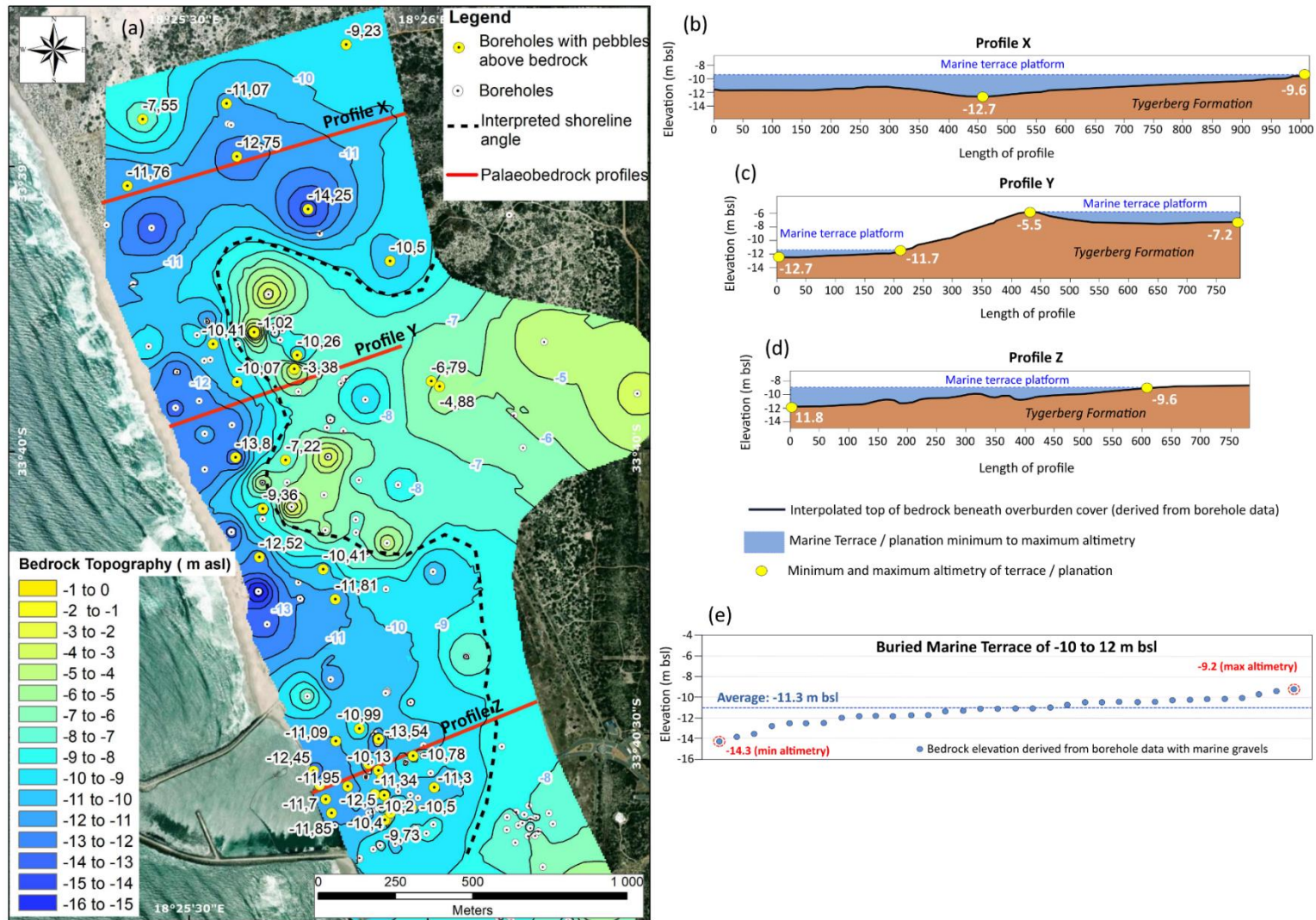
Figure 4-36.(a) Map depicting interpolated 1 m contour interval elevation map of the bedrock below Cenozoic overburden at the Duynefontyn site. (b-d) Cross-sections X, Y and Z perpendicular to the coastline and bedding strike across the interpolated palaeotopography surface. (e) Elevations of bedrock encountered in boreholes across the lower 10 to 12 m bmsl marine terrace platform.

The degree and depth of weathering of the Tygerberg Formation is highly variable across both sites (Figure 4-37). Strata range from unweathered to highly weathered. Unweathered greywacke is found within 6 m of the bedrock surface while weathering in the mudstones and siltstones extends to depths of 26 m in places. Generally, strata are highly weathered at the surface and become moderately to slightly weathered/unweathered with depth. The degree of weathering appears linked to lithology types with localised bedrock lows often forming in less competent strata such as mudstone. Zones of highly to completely weathered, brecciated/crushed rock are associated with the very fine-grained mudstones (Day and Ridgway, 2006). Geotechnical boreholes drilled by SRK (2008, 2021) defined weathered (soft to medium hard rock) and unweathered (hard to very hard rock) at the Duynefontyn site (Figure 4-38).
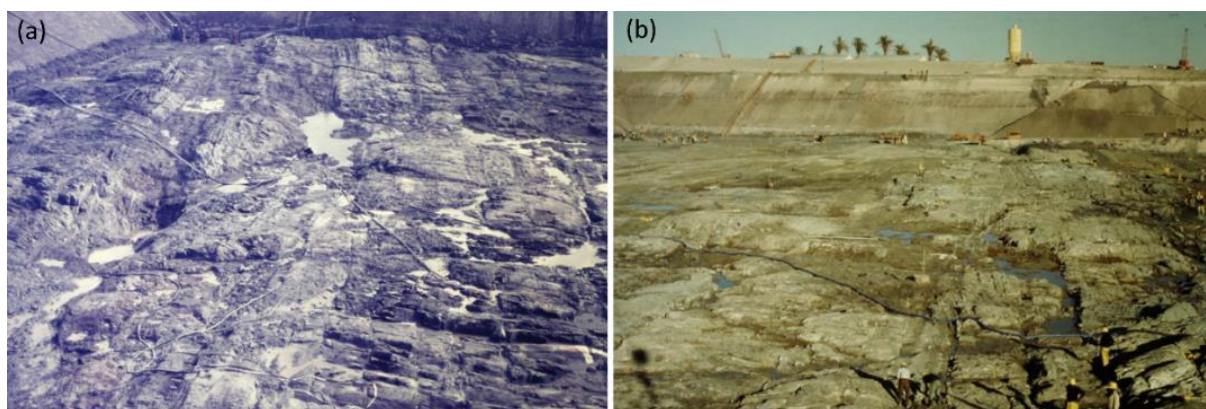

Figure 4-37. (a and b) Undulating, uneven planated bedrock surface exposed during excavations at Koeberg showing the differential weathering associated with the various lithologies (Photos J.Rogers).

4.4.2   Overburden geology (Sandveld Group)

Bedrock at Koeberg and Duynefontyn is overlain by unconsolidated to semi-consolidated, marine and aeolian sediments of the Sandveld Group deposited during a series of marine transgressions and intervening regressions. Borehole data (Murray and Saayman, 2000; Day and Ridgway, 2006; SRK, 2008a, b; Flanagan and Rosewarne, 2008; SRK, 2021, Claassen et al., 2024) enabled the creation of a 1 m interval isopach map across the Koeberg and Duynefontyn sites (Figure 4-39). The thickness of these overburden sediments range between 12.3 m (borehole B3, ~320m NW of Koeberg) to 35.2 m (borehole KB50, northwestern extent of Duynefontyn, ~1040 m from the coastline) with an average thickness of 20.8 m. Thickness increases with increasing distance from the coastline. Delineating the thickness of individual formations within the Sandveld Group across boreholes at Duynefontyn is not possible because borehole log descriptions are often not formation specific, and do not provide adequate lithological descriptions to facilitate accurate differentiation to formation level to facilitate correlation.
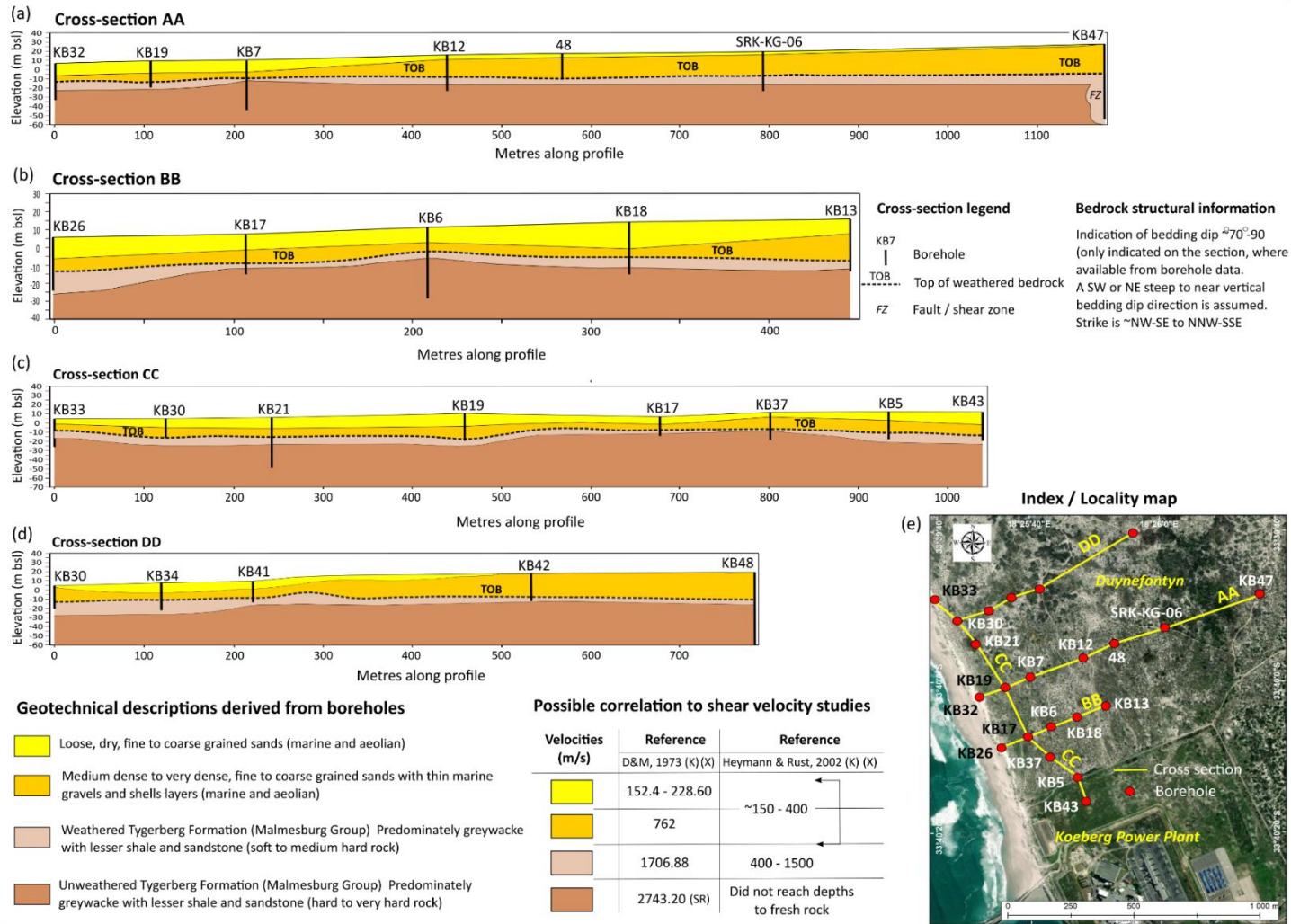
Figure 4-38. (a-d) Cross-sections depicting the geotechnical properties of overburden and bedrock, as defined by the SRK (2008, 2021) drilling programme at Duynefontyn, where differentiation was made between weathered (soft to medium rock) and unweathered (hard to very hard rock). (e) Index map showing locations of cross sections.
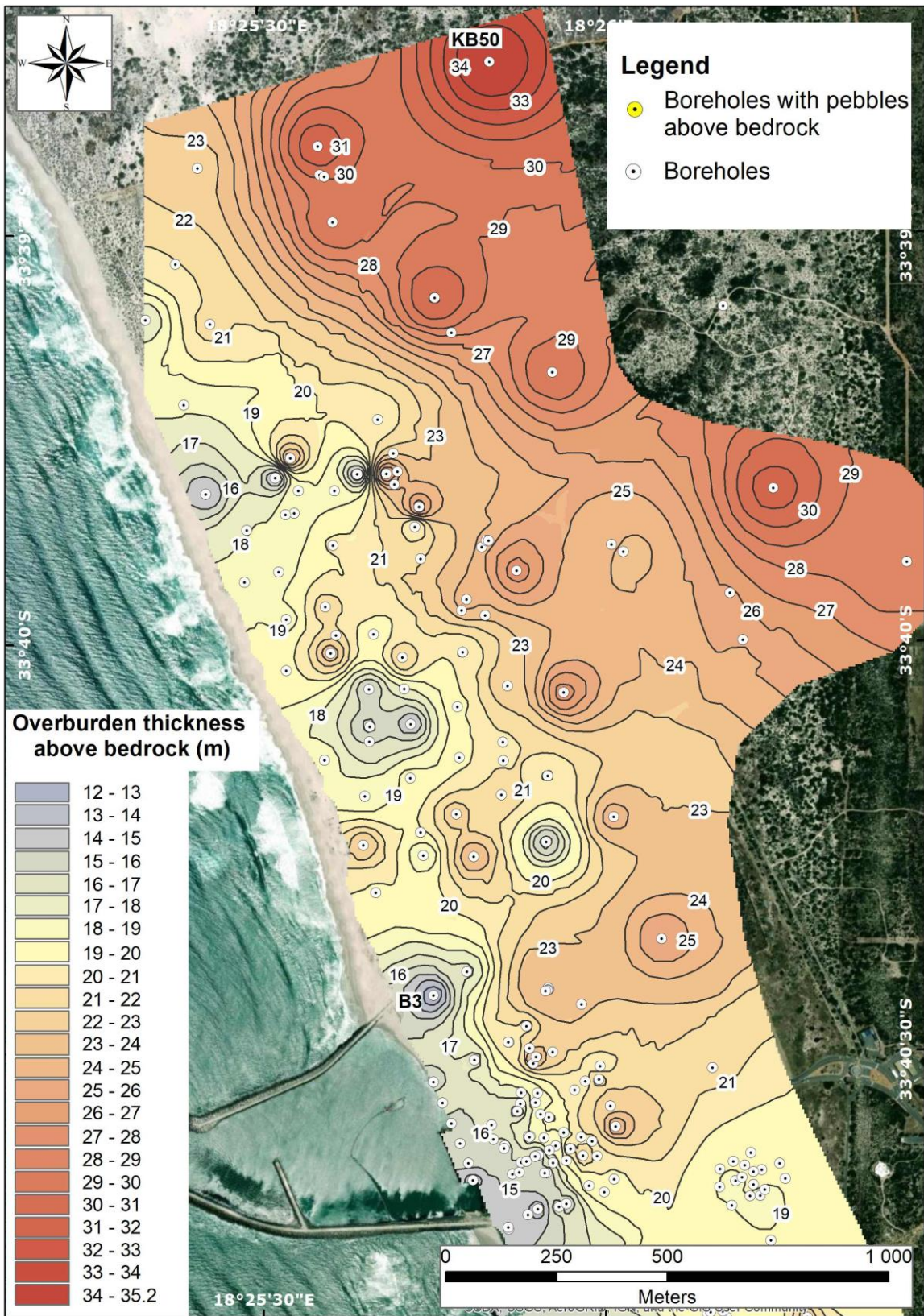
Figure 4-39. Interpolated isopach map (1 m intervals) showing the overburden thickness at the Duynefontyn site.

Figure 4-40 provides a lithostratigraphy for the Sandveld Group along the southwest coast as it is currently accepted by the South African Commitee for Stratigraphy (SACS) and detailed by Roberts et al. (2006). Although the lithostratigraphic subdivisions of the various formations and their members have varied between authors (e.g., Rogers 1979, 1980, Roberts 2001, 2002), the SSM TI Team has chosen to adopt the SACS approved lithostratigraphy and the additional two non-SACS approved members of the Varswater Formation at the Koeberg site as subdivided by (Roberts, 2001) and (De Beer, 2008). The SSM TI Team also notes that overburden lithostratigraphy can be highly variable across both sites as well as the greater southwest coast and that the lithostratigraphy of the Sandveld Group as represented by Roberts et al (2006) is an idealised, composite section. At Koeberg and Duynefontyn the Sandveld Group comprises the Varswater, Velddrif, Langebaan, Springfontyn, and Witzand Formations
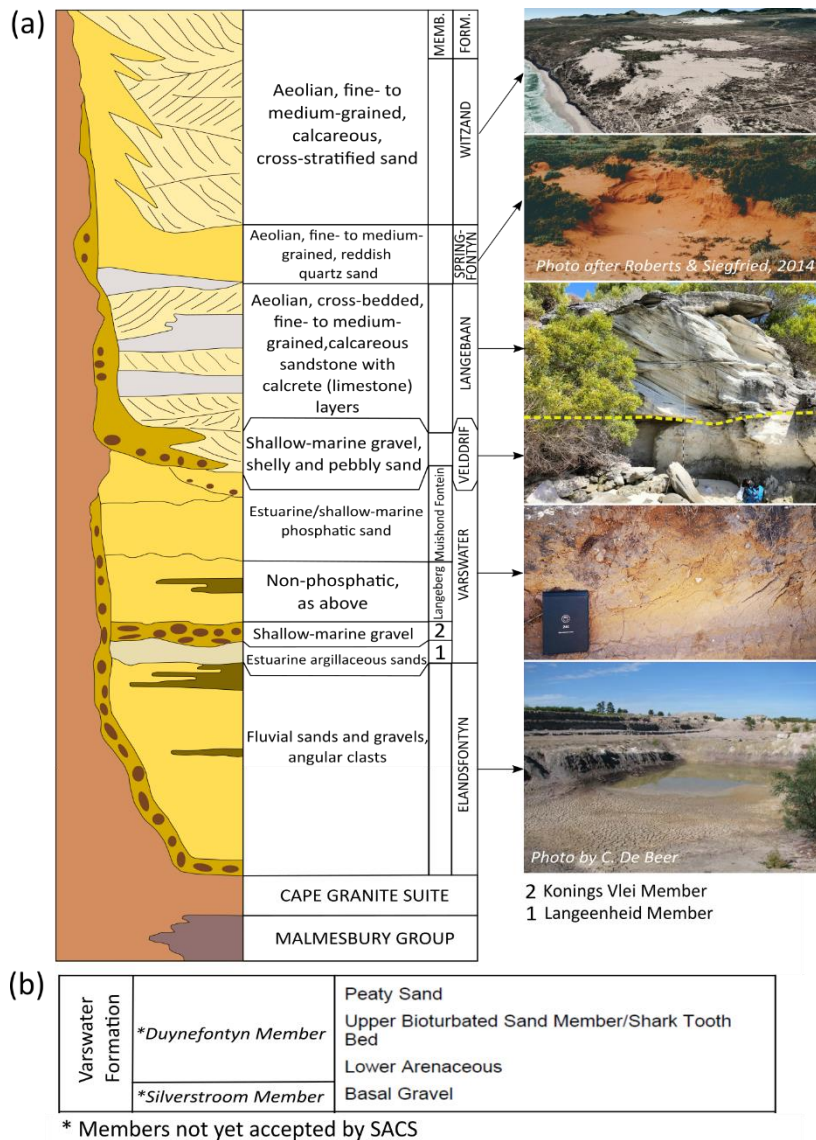

Figure 4-40. (a) Lithostratigraphy of the Sandveld Group (after Roberts et al., 2006). (b) Two additional members (Silwerstroom and Duynefontyn) of the Varswater Formation, identified during excavations at KNPS (Rogers, 1979; 1980). These member subdivisions as outlined by Roberts, (2001) have not yet accepted by the South African Committee for Stratigraphy (SACS).

Varswater Formation

The estuarine to shallow marine phosphatic Varswater Formation is traditionally subdivided into four Members across the southwest coast: Langeenheid Clayey Sand, Konings Vlei Gravel, Langeberg Quartz Sand, and the Muishond Fontein Pelletal Phosphorite Sand (Tankard, 1974; Rogers 1980, 1982; Hendey, 1981; Hendey and Dingle, 1983) (Figure 4-41a). Rich and diverse fauna of the Langeberg Quartz Sand and Muishond Fontein Pelletal Phosphorite Members suggests a Mio-Pliocene age (~5 Ma) (Hendey and Gentry, 1970; Hendey, 1976, 1981) and an inferred Middle Miocene age (~10 Ma) for the Konings Vlei Gravel Member. Two additional units, recognised as the Silverstroom and Duynefontyn Members (Miocene-Pliocene), but not yet accepted by SACS, were identified during excavations at the KNPS (Rogers, 1979, 1980; Rogers et al., 1990; Roberts, 2001) (Figure 4-40b). The various lithological beds and correlation of the lithological facies comprising these two members, as originally subdivided by Rogers (1979, 1980), were questioned by Roberts (2001). Therefore, the description as it follows below, details the more recently published works of Roberts (2001) that described the geology of the Melkbosstrand area as well as from De Beer et al. (2008) who mapped the geology of 40 km radius around Koeberg. The Silwerstroom Member occurs above the Tygerberg Formation and correlates to the marine *'Basal Gravel bed'* first identified by Rogers (1979). The unit is composed of well-rounded to angular pebbles and cobbles of Malmesbury Group and vein quartz clasts set in a matrix of dark grey quartzose sand rich in phosphatised shell fragments (Figure 4-41a and b). Borehole data indicates that this horizon is generally a few centimetres to <2 m thick at average elevations of 10-12 m below sea level. Some boreholes (SRK, 2008a) record thicker gravel accretions up to 14 m in isolated bedrock pockets. The lowermost gravel unit of the Varswater Formation was likely deposited as a regressive deposit during the pre-terminal Miocene, before the Early Pliocene regression.

Figure 4-41. (a) Basal gravels of the Silwerstroom Member (Varswater Formation) that correlates to the '*Basal Gravel bed*' first identified by Rogers (1979) during excavations at Koeberg and (b) at Duynefontyn in borehole M3 at a depth of 19.7-20 m (Claassen et al., 2023).

Overlying the Silwerstroom Member is the Duynefontyn Member which collectively correlates to the '*Lower Arenaceous*', '*Upper Bioturbated Sand*' and '*Peaty Sand*' beds mapped by Rogers (1979, 1980) at the Duynefontyn site. The member comprises a widespread and persistent basal arenaceous horizon of light grey, very well-sorted fine quartzose sand with minor phosphatised shell fragments that is subhorizontally bedded with signs of bioturbation and generally less than 2 m in thickness. Overlying this unit is a bed composed of a bioturbated, light olive grey to pale yellowish brown, slightly muddy and somewhat gravelly, well sorted, and fine sand (Figure 4-42) that reaches a thickness of 10 m between the elevations of 8.1 m bmsl and 1 m amsl. This bed is of particular importance since it contains a 10 cm thick bed of slightly gravelly to coarse sand containing ample shark's teeth, fish and whale debris referred to by Rogers (1979, 1980) as the '*Shark Tooth Bed'.* The fossil content ranges from sharks' teeth (*Megaselachus megalodon* and *Carcharodon carcharias*) (Figure 4-43) to teleost fish remains (vertebrae, teeth, scales, and spines), marine-mammal fossils (whale vertebrae, earbones and ribs; dolphin teeth; seal teeth) as well as bird bones (heelbones of the penguin *Nucleornis insolatis*). Similar fossils are found throughout the Duynefontyn Member, but they are most abundant in this layer at elevations ~8 m below present sea level. A 10-15 cm thick unit of moderately sorted, gravelly, muddy fine sand, rich in organic matter, sporadically caps the Duynefontyn Member in places.

Figure 4-42. A portion of the Duynefontyn Member exposed in excavations during the construction of the KNPP. The lower portion shows a completely bioturbated bed overlain by a sandy bed containing gastropods and cobble-sized peaty intraclasts (Photo by J.Rogers).
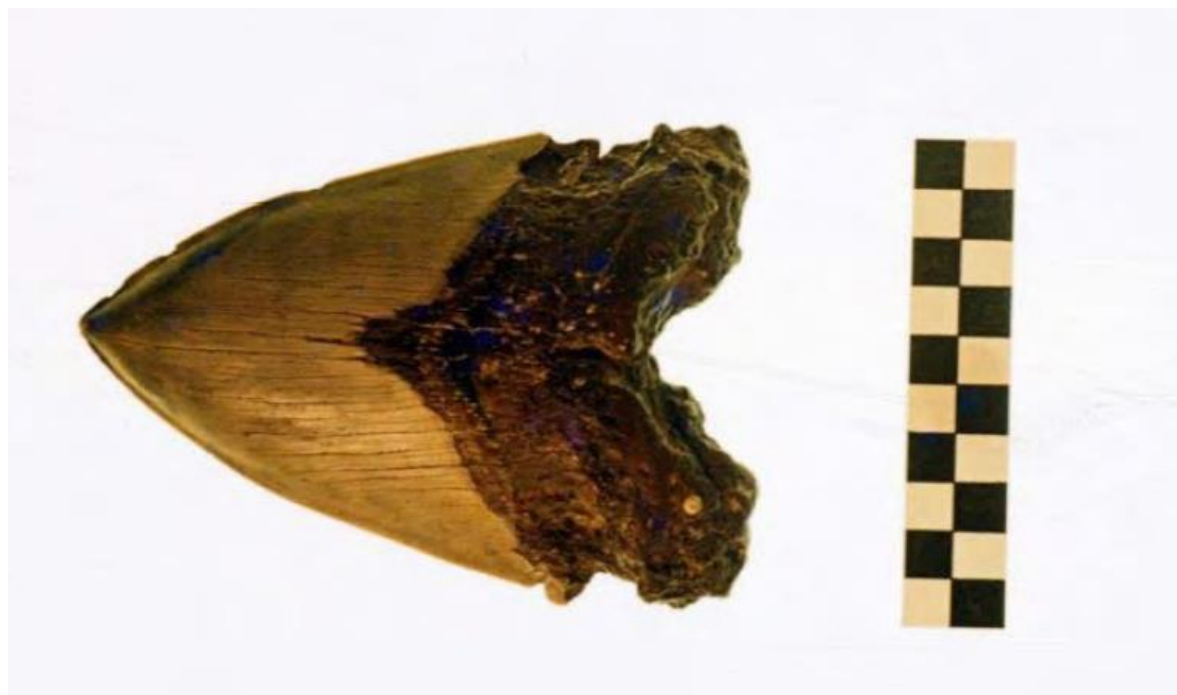

Figure 4-43.Tooth of the Miocene-Pliocene shark *Megaselachus carcharodon* found in excavations at the KNPP in the Duynefontyn Member (Photo taken by J.Rogers). Scale is in centimetres.

Velddrif Formation

The Late Pleistocene ~120 ka (Roberts and Berger, 1997) Velddrif Formation is composed of non-phosphatic gravelly conglomerate, shelly foreshore and coquina deposits with cold water fauna related to Marine Isotope Stage 5e (Tankard, 1976a; Rogers, 1983). The formation reaches a maximum thickness of 17 m and is intermittently exposed along the southwest coast, with most exposures situated outside the site areas near Velddrif, Saldanha Bay, and in the vicinity of Milnerton. The Velddrif Formation deposits are well documented by various authors who also referred to deposits as the outdated and SACS unproved lithostratigraphic names of *'Milnerton Beach Member', 'Milnerton Formation'*, '*Diep River Member'* and *'Killarney Member'* (Kensley, 1972; Rogers, 1980; Theron et al., 1992; Roberts, 2001, 2006; Roberts and Siegfried, 2014). A maximum height of ~7 m asl was initially indicated (Tankard, 1976a, b; Rogers 1980). The formation was encountered by Rogers (1980) at the pumphouse excavations, near the coastal margin at the KNPS site, where the formation attained a 3.5 m thickness.

Langebaan Formation

The sporadically occurring Langebaan Formation represents a multigenerational dune system comprises of the older Diazville Member and younger Kraal Bay Member. Both members comprise cross-bedded biocalc-siliclastic aeolianite, with terrestrial snail fossils and rhizoliths (Rogers et al., 1990; Roberts et al., 2006; Roberts and Siegfried, 2015). The age of the Langebaan Formation ranges from Early Pleistocene Diazville Member to the Late Pleistocene Kraal Bay Member (Roberts and Siegfried, 2015). Archaeological evidence and infrared stimulated luminescence conducted on aeolianites of the Kraal Member known to overly marine-related MIS 5 e deposits of the Velddrift Formation provided dates of 107±7 ka and 103±7 (Roberts and Berger, 1997). Studies undertaken of the Geelbek dunes also supported the existence of at least two chronologically distinct dune formations of ~140 ka and 65 ka North of Duynefontyn. In the Velddrif area, Mammalian fossils in aeolianites of the lower Diazville Member unconformably overlying the marine packages of the Varswater Formation suggest a Late Pliocene age (Hendey 1981a, b). The Langebaan Formation is well exposed only along the Springfontyn Cliffs (Rogers, 1980). Borehole data indicate that the formation probably does not exceed 10 m in thickness in the Duynefontyn site.

Figure 4-44. Langebaan Formation sediments encountered (a) in borehole BH8 (Day and Ridgway, 2000) at the Duynefontyn site between 0-6 m depth, and (b) exposures of cross-bedded aeolianite south of Tieties Baai (S 32°50'30.68"; E 17°51'55.83").

The Springfontyn Formation

The Middle Pleistocene to Holocene aeolian Springfontyn Formation is characterised by unconsolidated, fine- to medium-grained, grey to pale red, structureless quartzose sand with thin peaty horizons with high organic content material (Rogers, 1980; Roberts, 2001; De Beer, et al., 2008) and reaches a maximum known thickness of 67 m near Atlantis (Rogers (1980). The formation's type area is the Springfontyn Cliffs, located northwest of Koeberg. The formation is frequently exposed at the surface unconformably blanketing weathered Malmesbury Group bedrock and forms undulating vegetated dunes in and around the Koeberg and Duyefontyn sites, as seen along the R27 road (Figure 4-45).

Figure 4-45. Vegetated dune of the Springfontyn Formation exposed along the R27 road leading to the KNPS (S 33°36'37.27"; E 18°25'13.63").

<u>Witzand Formation</u>

The uppermost exposed formation of the Sandveld Group comprises the unconsolidated, unvegetated to partially vegetated, calcareous Holocene coastal dunes that form the youngest deposits of the Sandveld Group (Rogers, 1982; Browning and Roberts, 2015). The holostratotype for the formation is located in the Duynefontyn dune plume at the top of the Springfontyn Cliff just north of Duynefontyn. The formation comprises predominantly moderately-to-well sorted, medium-to-fine grained sand. At Groot Springfontyn, the uppermost Langebaan Formation is overlain by a dark brown palaeosol with a midden containing shells of *Donax, Choromytilus* and *Patella* species. Roberts (2001) notes that the presence of bone and stone implements demonstrate a Holocene age for these deposits.

4.4.3 Structural geology

The structural geology of the Tygerberg Formation in the areas surrounding the Duynefontyn site is largely obscured by Cenozoic cover. Structural characteristics are predominantly obtained from excavations and oriented borehole cores at the Duynefontyn site (Dames and Moore, 1976, 1977), coastal outcrops (e.g., Bloubergstrand, Bokbaai) (Von Veh, 1982; Stowe, 1995; Theron et al., 1992) and inland exposures within a 40 km radius around the KNPS (De Beer et al., 2008).

Figure 4-46 shows stereonet plots depicting poles to bedding, joints and fractures, fold axes, faults, and cleavage at the Duynefontyn site and surrounding area within a 40 km radius around Duynefontyn from various authors (Dames and Moore, 1977; Von Veh, 1982; Theron et al., 1992; Stowe, 1995; De Beer et al., 2008).

- Bedding of the Tygerberg Formation at both the KNPS and Duynefontyn sites strike NNW-SSE (320°-330°) with little variation in strike (Figure 4-46a). A larger variation in strike is encountered in areas within the 40 km radius around the both sites, with bedding striking slightly more NW-SE.
- Bedding mainly dips steeply WSW between 60° and 85° as derived from bedding measurements during excavations at Koeberg, adjacent to the Duynefontyn site.

- The Tygerberg Formation is deformed in a succession of slightly inclined to tight upright folds with axial planes trending NW to NNW.
- A regional deviation fold axes of as much as 60° is observed along coastal exposures north and south of Duynefontyn, a possible consequence of polyphase folding and pitching of folds.
- The wavelengths of folds generally range from a few centimetres to ten of metres. In the Tygerberg area the half-wavelength of adjacent major synclines and anticlines varies from 0.5 to 1.5 km (Theron et al., 1992).
- Folds exibit both a 'S' and 'Z' symmetry. Folds' plunges vary considerably along axial traces and may be doubly plunging. Folds show considerable variation in symmetry especially on a small-scale within minor folds structures as observed by Von Veh (1982) at Bloubergstrand. Strata at the Duynefontyn site form part of a western limb of an NNW striking regional anticline with an almost horizontal fold axis with second order minor folds.
- Fold structures are transected by several sets of quartz-filled shear veins and open joints.

Dames and Moore (1977) identified both transcurrent and thrust faults at the Duynefontyn site (Figure 4-33). The transcurrent type faults occur as a conjugate system of vertical to subvertical strike-slip faults; a right-lateral strike-slip set with an NNE trend and a left-lateral strike-slip set with a WNW trend. These faults are of a meso-scale and generally occur in a discontinuous *en echelon* pattern with fault widths ranging from hairline to 0.5 m with common fault drag features. The faults are frequently infilled with quartz veining or breccia. Lateral offset along these faults range from a few centimetres to several metres with an unknown amount of vertical displacement. Low angle, NE and NW striking thrust faults dip between 10° and 60° with offset in the order of <10 m. Anastomosing shear zones range from 0.1-3 m in width and are associated with less competent lithologies. De Beer et al. (2008) confirmed these observations within the 40 km radius around the Duynefontyn site, denoting reverse, thrust and strike-slip faults at all scales. Sub-vertical, NNW-SSE striking slaty fracture cleavage is generally weakly developed and is rarely intense enough to obliterate bedding with quartzitic units generally not exhibiting cleavage.

Figure 4-46 show a stereonet plot for all joint measurements in these areas. Joints and fracture discontinuities are generally well developed and exhibit an array of strike orientations and dips. Stowe (1995) conducted a detailed joint analysis of the Tygerberg Formation and identified 5 joint sets: Jp, Jh, J1, J2 and J3. Joint set Jp is ubiquitous and dips steeply towards the WSW at 75-85°. The set is parallel to lithological layers and cleavage. Joint set Jh is extensional, unloading, sub-horizontal joints. J1 joints are described as right-lateral shear joints that generally dip east to ESE at 20-50°. J2 extensional cross joints strike at right angles across bedding and dip NNW at 80-90°. J3 joints strike obliquely NE and dip steeply SE. Regionally the two most prominent main sets are the sub-vertical joints (equivalent to Jp and J2) and the sub-horizontall orientated set. The main strike of joints at the Duynefontyn site is orientated ENE-WSW. Generally, joint and fracture apertures range from tight to slightly open (1 mm) to moderately open (10 – 30 mm) with wide apertures openings (> 30 mm) of 50 mm. Joint and fracture openings are either empty or filled with milky white quartz or occasionally exhibit pyrite mineralisation. Joint sets transect all other structural features. However, no joint set or fracture was found to extend into Cenozoic cover rocks.
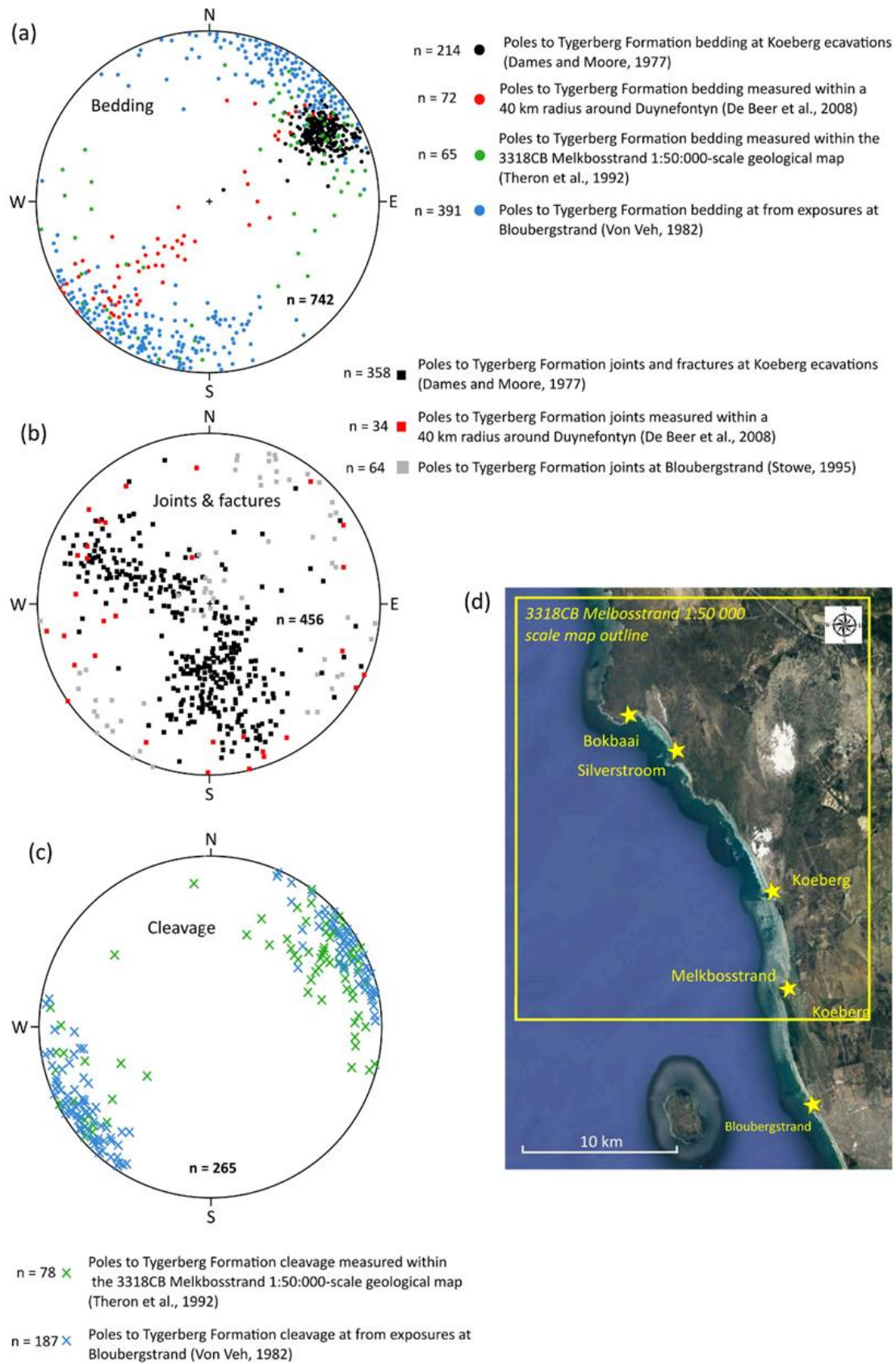
Figure 4-46. Stereonet plots depicting poles to (a) bedding, (b) joints and fractures, and (c) cleavage at the Duynefontyn site and surrounding area within a 40 km radius around the KNPS from various authors (Dames and Moore, 1977; Von Veh, 1982; Theron et al., 1992; Stowe, 1995; De Beer et al., 2008). (d) Index map showing main location from which structural readings are derived.

4.4.4 Regional erosion and Uplift Rates

There are currently two contrasting models for Cenozoic rates of land-level change and geomorphic evolution of southern Africa:

- Episodes of rapid uplift (e.g., King, 1962; Partridge and Maud, 1987).
- Slow to no uplift (e.g., Gurnis et al., 2000; Doucouré and De Wit, 2003).

Partridge and Maud (1987) proposed an episodic uplift model that invoked periods of rapid uplift and long periods of quiescence, resulting in large scale erosion and the development of extensive pediplains. The planar geomorphological features were termed 'African erosion surfaces' (Partridge & Maud, 2000; Partridge et al., 2006). Their model was based largely on field observations and interpretation since analytical tools were limited at that time. Criticism of their model is driven by lack of reliable age-constraints on erosional surfaces and uncertainty in correlating these surfaces over broad regions of the sub-continent. Doubts were also raised as to whether discrete uplift events would result in regional erosion surfaces (Brown et al., 2000; Summerfield, 1996).

More recent data-driven studies provide an alternative view of the episodic uplift model presented by Partridge and Maud (1987). Multiple authors presented evidence of slow rates of erosion and thus low rates of isostatic upliftduring the Cenozoic. Results were based on dating landscape surfaces using cosmogenic nuclides and fission track analysis (e.g., Tinker et al., 2008; Brown et al., 2002, Fleming et al., 1999). A reconstruction of the palaeotopography of the African continent also indicated that the interior topography had already been high in the Cretaceous and that modern topography did not require high uplift rates during the Cenozoic (Doucouré & de Wit, 2003). The long-term uplift (Cretaceous to Cenozoic) history of southern African was however marked by phases of uplift and inactivity (e.g., Baby et al., 2020; Marker and Holmes, 2010; Dauteuil et al., 2015; Walford and White, 2005). Along the southern coast of South Africa (or southern Cape), Tinker et al. (2008) calculated denudation of <1000 m during the Cenozoic. Throughout the Pliocene and Pleistocene, the coastal margin of the southern African Plate has been relatively tectonically stable (Roberts, 2006; Chen et al., 2014; Kounov et al., 2015).

Very slow land erosion rates of 5.4 m/My (4.4 m/My rock uplift rate) were calculated based on the [10]Be content of sand samples collected from six different river systems along southern South Africa (Bierman, 2012). Erlanger et al. (2012) inferred incision rates of less than <20 m/Ma with rock uplift rates of 9 m/My near Durban and 16 m/My within the Sundays River Valley. Linear inverse modelling of drainage networks in the Northern and Western Cape yielded average uplift rates of 11 ± 20 m for the past 15 Ma (Rudge et al., 2015). For South Africa, glacial isostatic adjustment models show only minor departures from eustacy (Raymo et al., 2011; Rovere et al., 2014) and are characterised by relatively small uncertainties under various mantle viscosity profiles used to predict glacial isostatic adjustment for Pleistocene and Pliocene time scales (Rovere et al., 2014). Uplift or subsidence during the Pleistocene and Pliocene along passive margins (Austermann et al., 2017; Moucha et al., 2008), appears to have a slight, although still uncertain effect along the western and southwest coasts of South Africa.

The Plio-Pleistocene relative sea level estimates by Hearty et al. (2020) were used to determine long term vertical tectonic uplift. Their results suggest an average, relatively low

uplift rate of 3.5-4.8 m/My during this time period for the broader west coast. This rate would have a minimal uplift effect on MIS 5e (125 ka) and MIS 11 (400 ka) (on average, <2 m). Their rate is lower than those reported by Rudge et al. (2015) for the last 13 ± 5 My from Hondeklip Bay (8 ± 3 m/My) and the 20±10 m/My for Saldanha Bay. Founded on comparison of stratigraphic, palaeontological and proxy sea level data for the Late Tertiary, Roberts (2006) suggests a 0-2 m/My tectonic uplift rate along the West Coast since the basal Pliocene (5.33 Ma). Using palaeontology and regional lithostratigraphy to link marine terraces along the west and southern coasts to the same transgressive episodes and chronologies, Roberts et al. (2006) also suggests that the slightly higher elevation (120 m) of the Alexandria and De Hoopvlei Formations (South Cape Coast) when compared to their lower West Coast counterparts (90-100 m) could indicate relative post basal Pliocene tectonism of ~20-30 m (3.75-5.62 m per My).

A regional study on marine terraces supported by geochronology investigations (Hanson et al., 2012, Bierman, 2012, Erlanger, 2012) provides evidence for relative stability along the southern Cape coast. At Thyspunt, in the Eastern Cape, burial ages derived from six paired CN samples of marine terrace bedrock and overlying beach gravels estimated an uplift rate of 5.0 ± 0.7 m/My. This is relatively similar, although slightly lower than the long-term incision rate of 6.6 ± 1.1 m/My for the Sundays River (near Gqeberha) terraces, some 120 km east of Thyspunt. These low rates compare to similar [10]Be denudation rates of between 2.3 ± 0.4 m/My and 8.8 ± 0.2 m/My for river sediment, bedrock outcrops, and fluvial gravels collected from the Cape Fold Belt in the Western Cape (Scharf, 2012).

Twenty-one (21) CN samples collected between Oyster Bay and Cape Recife yielded Middle Pleistocene ages between 250 and 450 ka, coinciding with MIS 9 and MIS 11 (Bierman, 2012). Total history ages for bedrock samples from 13 ± 1 m terraces at Oyster Bay and St. Francis Bay as well as a 12.8 m wave-cut platform at Cape Recife (southeast of Gqeberha) are correlated with MIS 11 (~400 ka) and can also be correlated with MIS 11 terraces at Mossel Bay situated at an elevation of 14 m. This would infer that uplift has been relatively uniform along most of the southern coast of South Africa during the past 400 ka (Hanson et al., 2012). The unexpectedly younger (MIS 5) ages of shorelines at ~10 m amsl at the Brazil nuclear site (West Coast) and Blind River (east coast) remain an unresolved issue but could be due to extreme wave energy or uplift of ~4 m between ~400-130 ka.

Roberts (2006) and Hanson et al. (2012) calculated uplift rates since MIS 5e (~130-117 ka) for the western and southern Cape coast. Late and possible Middle Pleistocene age data correlate with known sea levels above or near present levels, bolstering the notion of a tectonically stable coastal belt. If the maximum uplift rate of ~11.23 m/My inferred from Late Tertiary terraces (Roberts, 2006) is maintained since the inception of the Late Pleistocene (130 ka) to the present, this yields a total uplift of 1.46 m over the past ~130 ka. Ultimately this demonstrates low rates of uplift from the Middle Miocene to the Late Pleistocene, consistent with a stable intraplate setting (Roberts, 2006). Mantle convection (Burke, 1996; Simmons et al., 2007), igneous activity (Conrad & Gurnis, 2003), and flexural isostatic response (Gilchrist & Summerfield, 1990) are regarded as some of the mechanisms responsible for the above-mentioned slow uplift (de Wit, 2007).

The SSM TI Team evaluated results presented in the onshore fault report (Coppersmith et al., 2024) to better understand regional erosion rates and implications for tectonics. In order to evaluate erosion rates in the Western Cape, the authors collected eight bulk sediment samples

from different drainages in the region (Coppersmith et al., 2024). The selection of sample locations was based the position of the drainage relative to the watershed it was eroding. The watersheds eroded both the mountain ranges composed of Table Mountain Group quartzites and the rocks of the Malmesbury Group underlying the flat landscape along the western seaboard.

River sand [10]Be data showed that on average the field area is slowly eroding at rates of 5.9±0.5 m/My. These average and range of basin-scale erosion rates are fully consistent with those previously reported for similar South African landscapes. For example, Bierman et al., (2014) reported basin-scale erosion rates in the Eastern Cape region of 3.4 to 6.0 m/My for 8 basins ranging in size from 106 to 21,415 km^2. The mean rate (5.4 m/My) was similar to that reported by Scharf et al., (2012) for 10 smaller catchments underlain by quartzite (5.2 m/My).

Erosion rates of only a few metres per million years mandate that surface features are likely to persist on the landscape for many tens of thousands to hundreds of thousands of years. Such persistence suggests that vertical or horizontal surface offsets from large earthquakes (> 1m slip) should be visible if they were present on the landscape. Even fault scarps produced from more recent smaller earthquakes may remain visible in the landscape for thousands of years. The SSM TI Team thus concludes that the area-wide absence of such scarps is likely not due to erosion removing their surface expression but rather due to a lack of offset over a period of at least several hundred thousand years.

4.5   SITE GEOTECHNICAL STUDIES

The site-specific V_S characteristics are a fundamental input to the site response analysis. Estimates of V_S can come from a variety of sources, each with advantages and limitations. Several phases of geotechnical and geophysical tests were performed across the proposed Duynefontyn site (i.e., northwest of the existing KNPS). Only two V_S profiles from cross-hole testing at the KNPS were available, as documented in the Baseline report (Stamatakos et al.,2022), and these V_S profiles are compared with the more extensive Duynefontyn V_S profiles in Section 4.5.2.

Site investigations at the Duynefontyn site were performed by SRK Consulting (as reported in Du Plessis, 2021) using downhole (DH) seismic testing in 8 boreholes and multi-channel analysis of surface waves (MASW). The MASW tests performed by SRK did not develop V_S profiles deep enough into the rock, and thus are not considered in this analysis. Additional site investigations for this project included combined MASW and microtremor array measurements (MAM) performed at two locations (centred over boreholes DA and SA2) by CGS and interpreted by Prof. Brady Cox. Wireline Workshop performed PS-suspension logging in 6 CGS boreholes (DA, SA2, and ST1-ST4) that were ultimately re-interpreted by Prof. Cox and CGS personnel. The locations of the SRK boreholes, the MASW/MAM surface arrays, and the CGS boreholes are shown in Figure 4-47, and metadata is provided in Table 4-15, Table 4-16 and Table 4-17.

The two MASW/MAM testing locations were each centred on one of the two borehole array sites (i.e., the location of proposed surface and borehole ground-motion instruments at the time and completed during the timeframe of the Duynefontyn SSHAC project). These locations are called DA and SA2, which are in the southern and northern regions of the Duynefontyn site, respectively (Figure 4-47), and are northwest of the existing KNPS. Field testing took place 21-25 April 2022. Cox et al. (2024) interpreted the data from these MASW/MAM tests and produced V_S profiles down to depths of approximately 1500 m below the ground surface. Additional details of the MASW/MAM measurements and analyses are described in Section 4.6.1.

SRK performed DH testing in eight boreholes (labelled BH46-BH53) across the proposed Duynefontyn site and northwest of the existing KNPS. SRK (Du Plessis, 2021). The DH boreholes generally extended 80 m below the ground surface and up to 50 m below the base of the existing sand layer (i.e., top of rock). Drilling took place 26 May through 3 August 2021. Additional details of the DH measurements and analyses are described in Section 4.6.2.

Wireline Workshop performed PS logging to a depth of ~90-100 m (below the ground surface) at the DA and SA2 locations and shallower PS logging (~50 m below the ground surface) at four other locations (ST1-ST4) across the Duynefontyn site and northwest of the KNPS. Matamela and Cox (2024) interpreted the raw data from these measurements to obtain estimates of V_S at discrete points within the depths tested. Field testing took place in November and December 2022. Additional details of the PS logging measurements and analyses are described in Section 4.6.3.

Three different seismic techniques were used to measure V_S due to their complementary nature in terms of depth of profiling, ability to resolve thin layers and wavelength of seismic waves. Additionally, the different techniques provide confirmation of the general velocity

structure and quantification of epistemic uncertainty across different test methods. The MASW/MAM method provides the deepest profiling of V_S and represents wavelengths more similar to earthquake waves but has problems resolving thin layers at depth. Additionally, the presence of the sand above the rock at the site introduces uncertainty in the inverted V_S profiles. The DH method utilizes the same type of waves associated with the site response analyses (i.e., SH waves) and can resolve relatively thin layers, but it is difficult to measure V_S in deep layers because of attenuation of the waves from the impact source at the ground surface. The PS logging method can profile very deep and potentially can resolve very thin layers, but the wavelengths of the seismic waves are so small that the measurements show significant variability over small distances. Both the DH and PS logging methods require the selection of the wave arrival on a time record, which is subjective. The clarity of the arrivals is influenced by many factors; hence, it is important for the picks of the wave arrivals to be evaluated by experienced analysts.

The proposed plan at the Duynefontyn site prior to construction includes removal of the surficial cover strata down to the top of the shallowest rock layer (similar to the excavation performed at the KNPS before its construction). The MASW/MAM, DH, and PS logging tests were performed with the cover strata in place; thus, the resulting V_S profiles inherently include the surficial strata. Therefore, to accurately portray the V_S profile of the sites after excavation of the cover strata, the GMM TI Team modified the measured V_S profiles to exclude the influence of the cover strata, prior to using the V_S profiles in site response analyses. The appropriate method to exclude the cover strata depends on the data collection method and is discussed subsequently in each method-specific section.
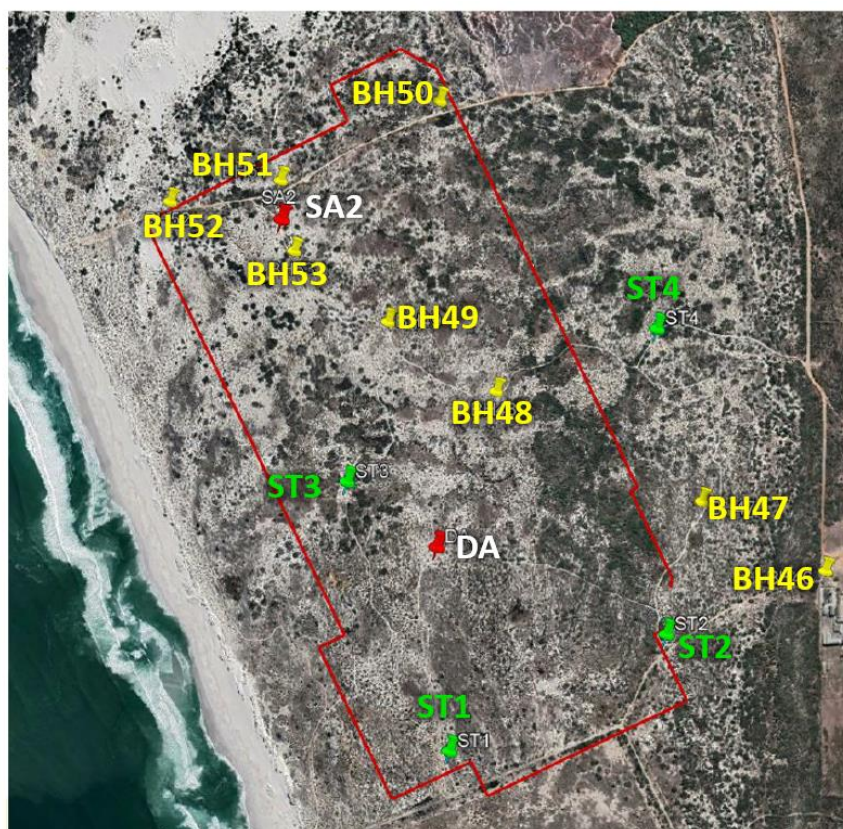

Figure 4-47. Locations of SRK boreholes (BH46 through BH53), MASW/MAM surface arrays (DA, SA2), and CGS boreholes (DA, SA2, ST1 through ST4).

Table 4-15. Metadata for MASW testing (Cox et al., 2024).

Site Name	Array Centre Latitude	Array Centre Longitude	Surface Elevation (m above msl)	Array Diameters (m)
DA	-33.664585	18.430594	17.25	50
				300
				1000
SA	-33.657416	18.426505	17.0	50
				300
				1000

Table 4-16. Metadata for the boreholes used for downhole testing by SRK.

Test Name	Latitude	Longitude	Total Borehole Depth (m)	Depth to top of rock (m)	Surface Elevation (m above msl)	Drilling Date
DH_BH46	-33.66506	18.440776	80	29.45	24.75	26 May 2021
DH_BH47	-33.66354	18.43753	81.6	31.6	27.25	7 June 2021
DH_BH48	-33.66116	18.432165	80	30.8	19.5	17 July 2021
DH_BH49	-33.65964	18.429318	80	31.05	16.75	10 July 2021
DH_BH50	-33.65484	18.430676	82.89	33.12	26	17 July 2021
DH_BH51	-33.65654	18.426492	83	32.45	20.75	3 August 2021
DH_BH52	-33.65698	18.423557	72.5	22.55	15	27 July 2021
DH_BH53	-33.65808	18.426838	80	39.0	17.25	20 July 2021

Table 4-17. Metadata for the boreholes used for PS logging.

Test Name	Latitude	Longitude	Surface Elevation (m above msl)	Maximum Depth below surface (m)
DA	-33.664586	18.430594	17.25	100 m
SA2	-33.657417	18.426506	17.0	90 m
ST1	-33.669075	18.430928	13	120 m
ST2	-33.666486	18.436633	21.25	80 m
ST3	-33.663147	18.428228	16.5	80 m
ST4	-33.659836	18.436336	26.75	80 m

4.5.1 Shear-wave velocity profiles from MASW/MAM testing

V_S profiles from MASW/MAM testing are established based on interpretation of dispersion data through inversion. The inversion process involves finding layered earth models whose theoretical dispersion curves best match the experimentally measured dispersion data. This process yields non-unique solutions, each with a "misfit" value (i.e., quality of fit between theoretical and experimental dispersion data). The range of V_S profiles that could reasonably match the dispersion data can vary widely depending on the analyst's approach and assumptions (e.g., mode interpretation, layer thicknesses). The following discussion highlights some of these assumptions, as documented by Cox et al. (2024).

It is typical to initially assume that the dispersion data from MASW/MAM can be fit using a fundamental mode (FM) interpretation. However, in cases where it is expected that there could be a mode jump (e.g., due to a strong interface between low and high V_S material) or when the dispersion data is not fit well with a FM interpretation, other higher modes may also be considered using a multi-mode (MM) interpretation. The decision to adopt a FM or MM interpretation can be guided by additional information (e.g., identifying site-specific characteristics that could explain the presence of mode jumps).

While inverting the MASW/MAM dispersion data into V_S profiles, Cox et al. (2024) assumed different mode interpretations to develop two sets of inversions. The first set of inversions assumed a FM fit to the data and the second set of inversions assumed a MM fit to the data. The FM inversions generated V_S values at depth that were greater than 4,000 m/s (capped at 4,500 m/s), particularly at the DA site. Cox et al. (2024) indicated that these velocities are unlikely for relatively shallow depths (i.e., as shallow as 100 to 500 m). The MM interpretations used the fundamental mode and first higher mode and resulted in maximum values of V_S in the profiles less than about 3,300 m/s (i.e., the maximum V_S of the Al Atik and Abrahamson (2021) V_S profile that the TI Team chose to use for the host V_S profile). However, Cox et al. (2024) indicated that the MM inversions would have likely exceeded this maximum if allowed to do so.

Cox et al. (2024) considered the MM inversions as likely better interpretations of the measured dispersion data. Strong impedance contrasts (e.g., the sand-rock interface at the Duynefontyn site) often yield mode jumps and/or superimposed modes that can be difficult to discern. However, Cox et al. (2024) provided both FM and MM results to the GMM TI Team to enable the consideration of both sets of V_S profiles and assign appropriate weights.

To capture additional epistemic uncertainty in the inversion process, Cox et al. (2024) considered a range of layering ratios (LRs) during the inversions. The LR parameter tunes the average layer thickness in a V_S profile to be thinner or thicker. For example, a higher LR will typically lead to fewer, thicker layers compared to smaller LRs. Cox et al. (2024) considered several LRs during the inversion process, but ultimately selected five LRs that yielded acceptable results: 1.5, 2.0, 3.0, 5.0, and 7.0.

Finally, Cox et al. (2024) also computed horizontal-to-vertical spectral ratios (HVSRs) to guide the inversions. HVSRs were computed for all stations used in MAM testing at the DA and SA2 sites. If he identified a well-defined peak in the HVSR, the frequency of the lowest frequency peak was used to estimate the fundamental resonant frequency of the site. This fundamental frequency is a general characteristic of the site that can be used to further refine the selection of V_S profiles in the inversion process. However, due to the strong impedance contrast between the surficial sand and the underlying rock, these HVSR peaks mainly represent only the sand-rock interface (i.e., peaks observed between 2-5 Hz in Cox et al., 2024). Because the sand will ultimately be removed from the site, the GMM TI Team did not use the HVSR data to judge the inverted V_S profiles in the rock. No lower frequency peaks in the HVSR were observed that may could have been used in the inversions to help constrain the V_S profile in rock.

The GMM TI Team received a total of 20 median V_S interpretations (each median represents 100 individual V_S profiles). The 20 median profiles were developed from combinations of 2 mode interpretations (MM and FM) and five LRs (1.5, 2.0, 3.0, 5.0, and 7.0) for each of the two MASW/MAM sites (DA and SA2). These V_S profiles from the MASW/MAM testing extend to a depth of ~1500 m below ground surface. Figure 4-48, Figure 4-49, Figure 4-50 and Figure 4-51 show the top 100 V_S profiles for the DA-FM, DA-MM, SA2-FM, and SA2-MM interpretations, respectively, as provided by Cox et al. (2024). Also shown are the theoretical dispersion curves for each V_S profile, as well as the experimental dispersion data with uncertainty bounds. When fitting the experimental dispersion data with multiple modes (e.g., Figures 4-49, 4-51), the higher frequencies are fit with the fundamental mode)i.e., lower set of curves) and the lower frequencies with the first higher mode (upper set of curves). The resolution depth (d_{res}), defined as half of the resolution wavelength ($d_{res} = \lambda_{res}/2 = 1282$ m), is highlighted in each figure. At depths greater than the resolution depth, the V_S profiles are constrained by less reliable dispersion data and should be used with caution. Although V_S values below this depth are less certain, they provide guidance that is better than blind assumptions or guesses. Figure 4-52 summarizes the standard deviation of ln V_S (σ_{lnVs}) for each set of 100 profiles for the 5 LR for the DA-FM, DA-MM, SA2-FM, and SA2-MM interpretations. The V_S datasets generally show the most variability in the top 200 m (σ_{lnVs} ~ 0.1 to 0.4), with significant less variability (σ_{lnVs} < 0.05) at depth. The small variability at depth is a result of the large phase velocity (> 3000 m/s) at low frequencies in the dispersion data and the flattening of the dispersion curve at low frequencies (e.g., below 2-3 Hz in Figure 4-48). There are instances of larger variability at depth, but only at a location of a variable

impedance contrast (e.g., between 700-1000 m depth in the MM interpretations). Additionally, the LR7.0 profiles display the smallest variability among all the LR due to the fewer layers used in the inversions. The sigma (σ_{lnVs}) reported here only represent σ_{lnVs} for the individual test locations. Thus, it is not appropriate to compare different test locations to explain the smaller σ_{lnVs} at depth. Additionally, there are some differences in the phase velocities at low frequencies at the two test locations, such that the resulting Vs at depth for the two test locations are somewhat different, particularly for the FM interpretation (Figure 4-53).

The MASW/MAM V_S profiles inherently included the surficial sand, and thus required removal of V_S values that represent the sand layers before they could be used in site response analyses. For each V_S profile, the TI Team established that any shallow layer with V_S less than 500 m/s was associated with sand and was removed. This threshold of 500 m/s was determined from the DH V_S profiles (discussed in the next section) and the associated geologic descriptions from the associated boreholes. Using this approach, the top of the rock was assigned at the top of the shallowest V_S layer with V_S greater than or equal to 500 m/s. These depths were typically about 30 m below the existing ground surface. There is uncertainty in the approach used to remove the sand from the measured V_S profiles, as well as in the V_S threshold used to identify the sand/rock interface, but alternative approaches to define the top of rock (e.g., identifying a V_S contrast) would have introduced their own uncertainties. The GMM TI Team considers the uncertainty associated with the removal of the sand from the V_S profiles relatively modest, and in a general sense the GMM TI Team assumes that it is taken into account via other components of the logic tree (i.e., alternative V_S branches, model error).

The original median V_S profiles are shown in Figure 4-53 and the modified median V_S profiles after removing the sand are shown in Figure 4-54. The V_S profiles before removing the sand (Figure 4-53) indicate that the V_S values in the top 30 m representing the sand are generally below 300 m/s, and then a significant increase in V_S occurs. However, some profiles increase to a value only slightly larger than 500 m/s (e.g., SA2-FM LR1.5) while others increase to values as large as 2500 m/s (e.g., SA2-MM LR7.0). This variability in the velocity that first exceeds 500 m/s leads to significant variability in the V_S at the top of the profiles when the sand is removed (Figure 4-54). This variability is a consequence of the approach used to define the top of rock and is discussed further in the next section.

There are several differences across the 20 median V_S profiles shown in Figure 4-54. As mentioned above, there is significant variability in the V_S at the top of the rock. Also, the V_S values at depth are smaller for the MM interpretations. Finally, the V_S profiles associated with smaller LR have more layers, which result in a more gradual increase in V_S over the top ~400 m. These differences will all contribute to the epistemic uncertainty in the SAF computed from site response analyses.
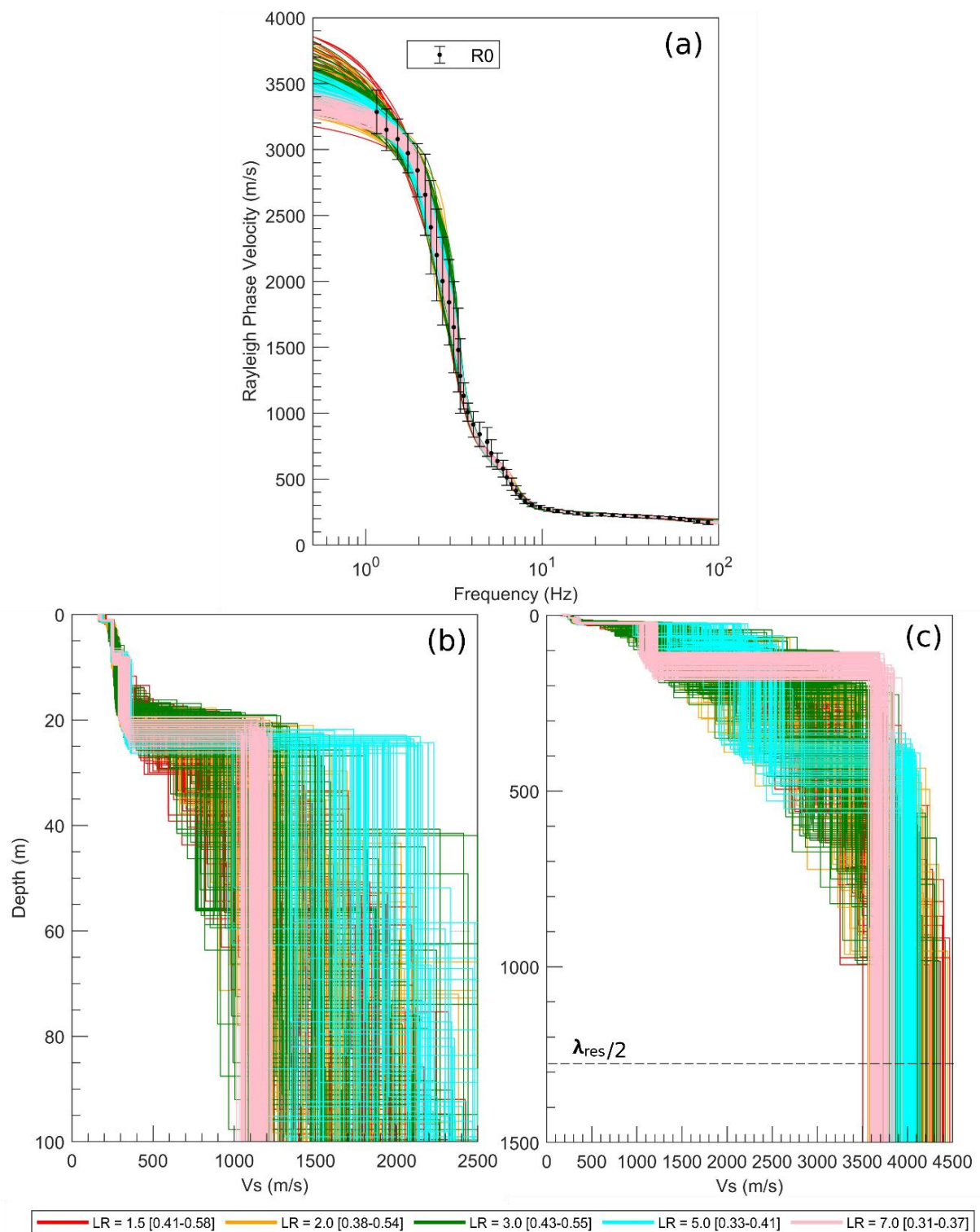
Figure 4-48. Summary of inversion results for the DA-FM inversions: a) theoretical Rayleigh dispersion curves and error bars representing experimental dispersion uncertainty bounds, b) V_S profiles in the upper 100 m, and c) V_S profiles for the entire 1500 m depth associated with the best 100 V_S profiles (based on misfit). Dispersion misfit values indicated inside square brackets.
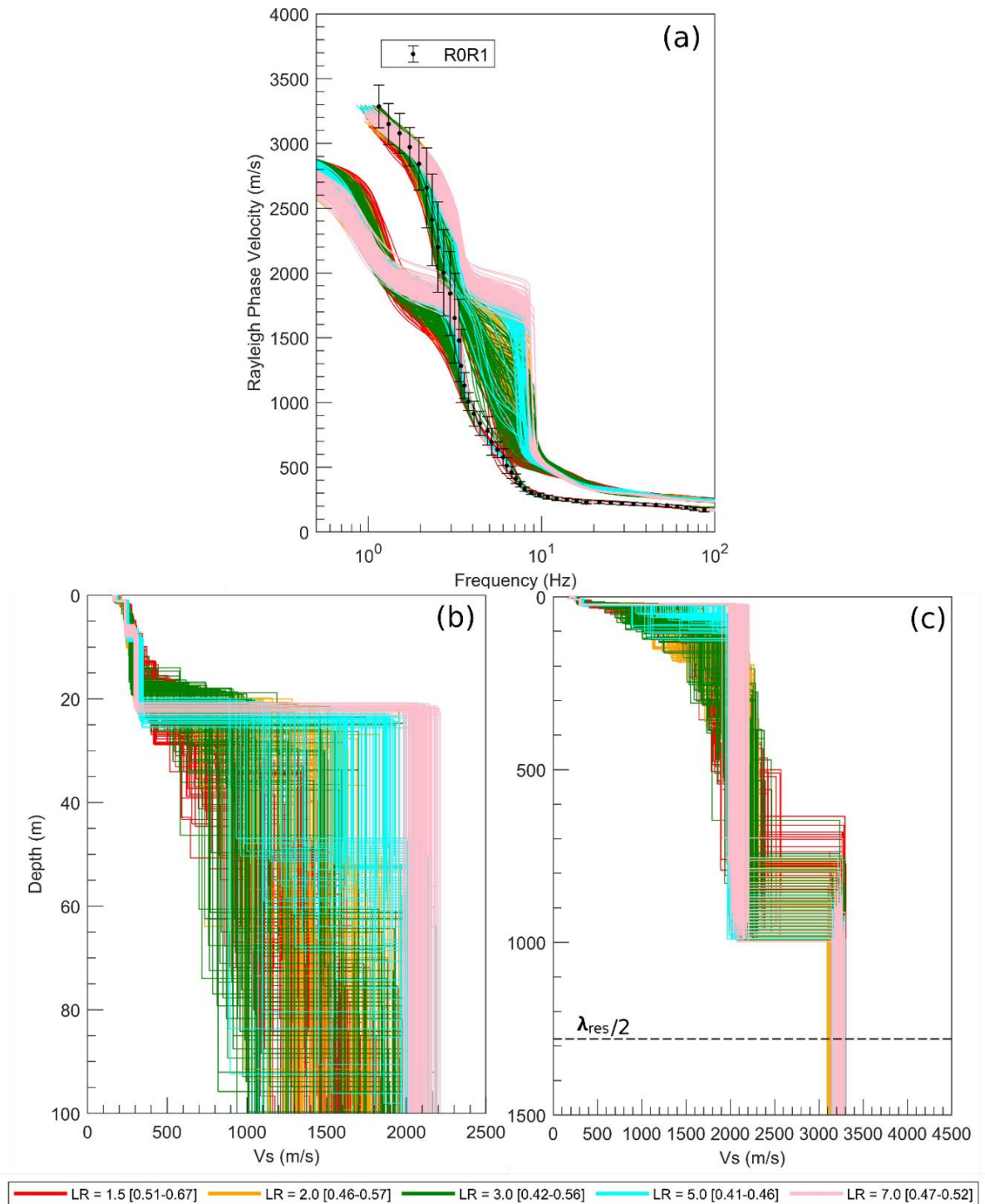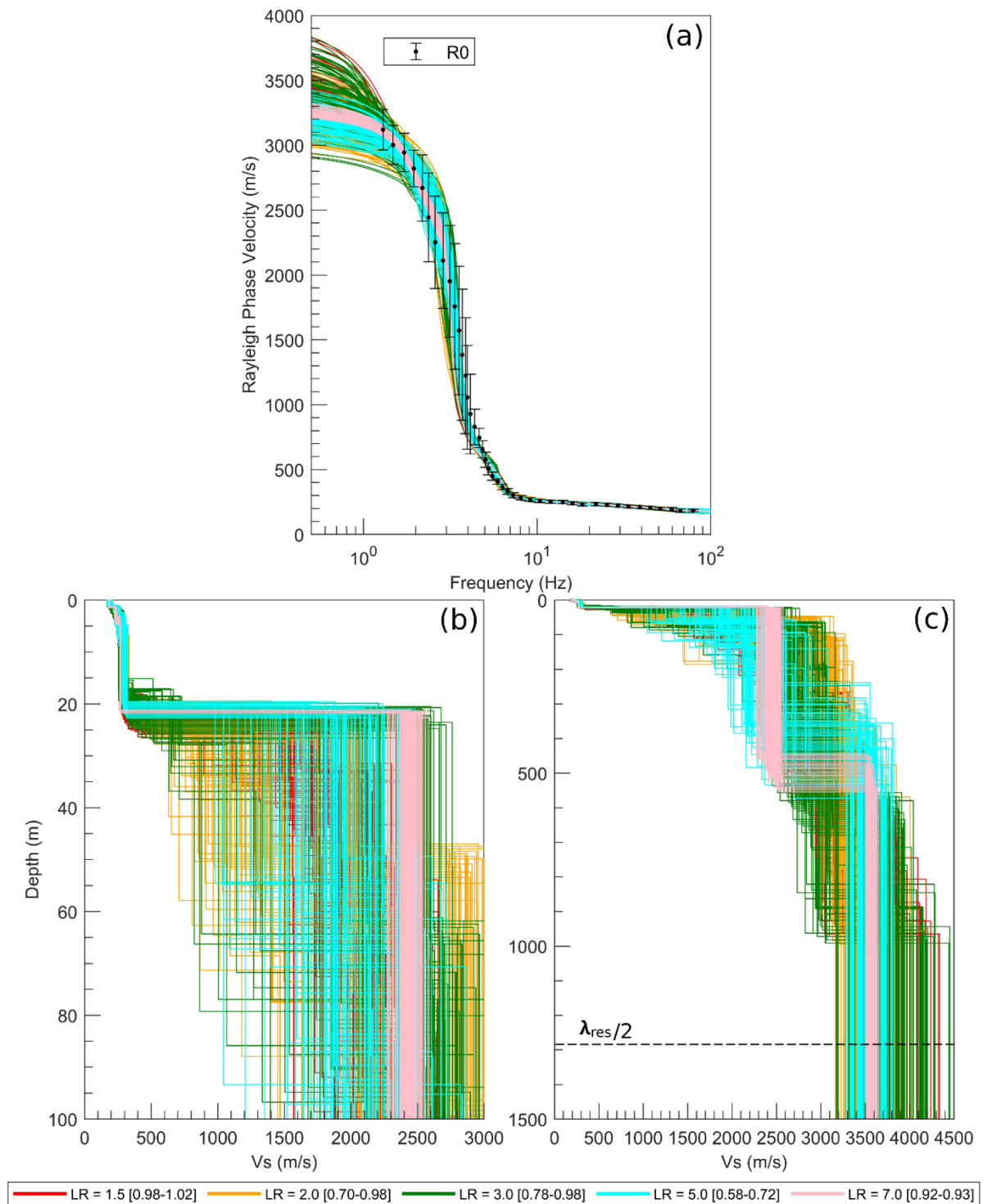
Figure 4-49. Summary of inversion results for the DA-MM inversions: a) theoretical Rayleigh dispersion curves (fundamental mode are lower set of curves, 1st higher mode is higher set of curves) and error bars representing experimental dispersion uncertainty bounds, b) Vs profiles in the upper 100 m, and c) Vs profiles for the entire 1500 m depth associated with the best 100 Vs profiles (based on misfit). Dispersion misfit values indicated inside square brackets.
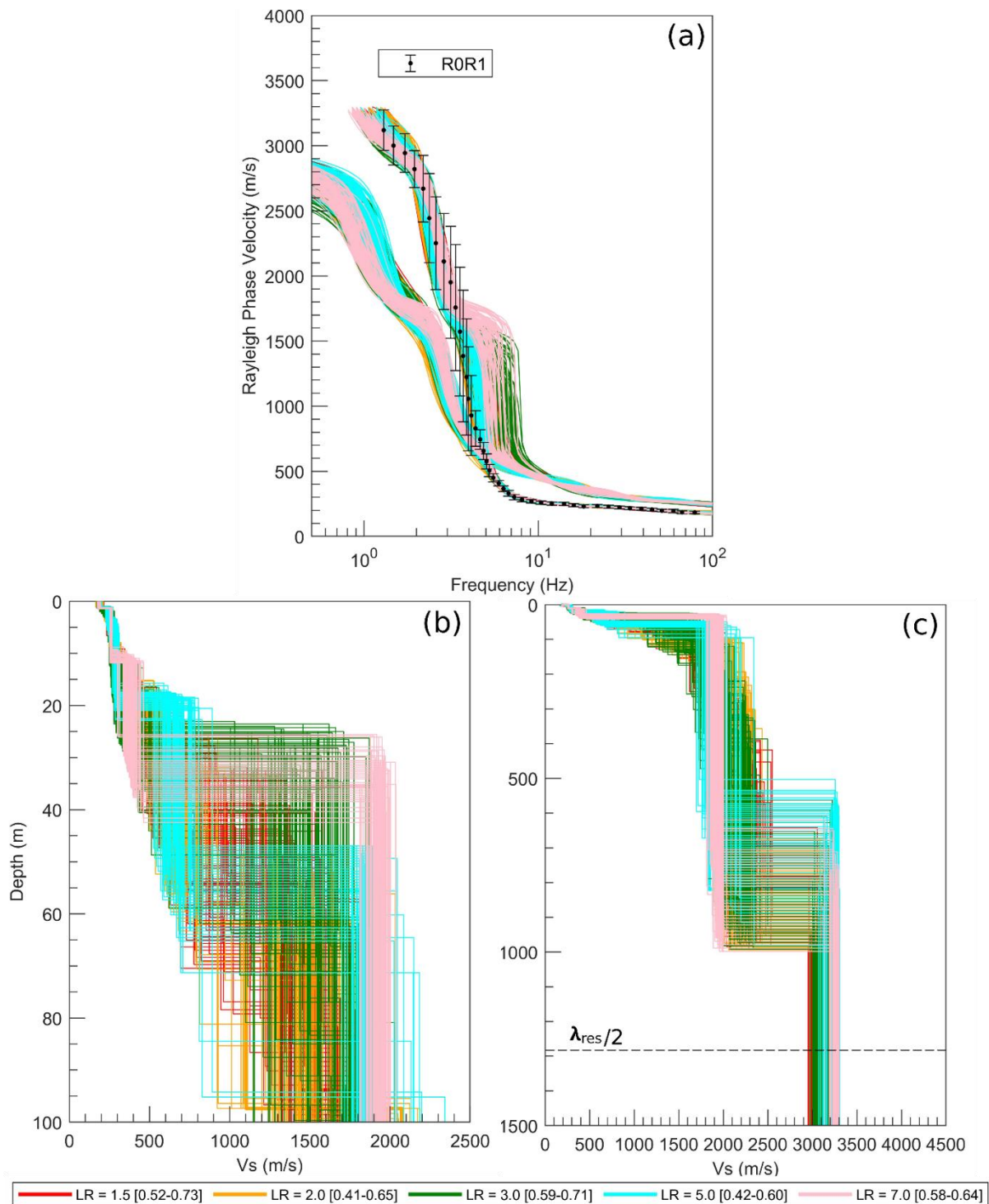
Figure 4-50. Summary of inversion results for the SA2-FM inversions: a) theoretical Rayleigh dispersion curves and error bars representing experimental dispersion uncertainty bounds, b) V_S profiles in the upper 100 m, and c) V_S profiles for the entire 1500 m depth associated with the best 100 V_S profiles (based on misfit). Dispersion misfit values indicated inside square brackets.

Figure 4-51. Summary of inversion results for the SA2-MM inversions: a) theoretical Rayleigh dispersion curves (fundamental mode are lower set of curves, 1st higher mode is higher set of curves) and error bars representing experimental dispersion uncertainty bounds, b) V_S profiles in the upper 100 m, and c) V_S profiles for the entire 1500 m depth associated with the best 100 V_S profiles (based on misfit). Dispersion misfit values indicated inside square brackets.
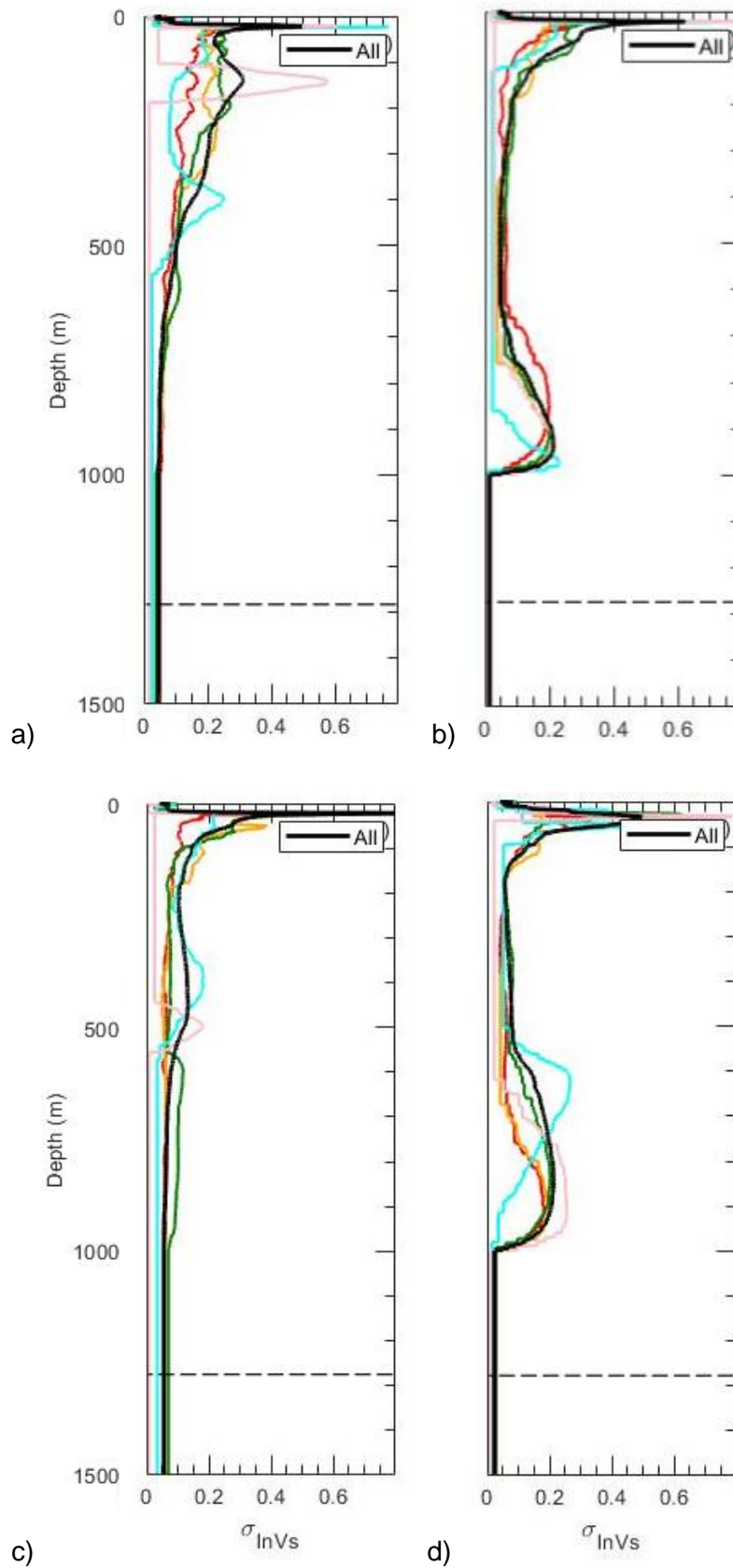
Figure 4-52. Variability in V$_S$ for the top 100 profiles from a) DA-FM, b) DA-MM, c) SA2-FM, and d) SA2-MM interpretations. LR1.5 = red, LR2.0 = yellow, LR3.0 = green, LR5.0 = cyan, LR7.0 = pink, black = average for all LRs.
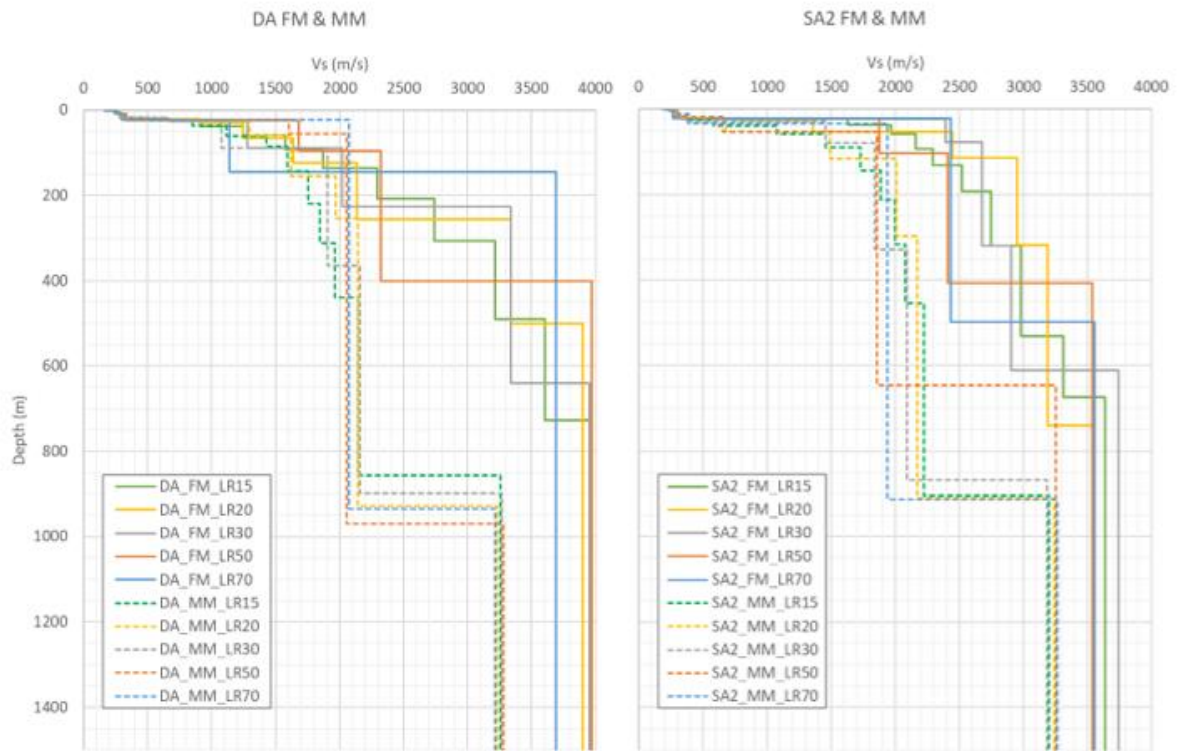
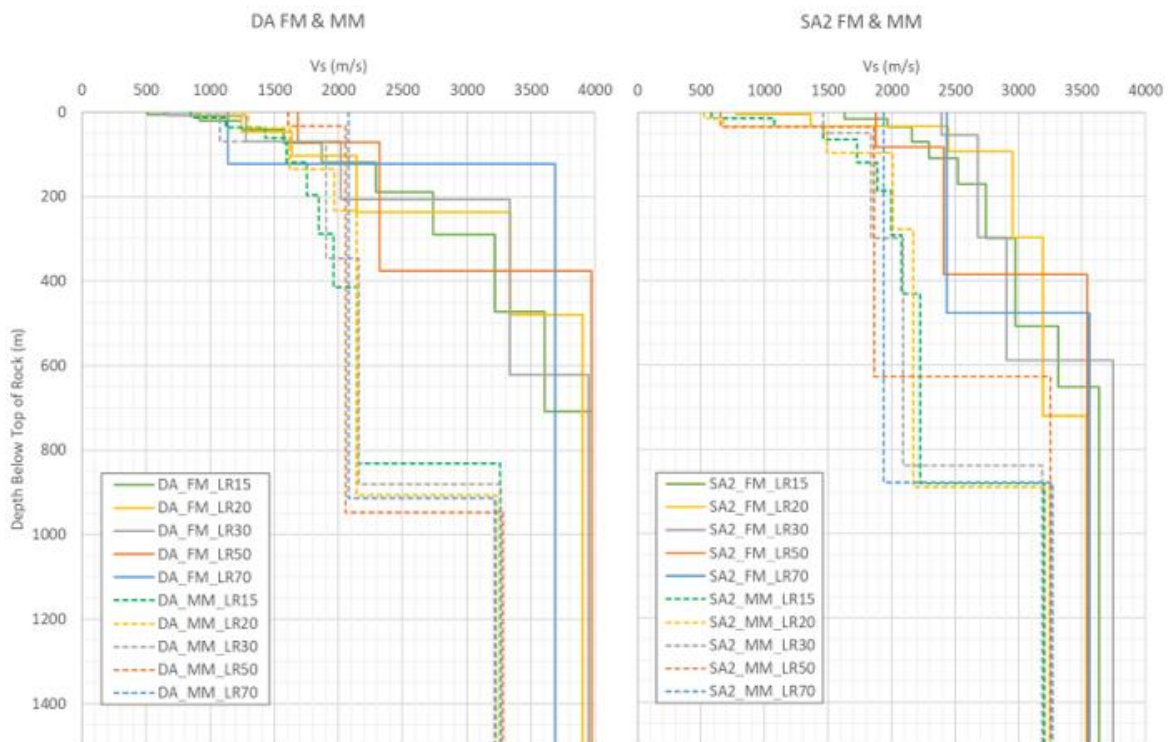**Figure 4-53. Summary of median V$_S$ profiles before surficial sand layers removed for a) DA site and b) SA2 site.**

Figure 4-54. Summary of median V$_S$ profiles after surficial sand layers removed for a) DA site and b) SA2 site.

4.5.2 Shear-wave velocity profiles from downhole testing

V_S profiles from DH testing were established based on interpretation of travel times of shear waves (Figure 4-55). There are different approaches that can be used to interpret the travel times to derive a velocity profile. Figure 4-56 shows an example plot of travel time versus depth from the SRK information in Du Plessis (2021). Du Plessis (2021) interpreted the V_S profile from these data in two ways: an interval interpretation where the difference in travel time between adjacent measurements is used to compute velocity and a layered interpretation where layers are identified in the travel time versus depth plot with constant slope (i.e., velocity). As shown in Figure 4-55, the interval interpretation generates thin layers while the layered interpretation generates thicker layers. However, the layered interpretation requires more judgment in terms of identifying the layers where the slope of the travel time curve is constant.

The GMM TI Team considered three sets of interpretations for the eight DH boreholes: (1) the SRK interval interpretation, (2) the SRK layered interpretation, and (3) a revised layered interpretation by Cox (2023, personal communication).
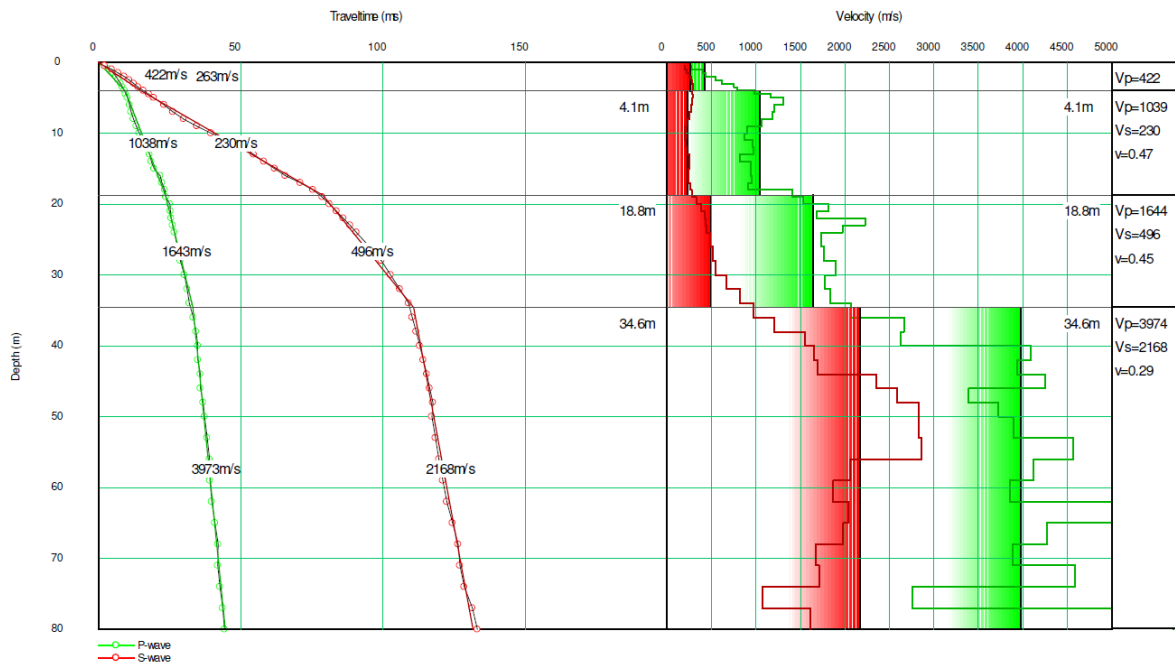

Figure 4-55. Example DH travel time data with SRK's interval (red shading) and layered (red line) V_S interpretations from SRK's BH47. SRK's P-wave interpretations shown in green.

Figure 4-56 shows the V_S profiles for each of these three interpretations. The SRK interval interpretation yields the thinnest layers, the SRK layered interpretation yields the thickest layers, and the Cox (2023) layered interpretations yield layers with thicknesses that are typically in between the two SRK interpretations. Also shown in Figure 4-56 are two cross-hole V_S profiles from the Pebble Bed Modular Reactor (PBMR) in the KNPS area as reported by Heymann and Rust (2002). The PBMR profiles were used in the Baseline report (Stamatakos et al., 2022) and are within the range of the V_S profiles from Duynefontyn. Based on this limited comparison, it can be reasonably assumed that the site amplification analyses performed for Duynefontyn approximately represent KNPS as well.
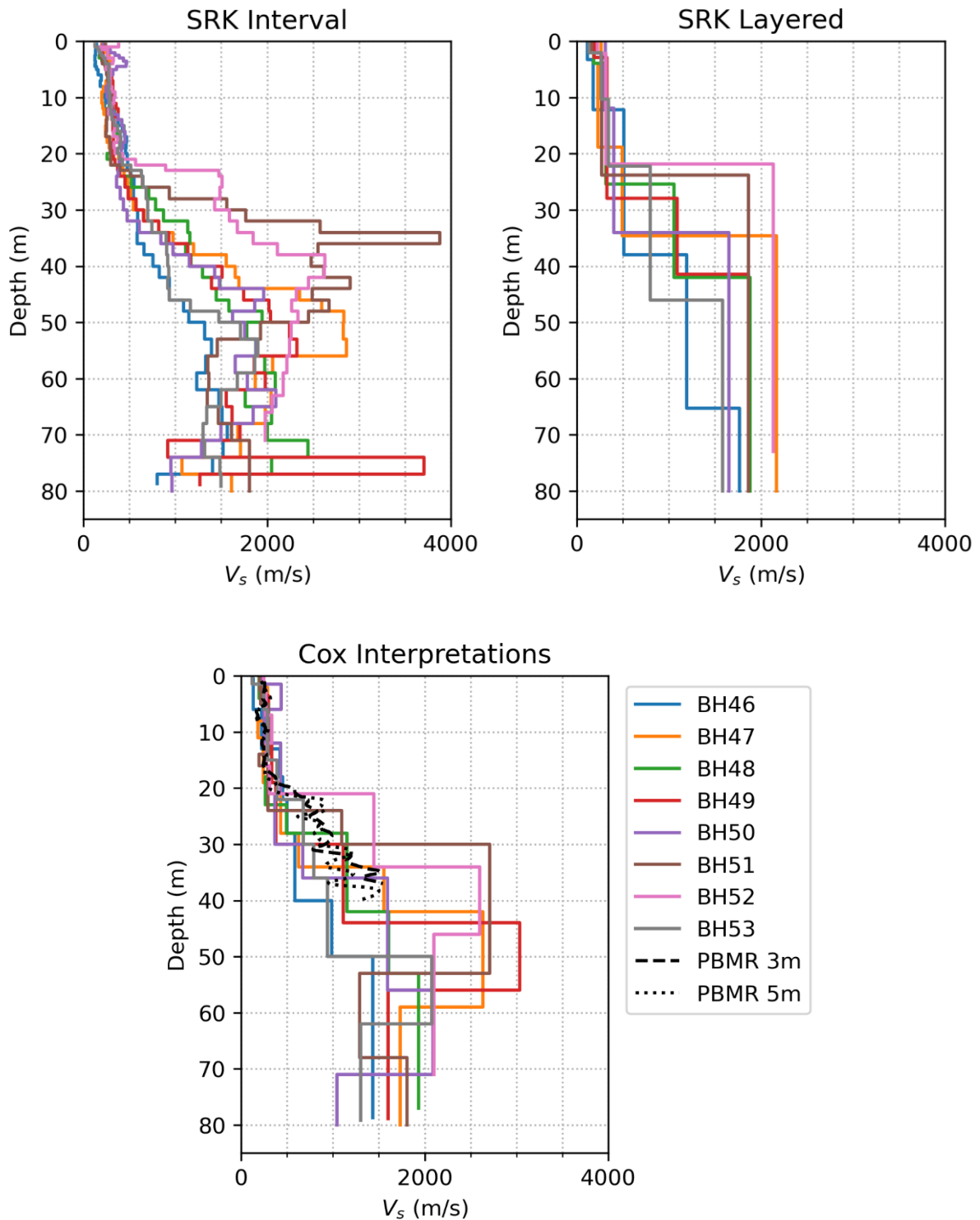
Figure 4-56. Summary of SRK interval interpretations, SRK layered interpretations, and Cox (2023) layered interpretations of V$_S$ profiles from downhole data. Two cross-hole V$_S$ profiles from the PBMR site in the KNPS area are also shown for comparison.

The V$_S$ profiles based on DH measurements include the surficial sand, and thus require removal of V$_S$ values that represent the sand layers before they are used in site response analyses. For each borehole, the TI Team used the descriptions in the boring logs to identify the top of the rock and removed V$_S$ values from the DH profiles above that depth. These

depths were typically about 30 m (see Table 4-16). V_S profiles from the DH testing extend to a depth of ~ 80 m below ground surface or ~50 m below top of rock. The modified V_S profiles (based on the Cox [2023] interpretations) after removing the sand are shown in Figure 4-57. Most of the DH V_S profiles (except BH51) show a similar trend of increasing V_S in the top 20 m followed by a reversal in the V_S (i.e., an increase in V_S followed by a decrease) between depths of about 20 and 40 m.

The depth to the top of rock for the DH measurements is explicitly known from the boring logs, yet the V_S at the top of rock in varies significantly - from a little over 500 m/s to more than 2500 m/s (Figure 4-57). This range is similar to the range obtained for the MAM/MASW profiles after removal of the sand (Figure 4-54), indicating that the approach used to remove the sand from the MASW/MAM profiles did not introduce additional variability in the V_S at the top of rock.
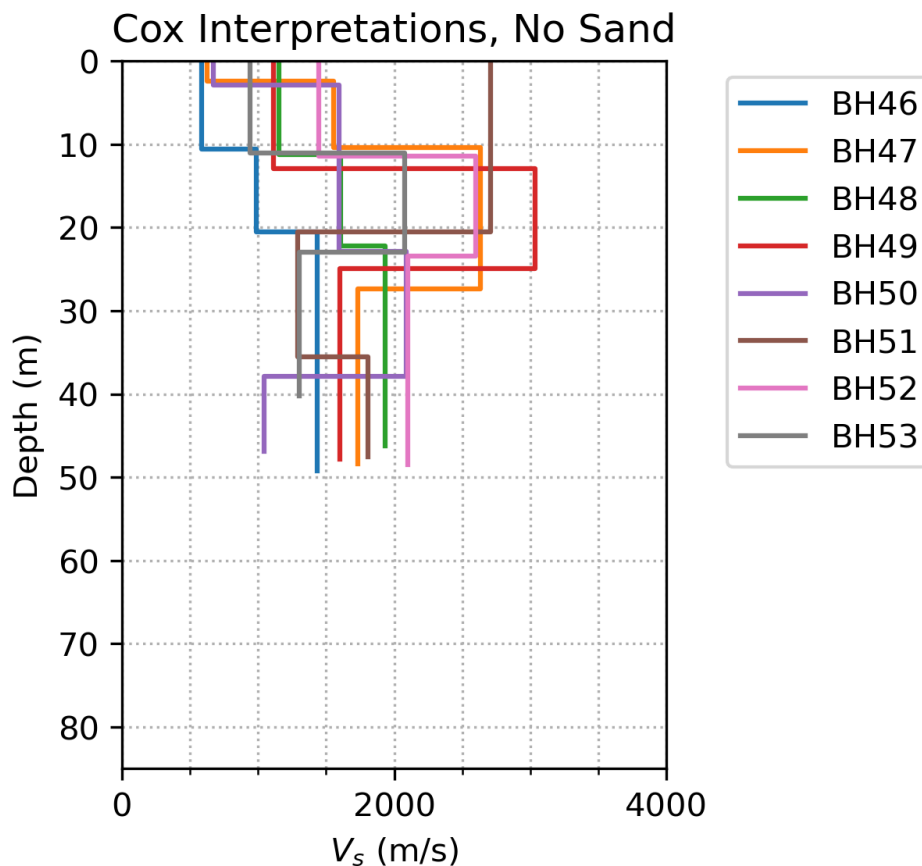

Figure 4-57. DH V_S profiles after sand removal.

4.5.3   Shear-wave velocity profiles from PS logging testing

Similar to the V_S profiles from DH data, V_S profiles from PS logging were established based on interpretation of travel times of shear waves (Matamela and Cox, 2024). As noted earlier, the selection of wave arrivals for the travel times was subjective and, thus, it was important for an experienced analyst to perform this analysis. According to Matamela and Cox (2024), the shear-wave arrival was often unclear on the PS logging time records, making the data difficult to interpret. Thus, Matamela and Cox (2024) assigned a flag to each V_S value with a code to represent data quality based on the level of difficulty in identifying the wave arrival from the time records. The code varied from 1 to 5, with Code 1 corresponding to the high quality or

confidence in the V_S data, Code 2 representing medium confidence, and Code 3 representing low confidence and ambiguous picks. Code 3 data considered two different wave arrivals for the travel-time selection because the analysts could not confidently identify a single wave arrival, and thus two V_S values are reported at each depth for Code 3. Codes 4 and 5 indicated poor waveforms that could not be interpreted with any confidence, and these were excluded from further evaluation. All V_S values were computed using interval travel times.

Figure 4-58 and Figure 4-60 show the V_S values obtained from PS logging based on the Matamela and Cox (2024) interpretations, with the data in Figure 4-58 separated by code and the same data separated by borehole in Figure 4-60. Surficial sand was removed from the V_S profiles by examining the depth to rock noted in each boring log (typically about 30 m below the ground surface), such that the data in these figures only represent the V_S in the rock. Figure 4-58 shows the Code 1 V_S data gradually increasing from about 1000 m/s to 2500 m/s in the top 50 m, with more variability in the data at depths below 50 m. The Code 2 and 3 V_S data are variable at all depths, with values varying between 1500 m/s and 3500 m/s at the same depth. The data separated based on borehole in Figure 4-60 show that the variability is distributed similarly across all the boreholes.

The V_S values identified with high confidence (Code 1) are quite reliable, but these data are relatively few in each borehole. Most of the V_S values are flagged as either medium confidence or low confidence/ambiguous (Code 2 and 3). For this reason, the PS logging data, overall, was deemed to be of low quality. Further discussion of the TI Team's evaluation of the reliability of the PS logging data and its use in developing the V_S profiles for the site response analysis is provided in Section 9.4.2.
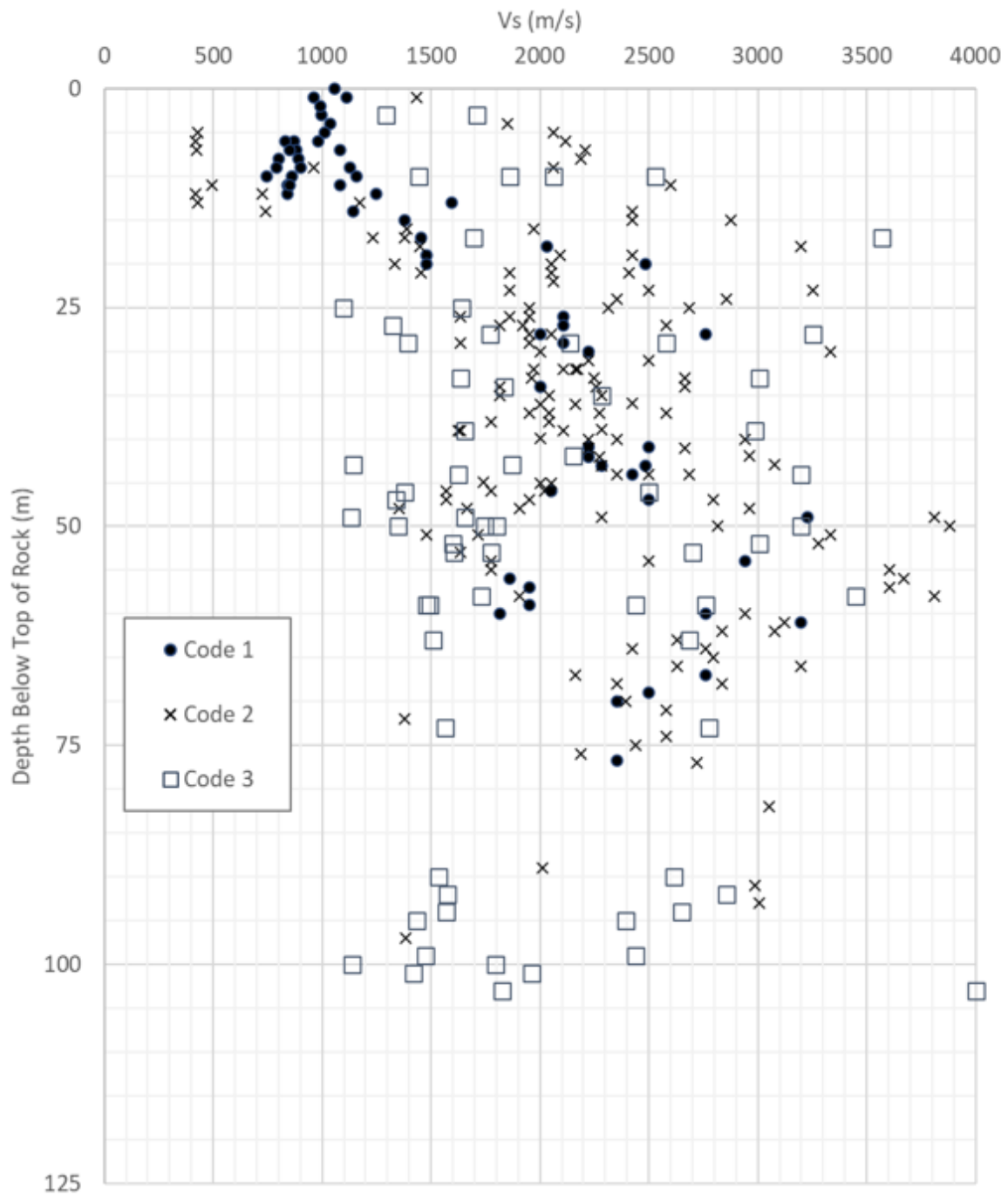
Figure 4-58. V$_S$ estimates obtained from PS logging after removing V$_S$ values in surficial sand, showing only data with highest data quality (codes 1, 2, and 3)

Figure 4-59. V$_S$ estimates (codes 1, 2, and 3) obtained from PS logging after removing V$_S$ values in surficial sand, with values shown separately for each borehole.
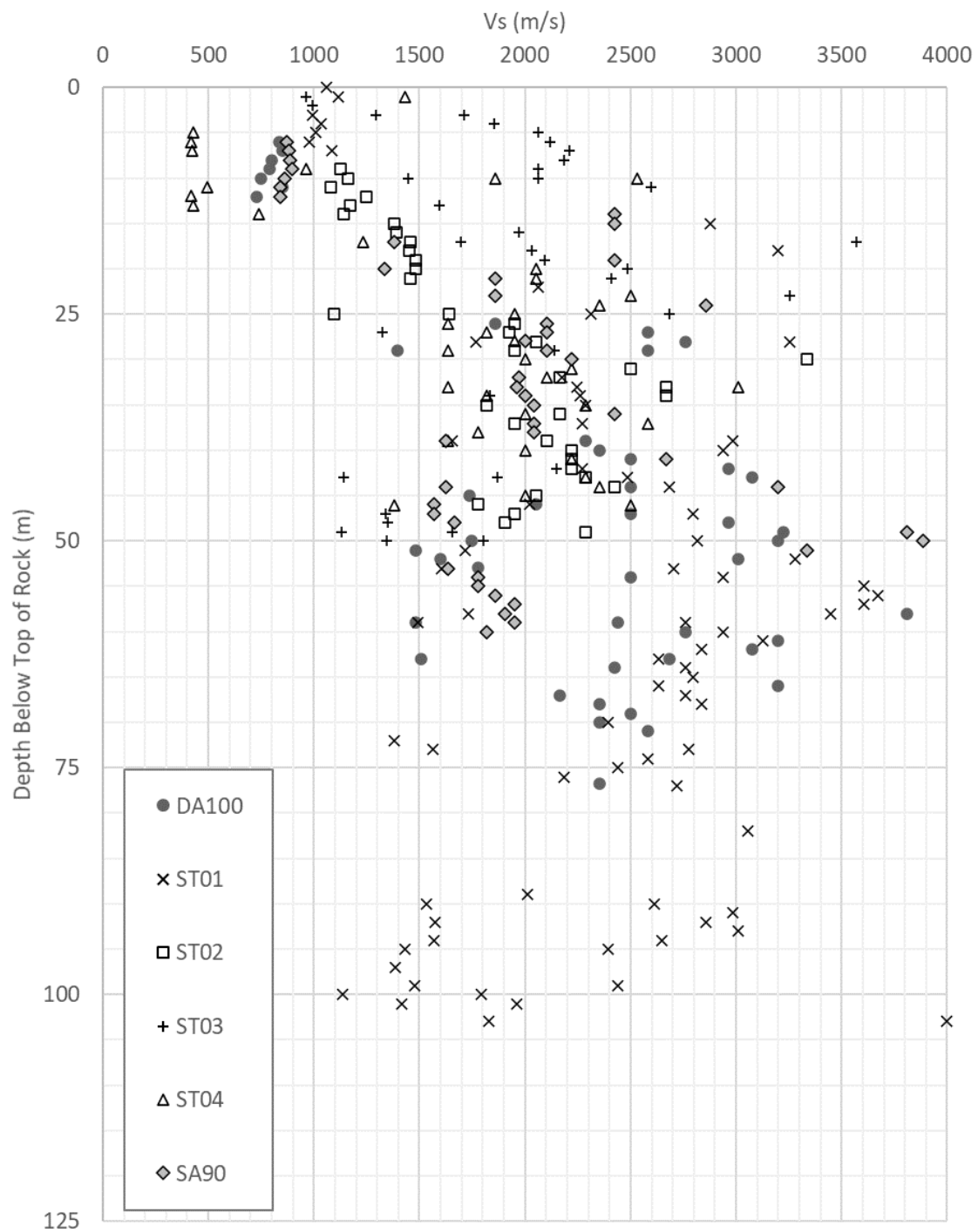
Figure 4-60. V$_S$ estimates (codes 1, 2, and 3) obtained from PS logging after removing V$_S$ values in surficial sand, with values shown separately for each borehole.
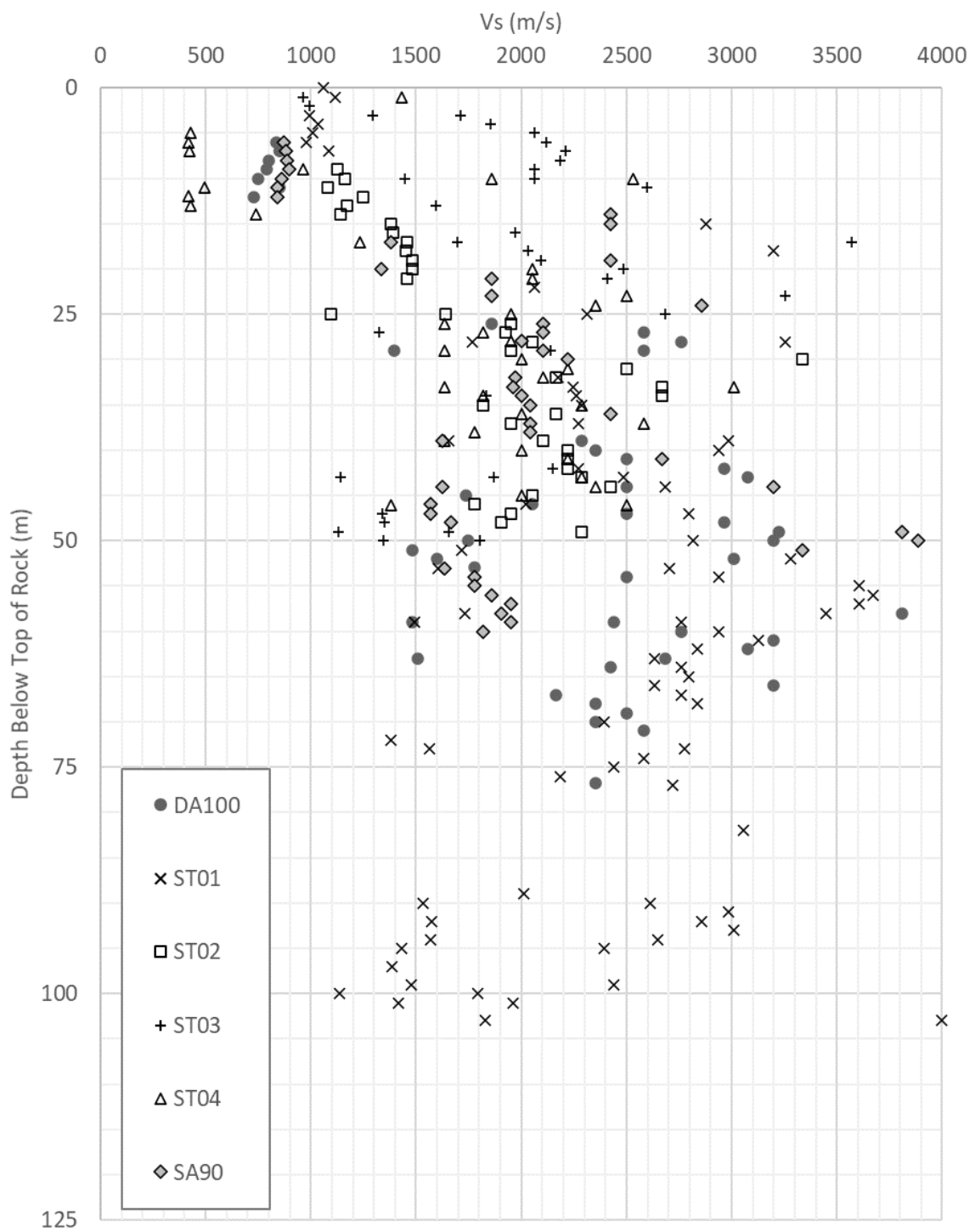
4.7   REFERENCES

Agricultural Journal (1909). Agricultural Journal, Department of Agriculture, Cape of Good Hope. Townshend, Taylor & Snashall Printers, Cape Town, South Africa XXIII.

Albini, P.; Strasser, F.O. and Flint, N.S. (2014). Earthquakes from 1820 to 1936 in Grahamstown and Surroundings (Eastern Cape Province, South Africa). Bulletin of Earthquake Engineering 12(1). 45-78.

Albini, P. and Flint, N. (2023). Investigating the Earthquake Records from 1620 to 1969 of Interest for the Duynefontyn Area, South Africa. CGS Report 2022-0127 (Rev.0). Council for Geoscience, Pretoria, South Africa, 400 pp.

Andreoli, M.; Doucoure, M.; van Bever Donker, J.; Brandt, D., and Andersen, N.J.B. (1996). Neotectonics of southern Africa - A review. Africa Geoscience Review. 3. 1-16.

Austermann, J., Mitrovica, J. X., Huybers, P., and Rovere, A. (2017). Detection of a dynamic topography signal in last interglacial sea-level records. Science Advances, 3(7).

Baby, G., Guillocheau, F., Braun, J., Robin, C., and Dall'Asta, M. (2020). Solid sedimentation rates history of the Southern African continental margins: Implications for the uplift history of the South African Plateau. Terra Nova, 32(1), 53–65.

Bakun, W.U. and Wentworth, C.M. (1997). Estimating Earthquake Location and Magnitude from Seismic Intensity Data. Bulletin of the Seismological Society of America 87(6). 1,502-1,521.

Barker, O. (2023). Koeberg - 1976 to 1978 - Memories Observations and Ideas. Prepared for the Council for Geoscience Enhanced SSHAC Level 2 PSHA, Koeberg Nuclear Power Station.

BC Hydro (2012). Probabilistic Seismic Hazard Analysis (PSHA) Model 1-4. BC Hydro Engineering Report E658. Vancouver, Canada.

Beeson, R. (1973). 3318DA Philadelphia Geological Field Map (Unpublished). 1:50,000 Scale. Council for Geoscience, Pretoria, South Africa.

Belcher R.W. and Kisters A.F.M. (2003). Lithostratigraphic correlations in the western branch of the Pan-African Saldania Belt, South Africa: The Malmesbury Group revisited. South African Journal of Geology 106. 327-342.

Bierman, P.R., (2012). Report #1 Cosmogenic Geochronology, Southern Africa Fault Corridor Investigation, Appendix B.3 in Hanson, K., Slack, C. and Coppersmith, R., Thyspunt Geological Investigations—Kango Fault Study, Council of Geoscience Report Number 2012-0035 Rev. 0, 126 pp.

Bird, P.; Ben-Avraham, Z.; Schubert, G.; Andreoli, M. and Viola, G. (2006), Patterns of stress and strain rate in southern Africa, Journal of Geophysical Research 111, B08402.

Brandt, D.; Andreoli, M.A.G. and McCarthy, T.S. (2005). The Late Mesozoic Palaeosoils and Cenozoic Fluvial Deposits at Vaalputs, Namaqualand, South Africa: Possible Depositional Mechanisms and Their Bearing on the Evolution of the Continental Margin. South Africa Journal of Geology 108. 271-284.

Broad, D.S.; Jungslager, E.H.A.; McLachlan, I.R. and Roux, J. (2006). Offshore Mesozoic Basins. In: Johnson, M.R.; Annhaeusser, C.R. and Thomas, R.J. (Eds.). The Geology of South Africa. Geological Society of South Africa, Johannesburg/Council for Geoscience, Pretoria, South Africa. 553-572.

Broad, D.S.; Jungslager, E.H.A.; McLachlan, I.R.; Roux, J. and Van der Spuy, D. (2012). South Africa's Offshore Mesozoic Basins. In: Roberts, D.G. and Bally, A.W. (Eds.). Phanerozoic Passive Margins, Cratonic Basins and Global Tectonic Maps. Elsevier, Rotterdam, Netherlands. 535-564.

Brown, R.W., Gallagher, K., Gleadow, A.J.W. and Summerfield, M.A. (2000). Morphotectonic evolution of the South Atlantic margins of Africa and South America, in M.A. Summerfield (ed.), Geomorphology and Global Tectonics, pp. 255-280, John Wiley, New York.

Brown, R.W., Summerfield, M.A. and Gleadow, A.J.W. (2002). Denudational history along a transect across the Drakensberg Escarpment of Southern Africa derived from apatite fission track thermochronology, Journal of Geophysical Research, 107, 2350

Browning, C. and Roberts, D. L. (2015). Lithostragraphy of the Witzand Formation (Sandveld Group), South Africa. South African Journal of Geology 118(3). 317-322.

Buggisch W.; Kleinschmidt G.; Krumm S. (2010). Sedimentology, geochemistry and tectonic setting of the Neoproterozoic Malmesbury Group (Tygerberg Terrane) and its relation to neighbouring terranes, Saldania Fold Belt, South Africa. Neues Jahrbuch fur Geologie und Palaontologie 257. 85-114.

Chen, F., Friedman, S., Gertler, C. G., Looney, J., O'Connell, N., Sierks, K., and Mitrovica, J. X. (2014). Refining estimates of polar ice volumes during the MIS11 interglacial using sea level records from South Africa. Journal of Climate, 27, 8740–8746.

Chisenga, C.; Van der Meijde, M.; Yan, J.; Fadel, I.; Atekwana, E.A.; Steffen, R. and Ramotoroko, C. (2020). Gravity Derived Crustal Thickness Model of Botswana: Its Implication for the Mw 6.5 April 3, 2017, Botswana Earthquake. Tectonophysics 787. 228479.

Claassen, D.; Black, D.E. and Mthembi, P. (2024). Marine Terraces Studies (DDC5 Activity). CGS Report 2022-0140. Council for Geoscience, Pretoria, South Africa.

Conrad, C.P. and Gurnis, M. (2003). Seismic Tomography, Surface Uplift, and the Breakup of Gondwanaland: Integrating Mantle Convection Backwards in Time. Geochemistry, Geophysics, Geosystems 4(3).

Coppersmith, R.; Slack, C.; Moabi, N.; Dhansay, T.; Cawthra, H.; Claassen, D. and Sethobya, M. (2024). Duynefontyn Onshore Fault Mapping Investigation, DDC6. CGS Report 2023-0001. Council for Geoscience, Pretoria, South Africa.

Cox, B.R.; Abbas, A.; Mulabisana, T.; Jele, V.; Mantsha, R.; Sethobya, M.; Sobothonma, S. and Nxantsiya, Z. (2024). Deep Shear-Wave Velocity Profiling Using MASW and MAM Surface Wave Methods: Duynefontyn Project, South Africa. CGS Report 2023-0203 (Rev.0). Council for Geoscience, Pretoria, South Africa.

Dames and Moore (1975). Foundation Report for the Koeberg Power Station, Cape Province R.S.A.. For the Electricity Supply Commission. NSIP-KBG-007669#P1-6.

Dames and Moore (1976). Geologic Report. Koeberg Power Station, Cape Province, South Africa. For the Electricity Supply Commission. Job 9629-014-45.

Dames and Moore (1977). Supplementary Geologic Report for the Koeberg Power Station, Cape Province R.S.A.. For the Electricity Supply Commission. Job 9629-026-45.

Dauteuil, O., Bessin, P., and Guillocheau, F. (2015). Topographic growth around the Orange River valley, southern Africa: A Cenozoic record of crustal deformation and climatic change. Geomorphology, 233, 5–19.

Day, P.W. and Ridgway, M. (2000). Geotechnical borehole logs at the Koeberg Site.

Day, P.W. and Ridgway, M. (2006). Geotechnical investigation for Pebble bed modular reactor, Koeberg. Jones & Wagner Consulting Civil Engineers, Report JW161/05/9978 (Rev.0), 63 pp.

Day, R.W. (1986). Magnetometric Mapping of the False Bay Dolerites. Joint Geological Survey/University of Cape Town Marine Geoscience Technical Report 16, 217-227.

De Beer, C.H. (1990). Some Aspects of the Tectonics of the Western Branch of the Cape Fold Belt. Abstract Volume. Geocongress 1990. Geological Society of South Africa, Cape Town, South Africa. 666-669.

De Beer, C.H.; Roberts, D.L.; Cole, J.; Engelbrecht, J. and Dondo, C. (2008). The Geology of the Site and Site Vicinity Areas of Koeberg, and an Update on Onland Geological Hazards. CGS Report 2008-0239. Council for Geoscience, Pretoria, South Africa.

De la Torre, C.A. and Bradley, B.A. (2023). 2D Site Response at the Proposed Duynefontyn Nuclear Power Plant Site: The Influence of Steeply Inclined Interbedded Rock Layers. Bradley Seismics. Final Report 2023/09/18.

De Wit, M. (2007). The Kalahari epeirogeny and climate change: Differentiating cause and effect from core to space, *South African Journal of Geology* 110, 367-392.

Dhansay, T.; Musekiwa, C.; Ntholi, T.; Chevallier, L.; Cole, D. and de Wit, M.J. (2017). South Africa's Geothermal Energy Hotspots Inferred from Subsurface Temperature and Geology. South African Journal of Science 113.

Doucouré, C.M. and de Wit, M.J. (2003). Old inherited origin for the present near bimodal topography of Africa. Journal of African Earth Sciences 36. 371-388.

Du Plessis, A. (2021). Multichannel Analysis of Surface Waves (MASW) and Downhole Seismic Investigation at Duynefontyn, Western Cape. Open Ground Resources Report 2758/2021.

Engelsman, B.M. (2022). Geotechnical Characterisation. In: Site Safety Report for Duynefontyn (Rev.1), Section 5.15. Eskom.

Erlanger, E.D., Granger, D.E., and Gibbon, R.J. (2012). Rock uplift rates in South Africa from isochron burial dating of fluvial and marine terraces, Geology 40, 1019-1022.

Fadel, I.; van der Meijde, M. and Paulssen, H. (2018). Crustal Structure and Dynamics of Botswana. Journal of Geophysical Research, Solid Earth 123. 10,659-10,671.

Fitzsimmons, I.C.E. (2000). A Review of Tectonic Events in the East Antarctic Shield and Their Implications for Gondwana and Earlier Supercontinents. Journal of African Earth Sciences 31. 3-23.

Fleming, A., Summerfield, M.A., Stone, J.O., Fifield, L.K. and Cresswell, R.G. (1999). Denudation rates for the southern Drakensberg Escarpment, SE Africa, derived from in-situ–produced cosmogenic (super 36) Cl: Initial results, Journal of the Geological Society of London 156, 209-212.

Flanagan, L.E. and Rosewarne, R. (2008). The Provision of Groundwater Monitoring Boreholes, Progress Report #1 (Completion of Drilling Programme). Report 378412/01F.

Frimmel H.E. (2009) Configuration of Pan-African orogenic belts in southwestern Africa. In: Gaucher C; Sial A.N; Halverson G.P.; Frimmel H.E. (eds). Neoproterozoic-Cambrian tectonics, global change and evolution: a focus on southwestern Gondwana, Vol. 16. Developments in Precambrian geology, Elsevier, 145-151.

Frimmel, H.E.; Basei, M.A.S.; Correa, V.X. and Mbangula, N. (2013). A New Lithostratigraphic Subdivision and Geodynamic Model for the Pan-African Western Saldania Belt, South Africa. Precambrian Research 231. 218-235.

Frimmel HE, Basei MAS, Gaucher C (2011). Neoproterozoic geodynamic evolution of SW Gondwana: a southern African perspective. International Journal of Earth Science 100. 323-354.

Frimmel, H.E. and Frank, W. (1998). Neoproterozoic Tectono-Thermal Evolution of the Gariep Belt and Its Basement, Namibia/South Africa. Precambrian Research 90. 1-28.

Frimmel, H.E.; Klötzli, U.S. and Siegfried, P.R. (1996). New Pb-Pb Single Zircon Age Constraints on the Timing of Neoproterozoic Glaciation and Continental Break-up in Namibia. Journal of Geology 104. 459-469.

Fynn, M. (2018). Micro-Seismic Observations in Leeu Gamka, Karoo, South Africa. MSc Thesis, University of Cape Town, South Africa.

Gardonio, B.; Jolivet, R.; Calais, E. and Leclère, H. (2018). The April 2017 Mw6.5 Botswana Earthquake: An Intraplate Event Triggered by Deep Fluids. Geophysical Research Letters 45(17). 8886–8896. 851-859.

Gasperini P.; Bernardini, F.; Valensise, G. and Boschi, E. (1999). Defining Seismogenic Sources from Historical Earthquake Felt Reports. Bulletin of the Seismological Society of America 89. 94-110.

Gaucher, C.; Frimmel, H.E. and Germs, G.J. (2009). Tectonic Events and Palaeogeographic Evolution of Southwestern Gondwana in the Neoproterozoic and Cambrian. Developments in Precambrian Geology 16. 295-316.

Gilchrist, A.R., and Summerfield, M.A. (1990). Differential denudation and flexural isostasy in formation of rifted-margin upwards, Nature 346, 739-742.

Green, R.W.E. and Bloch, S. (1971). The Ceres, South Africa, Earthquake of September 29, 1969: I. Report on Some Aftershocks. Bulletin of the Seismological Society of America 61(4). 851-859.

Gresse, P.G. (1980). Geologie van die Gebied Oos van die Soutrivier op Vel 3318AB,– Hopefield. Veld verslag van doe Geologiese Opname van Suid Afrika, 6 pp. [English translation: *Geology of the area east of the Sout River on Sheet 3318AR – Hopefield, Field Report of the Geological Survey of South Africa (Unpublished), 6 pp.*].

Gresse, P.G. and Scheepers, R. (1993). Neoproterozoic to Cambrian (Namibian) Rocks of South Africa: A Geochronological and Geotectonic Review. Journal of African Earth Sciences 16. 375-393.

Gresse P.G.; von Veh, M.W. and Frimmel, H.E. (2006). Namibian (Neoproterozoic) to Early Cambrian Successions. In: Johnson, M.R.; Anhaeusser, C.R. and Thomas, R.J. (Eds.). The Geology of South Africa. Geological Society of South Africa, Johannesburg/Council for Geoscience, Pretoria, South Africa. 395-421.

Groshong, R.H. (1989). Half-Graben Structures: Balanced Models of Extensional Fault-Bend Folds. Geological Society of America Bulletin 101(1). 96-105.

Giulio V.; Andreoli; M., Ben-Avraham; Stengel, I., Reshef, M. 2005. Offshore mud volcanoes and onland faulting in southwestern Africa: neotectonic implications and constraints on the regional stress field, Earth and Planetary Science Letters 231, 147-160.

Gurnis, M., Mitrovica, J.X., Ritsema, J. and van Heijst, H.J. (2000). Constraining mantle density structure using geological evidence of surface uplift rates: The case of the African Superplume, Geochemistry, Geophysics, Geosystems 1, Paper No. 1999GC000035.

Hälbich, I.W. (1983). A Tectonogenesis of the Cape Fold Belt (CFB). In: Sönghe, A.P.G. and Hälbich, I.W. (Eds.). Geodynamics of the Cape Fold Belt. Special Publication 12(14). Geological Society of South Africa, Johannesburg, South Africa. 165-175.

Hansma, J.; Tohver, E.; Schrank, C.; Jourdan, F. and Adams, D. (2015). The Timing of the Cape Orogeny: New 40Ar/39Ar Age Constraints on Deformation and Cooling of the Cape Fold Belt, South Africa. Gondwana Research 32.

Hanson, K.L., Coppersmith R., Glaser, L., Roberts, D.L., Claassen, D., and Black, D. (2012). Thyspunt Geological Investigations-Marine terrace studies. *Rev. 0.*, Council for Geoscience, Pretoria, Report number: 2012-0034.

Hartnady, C.J.H.; Newton, A.R. and Theron, J.N. (1974). The Stratigraphy and Structure of the Malmesbury Group in the South-Western Cape. Bulletin of the Chamber of Mines Precambrian Research Unit, University of Cape Town 15. 193-213.

Hartnady, C.J.H.; Joubert, P. and Stowe, C.W. (1985). Proterozoic Crustal Evolution of Southwestern Africa. Episodes 8. 236-244.

Hearty, P.J.; Rovere, A.; Sandstrom, M.R.; O'Leary, M.J.; Roberts, D. and Raymo, M.E. (2020). Pliocene-Pleistocene Stratigraphy and Sea-Level Estimates, Republic of South Africa with Implications for a 400 ppmv CO2 World. Paleoceanography and Paleoclimatology 35(7).

Heidbach, O.; Rajabi, M.; Cui, X.; Fuchs, B.; Müller, J.; Reinecker, K.; Reiter, M.; Tingay, F.; Wenzel, F.; Xie, M. O.; Ziegler, M.-L.; Zoback, M. D. and the WSM Team (2018). The World Stress Map, Database Release 2016: Crustal Stress Pattern Across Scales. Tectonophysics 744. 484-498.

Heidbach, O.; Rajabi, M.; Reiter, K.; Ziegler, M.O. and the WSM Team. (2016). World Stress Map Database Release 2016. GFZ Data Services.

Hendey, Q.B. (1976). The Pliocene Fossil Occurrence in 'E' Quarry, Langebaanweg, South Africa. Annals of the South African Museum 69. 215-247.

Hendey, Q.B. (1981). Palaeoecology of the Late Tertiary Fossil Occurrences in "E" Quarry, Langebaanweg, South Africa, and a Reinterpretation of Their Geological Context. Annals of the South African Museum 84. 1-104.

Hendey, Q.B. and Dingle, R.V. (1983). Onshore Sedimentary Phosphate Deposits in Southwestern Africa. Technical Report of the Joint Geological/Survey/University of Cape Town Marine Geoscience Unit 14. 27-40.

Hendey, Q. B. and Gentry, A. W. (1970). A Review of the Geology and Palaeontology of the Plio-Pleistocene Deposits at Langebaanweg, Cape Province. Annals of the South African Museum 56. 75-117.

Heymann, G. and Rust, E., (2002). Geotechnical Parameters from Seismic Cross-Hole Measurements at the PBMR Koeberg Site (Final). G. Heymann CC, ck 9868421/23 / PBMR/2933, 26 June 2002, 43 pp.

Hodge, M.S. (2013). Neotectonic Deformation Features in Plio-Pleistocene Coastal Aeolianites: Palaeoseismology and Earthquake Hazard Implications for the Southern Cape, South Africa. MSc Thesis, University of Cape Town, South Africa.

Johnson, M.R.; Anhaeusser, C.R. and Thomas, R.J. (Eds.) (2006). The Geology of South Africa. Geological Society of South Africa, Johannesburg/Council for Geoscience, Pretoria, South Africa.

Johnston, S.T. (2000). The Cape Belt and Syntaxis and the rotated Falkland Islands: dextral transpressional tectonics along the southwest margin of Gondwana. Journal of African Earth Science 31, 51-63.

Kensley, B.F. (1972). Pliocene Marine Invertebrates from Langebaanweg, Cape Province. Annals of the South African Museum 60. 173-190.

Kent, L.E. (1980). Stratigraphy of South Africa, Part 1. Lithostratigraphy of the Republic of Africa, South West Africa/Namibia, and the Republics of Bophuthatswana, Transkei and Venda. South African Committee for Stratigraphy, Geological Survey South Africa, Handbook 8.

King, L.C. (1962). The Morphology of the Earth: A Study and Synthesis of World Scenery, Oliver and Boyd, Edinburgh, 699 pp.

Kisters, A.F.M. (2022). Geology and Structure of Pan African Basement Rocks in the Western Cape. PowerPoint Presentation (DNSP-PST-117) presented at PSHA Duynefontyn Workshop 2, June 21, Stellenbosch, South Africa.

Kisters, A. and Belcher, R. (2018). The Stratigraphy and Structure of the Western Saldania Belt, South Africa and Geodynamic Implications. In: Siegesmund, S.; Basei, M.; Oyhantçabal, P.; Oriolo, S. (Eds.). Geology of Southwest Gondwana. Regional Geology Reviews. Springer, Cham, Switzerland. 387-410.

Kisters, A.F.M.; Belcher, R.W.; Armstrong, R.A.; Scheepers, R.; Rozendaal, A. and Jordaan, L.S. (2002). Timing and Kinematics of the Colenso Fault, The Early-Palaeozoic Shift from Collisional to Extensional Tectonics in the Pan-African Saldania Belt, South Africa. South African Journal of Geology 105. 257-270.

Kolawole, F.; Atekwana, E.A.; Malloy, S.; Stamps, D.S.; Grandin, R.; Abdelsalam, M.G.; Leseane, K. and Shemang, E.M. (2017). Aeromagnetic, Gravity, and Differential Interferometric Synthetic Aperture Radar Analyses Reveal the Causative Fault of the 3 April 2017 Mw 6.5 Moiyabana, Botswana, Earthquake. Geophysical Research Letters 44(17). 8,837-8,846.

Kounov, A., Niedermann, S., De Wit, M. J., Codilean, A. T., Viola, G., Andreoli, M., and Christl, M. (2015). Cosmogenic 21Ne and 10Be reveal a more than 2 Ma alluvial fan flanking the Cape Mountains, South Africa. South African Journal of Geology, 118(2), 129–144.

Kövesligethy R.D. (1906). Processing of Macroseismic Tremors. Mathematical and Natural Science Bulletin 24. 349-368.

Kuester J.A. (1809). Letter to the Church of the United Brethren, London. Periodical Accounts, 1809, Relating to the Missions of the Church of the United Brethren, Brethren's Society for the Furtherance of the Gospel, London 4. 475-476.

Kuester J.A. and I.C. Kuehnel (1809). Account of the Journey from Genadendal to Gruenekloof, Cape Town, and Back to Genadendal. Periodical Accounts, 1811, Relating to the Missions of the Church of the United Brethren, Brethren's Society for the Furtherance of the Gospel, London 5. 91-95.

Kwadiba, M.T.O.G.; Wright, C.; Kgaswane, E.M.; Simon, R.E. and Nguuri, T.K. (2003). Pn Arrivals and Lateral Variations of Moho Geometry beneath the Kaapvaal Craton. Lithos 71(2-4). 393-411.

Malservisi, R.; Hugentobler, U.; Wonnacott, R. and Hackl, M. (2013). How Rigid Is a Rigid Plate? Geodetic Constraint from the TrigNet CGPS Network, South Africa. Geophysical Journal International 192. 918-928.

Mandl, G. (1988). Mechanics of Tectonic Faulting. Elsevier, Amsterdam, Netherlands. 407.

Manzunzu, B.; Midzi, V.; Durrheim, R.; Pule, T. and Flint, N. (2023). Quantitative Evaluation of Source Parameters of Historical Earthquakes in Southern Africa. Journal of African Earth Sciences 199. 104833.

Marimira, K.; Manzunzu, B.; Shumba, B.T.; Midzi, V. and Saunders, I. (2021). Aftershock Sequence of 22 September 2016, Manica–Zinave Earthquake (Mw5.6), Mozambique. Journal of African Earth Sciences 177.

Marker, M. E., and Holmes, P. J. (2010). The geomorphology of the Coastal Platform in the southern Cape. South African Geographical Journal, 92(2), 105–116.

Markwick, P.J.; Paton, D.A. and Mortimer, E.J. (2021). Reclus, a New Database for Investigating the Tectonics of the Earth: An Example from the East African Margin and Hinterland. Geochemistry, Geophysics, Geosystems 22(11).

Matamela, J. and Cox, B.R. 2024. PS Logging in support of Probabilistic Seismic Hazard Analyses for Duynefontyn. CGS Report 2023-0185, Council for Geoscience, Pretoria, South Africa.

McClay, K.R. (1992). Glossary of Thrust Tectonic Terms, Thrust Tectonics. Springer. 419-433.

McClay, K. and Bonora, M. (2001). Analog Models of Restraining Stepovers in Strike-Slip Fault Systems. AAPG Bulletin 85(2). 233-260.

McFarland, J., Morris, A.P. and Ferrill, D.A. (2012). Stress Inversion Using Slip Tendency. Computers and Geosciences 41. 40-46.

McMillan, I.K.; Brink, G.I.; Broad, D.S. and Maier, J.J. (1997). Late Mesozoic Sedimentary Basins off the South Coast of South Africa. In: Selley, R.C. (Ed.). African Basins 3 in Sedimentary Basins of the World series. Elsevier, Amsterdam. 319-376.

Meert, J. and Lieberman, B. (2008). The Neoproterozoic Assembly of Gondwana and Its Relationship to the Ediacaran-Cambrian Radiation. Gondwana Research 14 (1/2), 5-21.

Meert, J. and Van der Voo, R. (1997). The Assembly of Gondwana 800-550 Ma. Journal of Geodynamics 23. 223-235.

Midzi, V.; Saunders, I.; Manzunzu, B.; Kwadiba, M.T.; Jele, V.; Mantsha, R.; Marimira, K.T.; Mulabisana, T.F.; Ntibinyane, O.; Pule, T.; Rathod, G.W.; Sitali, M.; Tabane, L.; van Aswegen, G. and Zulu, B.S. (2018). The 03 April 2017 Botswana M6.5 Earthquake: Preliminary Results. Journal of African Earth Sciences 143. 187-194.

Miller, R. McG. (1983). The Pan-African Damara Orogen of South West Africa/Namibia. Special Publication Geological Society of South Africa 11. 431-515.

Mitchell, C.; Taylor, G.K.; Cox, K.G. and Shaw, J. (1986). Are the Falkland Islands a rotated microplate? Nature 319, 131-134.

Moorkamp, M.; Fishwick, S.; Walker, R.J. and Jones, A.G. (2019). Geophysical Evidence for Crustal and Mantle Weak Zones Controlling Intra-Plate Seismicity - The 2017 Botswana Earthquake Sequence. Earth and Planetary Science Letters 506. 175-183.

Morris, A.P.; Ferrill, D.A. and Henderson, D.B. (1996). Slip Tendency Analysis and Fault Reactivation. Geology 24. 275-278.

Morris, A.P.; Ferrill, D.A. and McFarland, J.M. (2013). Geological Stress Inversion Using Fault Displacement and Slip Tendency. United States Patent # US 8,589,080 B2. November 19.

Morris, A.P.; Ferrill, D.A. and McGinnis, R.N. (2016). Using Fault Displacement and Slip Tendency to Estimate Stress States. Journal of Structural Geology 83. 60-72.

Moucha, R., Forte, A. M., Mitrovica, J. X., Rowley, D. B., and Quéré, S. (2008). Dynamic topography and long-term sea-level variations: There is no such thing as a stable continental platform. Earth and Planetary Science Letters, 271(1-4), 101–108.

Mulabisana, T.; Meghraoui, M.; Midzi, V.; Saleh, M.; Ntibinyane, O.; Kwadiba, T.; Manzunzu, B.; Seiphemo, O.; Pule, T. and Saunders. I. (2021). Seismotectonic Analysis of the 2017 Moiyabana Earthquake (MW 6.5, Botswana), Insights from Field Investigations, Aftershock and InSAR Studies. Journal of African Earth Sciences 182. 104297.

Murray, E.C. and Saayman, I. (2000). Geohydrological Investigation for Pebble Bed Modular Reactor Project, Koeberg Nuclear Power Station. CSIR Report ENV/S-C 2000-084.

Musson, R.M.W. (2009). MEEP 2.0 User Guide. Earth Hazards and Systems Programme Open Report OR/09/045, British Geological Survey.

Musson, R.M.W. and Jiménez, M.J. (2008). Macroseismic Estimation of Earthquake Parameters. NERIES Technical Report NA4-D3.

Pacific Northwest National Laboratory (PNNL) (2014). Hanford Sitewide Probabilistic Seismic Hazard Analysis. PNNL-23361. Pacific Northwest National Laboratory. Richland, Washington, USA.

Partridge, T.C., Botha, G.A., and Haddon, I.G. (2006). Cenozoic deposits of the interior. In: Johnson, M.R., Anhaeusser, C.R. and Thomas, R.J. (eds.), Geology of South Africa,

Geological Society of South Africa, Johannesburg/Council for Geoscience, Pretoria, pp. 585-604.

Partridge, T.C. and Maud, R.R. (1987). Geomorphic evolution of southern Africa since the Mesozoic, South African Journal of Geology 90 (2), 179 208.

Partridge, T.C., and Maud, R.R. (2000). Macroscale geomorphic evolution of southern Africa, in The Cenozoic of Southern Africa, Eds., T. C. Partridge and R. R. Maud, Oxford Univ. Press, New York, pp. 3-18.

Paton, D.A. (2022). Can (Should?) Thick/Thin Skinned Tectonics Concepts Be Applied to Understanding the Western Cape. PowerPoint Presentation (DNSP-PST-130) presented at PSHA Duynefontyn Workshop 2, 21 June 2022, Stellenbosch, South Africa.

Paton, D.A.; Macdonald, D. and Underhill, J.R. (2006). Applicability of Thin- or Thick-Skinned Structural Models in a Region of Multiple Inversion Episodes: Southern South Africa. Journal of Structural Geology 28. 1933-1947.

Paton, D.A.; Mortimer, E.J.; Markwick, P.J.; Khan, J.; Davids; A.; Tshikovhi, R. and Van der Spuy, D. (2022). Coeval development of extensional and contractional features along transform margins: insights from the Diaz Marginal Ridge Geological Society, London, Special Publications 524, 307-325.

Peruzza, L. (1992). Procedure of Macroseismic Epicentre Evaluation for Seismic Hazard Purposes. Proceedings of XXIII General Assembly of the ESC. 434-437.

Raymo, M. E., Mitrovica, J. X., O'Leary, M. J., DeConto, R. M., and Hearty, P. J. (2011). Departures from eustasy in Pliocene Sea-level records. Nature Geoscience, 4(5), 328–332.

Reid, D.L.; Erlank, A.J. and Rex, D.C. (1991). Age and Correlation of the False Bay Dolerite Dike Swarm, South-Western Cape, Cape Province. South African Journal of Geology 94(2/3). 155-158.

Richter, C.F. (1958). Modified Mercalli Scale Restated. In: Elementary Seismology. W.H. Freeman and Company, San Francisco and London. 136-139.

Roberts, D.L. (2001). The Geology of Melkbosstrand and Environs. Explanation Sheet 3318CB Melkbosstrand. 1:50,000 scale. Council for Geoscience, Pretoria, South Africa.

Roberts, D.L. (2002). Sheet 3318CB Melkbosstrand. 1:50,000 scale geological map series, Council for Geoscience, Pretoria.

Roberts, D.L. (2006). Dating and Preliminary Correlation of Raised Marine and Estuarine Terraces on the Western and Southern Coasts of South Africa, Final Report. CGS Report 2006-0186 (Rev. 0). Eskom NSIP-SHA-018230#P1-206. Council for Geoscience, Pretoria, South Africa.

Roberts, D.L. and Berger, L. (1997). Last Interglacial c.117 kyr Human Footprints, South Africa. South Africa Journal of Science 93. 349-350.

Roberts, D.L. and Siegfried, H.P. (2014). The Geology of the Saldanha, Vredenberg and Velddrif Environs. Geological Map Explanation. Council for Geoscience, Pretoria, South Africa.

Roberts, D.L.; Botha, G.S.; Maud, R.R. and Pether, J. (2006). Coastal Cenozoic Deposits. In: Johnson, M.R.; Anhaeusser, C.R. and Thomas, R.J. (Eds.). The Geology of South Africa. Geological Society of South Africa, Johannesburg/Council for Geoscience, Pretoria, South Africa. 605-628.

Roberts, D.L.; Matthews, T.; Herries, A.I.R.; Boulter, C.; Scott, L.; Dondo, C.; Mthembi, P.; Browning, C.; Smith, R.M.H.; Haarhoff, P. and Bateman, M.D. (2011). Regional and Global Context of the Late Cenozoic Langebaanweg (LBW) Paleontological Site, West Coast of South Africa. Earth-Science Reviews 106. 191-214.

Roberts, D.L.; Cawthra, H.C. and Musekiwa, C. (2013). Dynamics of Late Cenozoic Aeolian Deposition along the South African Coast: A Record of Evolving Climate and Ecosystems. Geological Society, London, Special Publications 388. 353-387.

Rogers, J. (1979). The Sedimentary Succession at the Koeberg Nuclear Power Station, Melkbosstrand. Extended Abstracts. Geocongress 1979, Geological Society of South Africa, Part 1. 310-322.

Rogers, J. (1980). First Report on the Cenozoic Sediments between Cape Town and Eland's Bay. Geological Survey of South Africa Report 1980-136.

Rogers, J. (1982). Lithostratigraphy of Cenozoic Sediments between Cape Town and Eland's Bay. Palaeoecology of Africa 15. 121-137.

Rogers, J. (1983). Lithostratigraphy of Cenozoic Sediments on the Coastal Plain between Cape Town and Saldanha. Technical Report of the Joint Geological Survey/University of Cape Town Marine Geoscience Unit 14. 87-103.

Rogers, J.; Pether, J.; Molyneux, G.; Genis, J.L.V.; Kilham, J.L.C.; Cooper, G. and Corbeti, I.B. (1990). Guidebook. Geocongress 1990, Geological Society of South Africa.

Rovere, A., Raymo, M. E., Mitrovica, J. X., Hearty, P. J., O'Leary, M. J., and Inglis, J. D. (2014). The mid-Pliocene Sea-level conundrum: Glacial isostasy, eustasy and dynamic topography. Earth and Planetary Science Letters, 387, 27–33.

Rowe, C.D.; Backeberg, N.R.; Van Rensburg, T.; Maclennan, S.A.; Faber, C.; Curtis, C. and Viglietti, P.A. (2010). Structural geology of Robben Island: implications for the tectonic environment of Saldanian deformation. South African Journal of Geology 113(1). 57-72.

Rozendaal, A.; Gresse, P.G.; Scheepers, R. and Le Roux, J.P. (1999). Neoproterozoic to Early Cambrian Crustal Evolution of the Pan-African Saldania Belt, South Africa. Precambrian Research 97. 303-323.

Rudge, J.F., Roberts G.G., and White, N.J. (2015). Uplift histories of Africa and Australia from linear inverse modeling of drainage inventories. Journal of Geophysical Research: Earth Surface, Vol. 120, (5), 894-914.

Scharf, T. (2012). Denudation rates and geomorphic evolution of the Cape Mountains, determined by the analysis of in situ-produced cosmogenic 10Be. Unpublished MSc., Nelson Mandela Metropolitan University, pp. 254.

Scheepers, R. (1995). Geology and Petrogenesis of the Late-Precambrian S-, I-, and A-type Granitoids in the Saldania Belt, Western Cape Province, South Africa. Journal of African Earth Science 21. 35-58.

Scheepers, R.; Schoch, A.E.; Johnson, M.R.; Anhaeusser, C.R.; Thomas, R.J. (2006). The Cape Granite Suite. The Geology of South Africa. Geological Society of South Africa, Johannesburg, South Africa. 421-432.

Shumba, B.T.; Midzi, V.; Manzunzu, B.; Ottemöller, L.; Marimira, K.T. (2020). Source Parameters of the Moderate Mozambique–Zimbabwe Border Earthquake on 22 December 2018. Journal of African Earth Sciences 166. 103829.

Siegfried, H.P. (2008a). 3318AC Yzerfontein and 3318AD Darling Geological Field Maps (Unpublished). 1:50,000 Scale. Council for Geoscience, Pretoria, South Africa.

Siegfried, H.P. (2008b). 3318DB Riebeek-kasteel Geological Field Map (Unpublished). 1:50,000 scale. Council for Geoscience, Pretoria, South Africa.

Söhnge, A.P.G. and Hälbich, I.W. (1983). Geodynamics of the Cape Fold Belt. Special Publication of the Geological Society of South Africa 12.

SRK (2008a). Eskom, Duynefontyn Geotechnical Characterization, Borehole Logs.

SRK (2008b). Eskom, Duynefontyn Site Geohydrology, Exploration Borehole Data and Logs.

SRK (2021). Eskom, Geotechnical Investigation, Borehole Data and Logs.

Stacey, T.R. and Wesseloo, J. (1998). Evaluation and Upgrading of Records of Stress Measurement Data in the Mining Industry. SRK Consulting Report GAP 511b. Safety in Mines Research Advisory Committee.

Stamatakos, J.; Watson-Lamprey, J.; Cawthra, H.C.; Claassen, D.; Coppersmith, R.; Johnson, C.; Largent, M.; Manzunzu, B.; Midzi, V.; Mulabisana, T.; Murphy, D.; Rathje, E.; Wooddell, K. (2022). Baseline PSHA for the Duynefontyn Site and the Koeberg Nuclear Power Station. CGS Report 2022-0009 (Rev. 1). Council for Geoscience, Pretoria, South Africa.

Stowe, C.W. (1995). Characteristics of Jointing in the Malmesbury Group, Harbour Area, Cape Town. South African Journal of Geology 98(2). 224-231.

Strasser, F.O.; Albini, P.; Flint, N.S.; Beauval, C. (2015). Twentieth Century Seismicity of the Koffiefontein Region (Free State, South Africa): Consistent Determination of Earthquake Catalogue Parameters from Mixed Data Types. Journal of Seismology 19(4). 915-934.

Summerfield, M.A. (1996). Tectonics, geology, and long-term landscape development. In Adams, W.M., Goudie, A.S. and Orne, A.R. (eds.): The Physical Geography of Africa, Oxford University Press, New York, 17 pp.

Tack, L.; Wingate, M.T.D.; De Waele, B.; Meert, J.; Belousova, E.; Griffin, B.; Tahon, A. and Fernandez-Alonso, M. (2010). The 1375 Ma "Kibaran Event" in Central Africa: prominent emplacement of bimodal magmatism under extensional regime, Precambrian Research.

Tankard, A.J. (1974). Varswater Formation of the Langebaanweg–Saldanha Area, Cape Province. Transactions of the Geological Society SA 77. 263-283.

Tankard, A.J. (1976a). Pleistocene History and Coastal Morphology of the Ysterfontein–Eland's Bay Area, Cape Province. Annals of the South African Museum 69. 73-119.

Tankard, A.J. (1976b). Cenozoic Sea Level Changes: A Discussion. Annals of the South African Museum 71. 1-17.

Tankard, A.J. (2022). Western Cape Crustal Thickness/Composition. PowerPoint presentation (DNSP-PST-128) presented at SSHAC Enhanced Level 2 Workshop 2, June 21, Cape Town, South Africa. 29.

Tankard, A.J.; Jackson, M.P.A.; Erikson, K.A.; Hobday, D.K.; Hunter, D.R.; Minter, W.E.L. (1982). Crustal Evolution of Southern Africa: 3.8 Billion Years of Earth History. Springer-Verlag, New York. 333-363.

Tankard, A.; Welsink, H.; Aukes, P.; Newton, R.; Stettler, E. (2012). Geodynamic Interpretation of the Cape and the Karoo Basins, South Africa. Phanerozoic Passive Margins, Cratonic Basins and Global Tectonic Maps. Elsevier, USA and UK.

Taylor, G.K. and Shaw, J. (1989). The Falkland Islands: new palaeomagnetic data for their origin as a displaced terrane from South America: in Hillhouse J.W. (Ed.), Deep Structure and Past Accreted Terranes, Geophysical Monograph 50.

Thamm, A.G.; Johnson M.R. (2006). The Cape Supergroup. In: Johnson, M.R.; Anhaeusser, C.R.; Thomas, R.J. (Eds.). The Geology of South Africa. Geological Society of South Africa, Johannesburg/Council for Geoscience, Pretoria, South Africa. 443-460.

Theron, J.N. (Compiler) (1975). 3318B Malmesbury – 3319A Ceres Geological Map Series. 1:125,000 Scale. Council for Geoscience, Pretoria, South Africa.

Theron, J.N. (1984). 3318 DC Bellville Geological Map. 1:50,000 Scale. Geological Survey of South Africa, Pretoria.

Theron, J.N. (Compiler). (1990). 3318 Cape Town Geological Map. 1:250,000 Scale. Council for Geoscience, Pretoria, South Africa.

Theron, J.N. (1992). Geological Map Sheet Explanation 3318 Cape Town Geological Map. 1:250,000 Scale. Geological Survey of South Africa, Pretoria. 140.

Theron, J.N.; Gresse, P.G.; Siegfried, H.P. and Rogers, J. (1992). The Geology of the Cape Town Area. Explanation of Sheet 3318. 1:250,000 Scale. Geological Survey of South Africa, Pretoria.

Tinker, J., de Wit, M. and Brown, R. (2008). Mesozoic exhumation of the southern Cape, South Africa, quantified using apatite fission-track thermochronology, Tectonophysics 455 (1-4), 77-93.

Van der Merwe, C. R. (1963). Soil Groups and Subgroups of South Africa. Department of Agricultural Technical Services, Pretoria, South Africa. Science Bulletin 356. 1-355.

Van Hinsbergen, D.J.J.; Buiter, S.J.H.; Torsvik, T.H.; Gaina, C.; and Webb, S.J. (2011). The Formation and Evolution of Africa: A Synopsis of 3.8 Ga of Earth History. Geological Society of London. ISBN 9781862393356.

Viljoen, J.H.A. (2008). 3318DD Stellenbosch Geological Field Map (Unpublished). 1:50,000 Scale. Council for Geoscience, Pretoria, South Africa.

Viola, G.; Kounov, A.; Andreoli, M.A.G. and Mattila, J. 2012. Brittle tectonic evolution along the western margin of South Africa: More than 500Myr of continued reactivation, Tectonophysics 514-517, 93-114.

Visser, H.H. (1988). Geological Report on the Koeberg Nuclear Power Station Site at Duynefontyn 34. ESKOM.

Visser, H.N. and Schoch, A.E. (1973). The Geology and Mineral Resources of the Saldanha Bay Area, Memoir. Geological Survey of South Africa 63.

Von Buchenröder, W.L. (1830). The Cape Town Earthquake of 1809. South African Quarterly Journal, Cape Town.

Von Veh, M.W. (1982). Aspects of Sedimentation, Structure, and Tectonic Evolution in the Tygerberg Terrane, Southwestern Cape Province. Bulletin of the Precambrian Research Unit, University of Cape Town, South Africa 32. 1-88.

Walford, H. L., and White, N. J. (2005). Constraining uplift and denudation of West African continental margin by inversion of stacking velocity data. Journal of Geophysical Research, 110, B04403.

Watkeys, M.K. (2006). Gondwana Break-up: A South African Perspective. In: Johnson, M.R.; Anhaeusser, C.R. and Thomas, R.J. (Eds.). The Geology of South Africa. Geological Society of South Africa, Johannesburg/Council for Geoscience, Pretoria, South Africa. 531-540.

White-Gaynor, A.L.; Nyblade, A.A.; Durrheim, R.; Raveloson, R.; Van der Meijde, M.; Fadel, I.; Paulssen, H.; Kwadiba, M.; Ntibinyane, O.; Titus, N. and Sitali, M. (2020). Lithospheric Boundaries and Upper Mantle Structure Beneath Southern Africa Imaged by P and S Wave Velocity Models. Geochemistry, Geophysics, Geosystems 21(10).

White-Gaynor, A.L.; Nyblade, A.A.; Durrheim, R.J.; Raveloson, R.; Van der Meijde, M.; Fadel, I.; Paulssen, H.; Kwadiba, M.; Ntibinyane, O.; Titus, N. and Sitali, M. (2021). Shear-Wave Velocity Structure of the Southern African Upper Mantle: Implications for Craton Structure and Plateau Uplift. Geophysical Research Letters 48(7).

Yang, Z.; and Chen, W.P. (2008). Mozambique Earthquake Sequence of 2006: High-Angle Normal Faulting in Southern Africa. Journal of Geophysical Research, Solid Earth 113(B12).